Design and Optimization of Force-Reduced High Field Magnets

by

Szabolcs Rembeczki

Master of Science
in Physics
University of Debrecen, Hungary
2003

A dissertation
submitted to
Florida Institute of Technology
in partial fulfillment of the requirements
for the degree of

Doctor of Philosophy
In
Physics

Melbourne, Florida
May, 2009

We the undersigned committee hereby recommend
that the attached document be accepted as fulfilling in
part the requirements for the degree of
Doctor of Philosophy in Physics.

"Design and Optimization of Force-Reduced High Field Magnets,"
a dissertation by Szabolcs Rembeczki

László Baksay, Ph.D.
Professor
Physics and Space Sciences
Dissertation Advisor

Rainer B. Meinke, Ph.D.
Senior Scientist and Director
Advanced Magnet Laboratory
Palm Bay, Florida

Hamid K. Rassoul, Ph.D.
Professor
Physics and Space Sciences
Associate Dean, College of Sciences

Marcus Hohlmann, Ph.D.
Associate Professor
Physics and Space Sciences

Hakeem Oluseyi, Ph.D.
Assistant Professor
Physics and Space Sciences

Hector Gutierrez, Ph.D.
Associate Professor
Mechanical and
Aerospace Engineering

Hans J. Schneider-Muntau, Ph.D.
Professor
National High Magnetic Field Laboratory,
Tallahasse, Florida

Gábor Dávid, Ph.D.
Senior Scientist
Brookhaven National Laboratory
Upton, New York

Terry D. Oswalt, Ph.D
Professor and Head
Physics and Space Sciences

Abstract

Title: Design and Optimization of Force-Reduced High Field Magnets

Author: Szabolcs Rembeczki

Advisor: László Baksay, Ph.D.

Co-Advisor: Rainer B. Meinke, Ph.D.

High field magnets have many important applications in different areas of research, in the power industry and also for military purposes. For example, high field magnets are particularly useful in: material sciences; high energy physics; plasma physics (as fusion magnets); high power applications (as energy storage devices); space applications (in propulsion systems).

One of the main issues with high-field magnets is the presence of very large electromagnetic stresses that must be counteracted and therefore require heavy support structures. In superconducting magnets, the problems caused by Lorentz forces are further complicated by the fact that superconductors for high field applications are pressure sensitive. The current carrying capacity is greatly reduced under stress and strain (especially in the case of Nb_3Sn and the new high temperature superconductors) so the reduction of the acting forces is of even greater importance. Different force-reduced magnet concepts have been studied in the past, both numerical and analytical methods have been used to solve this problem. The developed concepts are based on such complex

winding geometries that the realization and manufacturing of such coils is extremely difficult and these concepts are mainly of theoretical interest.

In the presented research, a novel concept for force-reduced magnets has been developed and analyzed which is easy to realize and therefore is of practical interest. The analysis has been performed with a new methodology, which does not require the time consuming finite element calculations. The developed computer models describe the 3-dimensional winding configuration by sets of filaments (filamentary approximation). This approach is much faster than finite element analysis and therefore allows rapid optimization of concepts. The method has been extensively tested on geometries of force-reduced solenoids where even analytical solutions exist. As a further cross check, the developed computer codes have been tested against qualified finite element codes and excellent agreement has been found.

The developed concept of force-reduced coils is directly applicable to pulsed magnets and a conceptual design of a 25 Tesla magnet has been developed. Although no experimental proof was possible within the scope of this research, there is strong evidence to believe that the developed concept is also applicable to superconducting magnets operating in a constant current mode.

Table of Contents

List of Figures

List of Tables

Acknowledgements

It is my honor to use this opportunity to thank my advisor, Prof. László Baksay for his support during my studies. My appreciation and respect also go to Dr. Rainer B. Meinke for his help and support in this research during the years. His knowledge, guidance, and patience were very valuable and helped me a lot, I appreciate it.

I would like to thank all members in my committee for the useful comments and suggestions. In particular, I am grateful to Prof. Hans J. Schneider-Muntau, former Deputy Director of National High Magnetic Field Laboratory, Florida State University. As a world known expert in the science of high magnetic fields, his suggestions were invaluable. I am also very grateful to Prof. Hamid K. Rassoul for his constructive suggestions and encouragement at important phases of my research. I wish to thank Dr. Gábor Dávid for introducing me to nuclear physics research at the RHIC accelerator of Brookhaven National Laboratory, which made me realize the crucial role of high-technology magnet development for the high-energy frontier. My sincere gratitude goes to Prof. István Lovas, Hungarian Academy of Sciences and University of Debrecen, Hungary, who guided my first steps into physics research. I also thank Dr. Stephane Vennes the useful discussions. Special thanks also go to Noni Warrell for her help.

I thank all the members of Advanced Magnet Lab for their support and providing the resources to my work. I am particularly indebted to Dr. Philippe Masson, Sasha Ishmael and Jeff Lammers for their great help and useful suggestions. I also acknowledge here the valuable discussions and help of Carl L. Goodzeit.

Last but not least, I am most grateful to my parents for their support during the years. My closest friends also deserve thanks and gratitude for their many years of friendship and support. Thank You!

Dedication

To My Parents

Chapter 1

Introduction

1.1 Overview of High Field Magnet Technology

In this section, I provide a brief overview of the development of high magnetic field generation methods focusing on the main design issues that constrain their achievable magnetic fields. As a definition of high magnetic field, one can say that the field a magnet produces is “high”**,** if it tests the limits of the mechanical and/or electromagnetic properties of the materials of which the magnet is made (National Research Council 2005).

Why high magnetic fields? In general, interactions between materials and magnetic field increase strongly with increasing field, and more detailed properties of materials are revealed by higher magnetic fields (Motokawa 2004). Fifteen Nobel prices have been awarded for discoveries that are directly due to applications of high magnetic fields.

Magnetic fields can be generated by permanent magnets made from hard magnetic materials or by electromagnets. Permanent magnets offer a cost-effective way to achieve magnetic fields up to almost 2 T. Magnetic fields above 2 T can be generated by different types of electromagnets which fall into three broad classes (Friedlander 1991): 1. resistive magnets with ferromagnetic core, 2. resistive magnets with air core, 3. superconducting magnets (usually with air core). In addition to these electromagnet types, one can also distinguish hybrid magnets that are a combination of resistive and superconducting magnets.

In electromagnets the current carrying conductor generates a certain magnetic field topology depending on the arrangement of the conductors. For very high field generation solenoids represent the most efficient geometry (Schneider-Muntau 2004). In general, the field (B_0) generated in the bore can be expressed as:

$$B_0 = \mu_0 j_0 a_1 h_0, \tag{1.1}$$

Where μ_0 is the permeability of vacuum, j_0 is the maximum value of current density in the coil volume, a_1 is a typical length like the radius of the bore, and h_0 is a dimensionless factor depending on the geometry of the magnet and on the current distribution (Aubert 1991). One can optimize these parameters in an electromagnet to reach higher fields in the bore. I will use equation 1.1 as a guide line to discuss the main design issues and limitations (if exist) of the basic types of high field electromagnets.

Table 1.1 High magnetic field generation methods with their typical (upper) limits.

Field Generation Method	**Field [T]***
Permanent Magnets	~ 1-2
Superconducting Magnets	~ 20
Resistive Magnets (Steady State)	~ 30 – 35
Hybrid Magnets	~ 40 – 45
Pulsed Magnets	~ 50 – 80
Flux Compression	~ 10^3

* Field values after Knoepfel (2000), Herlach and Miura (2003), Schneider-Muntau (2009)

1.1.1 Resistive Magnets

One can change the permeability in equation 1.1 in order to reach higher fields by applying materials with high relative permeability (for example iron) in the magnet. In iron cored electromagnets, the iron becomes saturated, limiting the maximum field to about 2 T.

Higher fields can be achieved in massive, steady state, air-cored resistive magnets by supplying large currents and several megawatt of power. However, increasing the current density in equation 1.1 brings up two major design issues: the problem of Lorentz forces and Joule heating. On one hand, increased electromagnetic forces tend to destroy the magnet, on the other hand, the increased Joule heating can also damage the magnet materials.

The Joule heating in steady state resistive magnets can be reduced using special current distributions with different types of cooling methods. Application of higher conductivity conductor materials can also reduce the Joule heating in resistive magnets, however, those materials (like high purity Cu or Al) are usually too soft to sustain the acting Lorentz forces, and hence massive reinforcement would be necessary. Addition of reinforcement materials, however, dilutes the overall current density, making the magnet larger, more expensive and less efficient.

High field resistive magnets are usually built by using Bitter type magnets (Bitter 1936) or polyhelix magnets (H. Schneider-Muntau 1974). Bitter type magnets are disc magnets: large number of copper discs piled up one on top of the other, interleaved with insulator foils. An improved version of these magnets is the Florida-Bitter magnet (Gao et al. 1996), designed at the National High Magnetic Field Laboratory, Florida.

In Bitter magnets, the current density has its highest value at the inner radii of the conductor discs. Thus, the maximum hoop stress occurs at the inner radius of the magnet. The hoop stress on the inside is further amplified by the accumulation of stress from the outer parts of the disks.

In polyhelix magnets this latter problem is solved by splitting up the magnet into a set of mechanically isolated concentric monolayer subcoils of thin wall thickness. The subcoils are electrically insulated from each other and powered separately, so each subcoil is subject to the same hoop stress (constant-stress current density distribution).

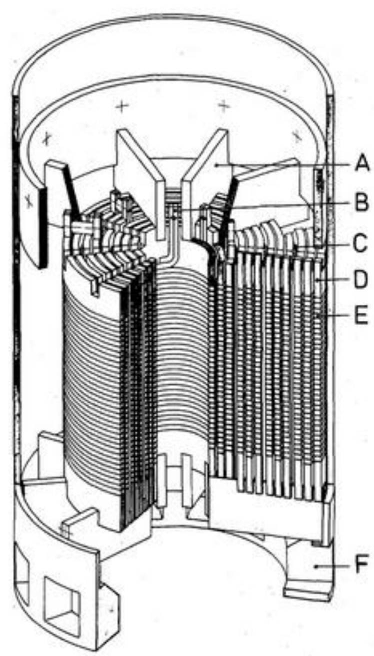

Figure 1.1 Polyhelix magnet. A: top cross; B: current connection of the helices; C: insulation layers; D: holding cylinder; E: winding; F: bottom cross (Schneider-Muntau 1981).

1.1.2 Pulsed Magnets

In (resistive) electromagnets, the problem of Joule heating can be also handled by operating the magnet in pulsed mode in order to reach higher fields. In pulsed mode, the magnet is pre-cooled (for example to liquid N_2 temperature) and the electric pulse energy is absorbed by the enthalpy of the magnet. In "short-pulse" magnets, fields can be generated with 5 – 50 ms pulse duration, while in "mid-pulse" magnets the pulse duration can be 50 – 100 ms. Small, pulsed magnets provide access to fields around 50 T for many applications worldwide.

The development of high field pulsed magnets encounters another obstacle: coil destruction by electromagnetic forces. In the ~10ms range pulse duration, the highest available pulsed field is around 80 T. Higher fields, for much shorter pulse duration (0.1 – 10 μs) can be generated by destructive pulsed magnets, where the magnet winding explodes or implodes.

There are two main types of destructive pulsed magnets. In the so called single turn systems, fields above 300T can be generated for microseconds. In these systems, the high field is created by passing a high current (several MA) through a small single turn coil by discharging a capacitor bank. Due to the large current density and resulting Lorentz forces the coil expands, melts, vaporizes and explodes. The current feed from the capacitor bank therefore must be faster than the thermal and mechanical inertia of the coil.

Extremely high magnetic fields (in the order of thousand T) can be achieved by electromagnetic or explosive flux compression. In these systems a seed field is compressed in microseconds by a collapsing liner. The world record of 2800T has been achieved in Sarov (Russia) via explosive flux compression.

Although higher magnetic fields can be generated by pulsed magnets (compared to steady state magnets), they have a major drawback: pulsed fields are not applicable for all experiments.

Another promising way towards cost effective generation of high fields was opened by the discovery of superconductivity (Kamerlingh Onnes 1911). However, it soon turned out that superconductivity in most materials ceases at even modest magnetic fields. So, before introducing superconducting magnets, it is worth to review the basic concepts of superconductivity that govern superconducting magnet design.

1.1.3 Brief Introduction to Superconductivity

In the design of superconducting magnets, the most important properties of the applied superconductor are its critical temperature (T_c), critical magnetic field (B_c), and its critical current density (J_c). These three parameters determine the so-called critical surface (see figure 1.2). Below this critical surface the material maintains its superconducting state. If anyone of these parameters exceeds its critical value superconductivity is lost and the material returns to its normal, non-superconducting state, causing the magnet to quench. Since these quantities strongly determine the performance of the magnet, it is worth to review each of them briefly.

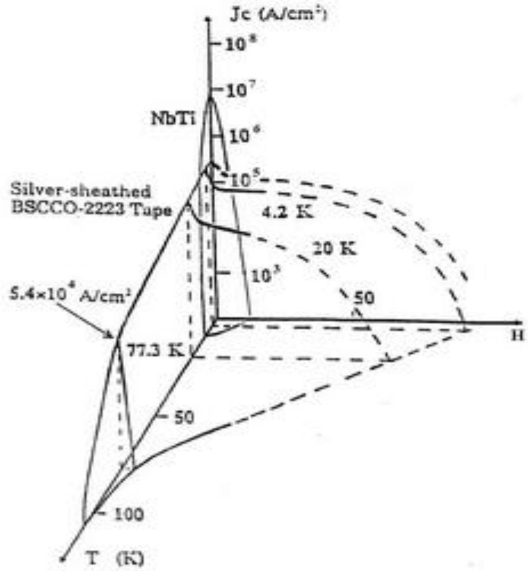

Figure 1.2 Critical surfaces of NbTi and BSCCO-2223 superconductors (Iwasa and Minervini 2003).

Critical Temperature

By decreasing the temperature of some metals close to absolute zero, the conductor electrons (fermions) form Cooper-pairs (bosons) and condensate into a state of lowest energy. This phase transition occurs when the temperature is below the material dependent critical temperature. Below the critical temperature the electric resistance drops to zero, and the material behaves as a perfect electrical conductor. Above the critical temperature the Cooper pairs break up, and the electrons behave as normal conductor electrons again.

Based on the value of critical temperature, two types of superconductors can be distinguished. Low temperature superconductors (LTS) require to be operated at liquid helium temperature. High temperature superconductors (HTS) exhibit superconductivity well above the boiling point of liquid nitrogen.

Critical Magnetic Field

Superconductors exhibit the so called Meissner effect (Meissner 1933), which is the total expulsion of magnetic flux from the superconducting specimen below a certain - material dependent - critical magnetic field B_c. Hence, this state of a material is also called the Meissner state.

Above the critical magnetic field it is energetically favorable to adopt the normal conducting state by admitting the magnetic flux into the specimen. Two basic types of superconductors can be distinguished by their behavior in magnetic fields.

Type I superconductors have rather low critical field values (~0.1 T), so they are not applicable to superconducting magnets. The first superconductors to be discovered were type I superconductors, i.e., metallic elements like mercury, tin and lead.

Type II superconductors have two critical magnetic field limits: a lower critical field B_{c1} and a higher critical field value B_{c2}. Up to B_{c1} the type II superconductors exclude the magnetic field from the interior, just like the type I materials. Above the lower critical field the magnetic field penetrates in form of discrete flux lines (fluxoids), however, while the bulk of the material still remains in the superconducting state. This is the so-called mixed state. The normal state core of each fluxoid is enclosed by a vortex of supercurrent that contains (shields) the magnetic flux and the field is zero everywhere in the surrounding superconductor. In homogeneous crystals these fluxoids form a flux line lattice, the lowest energy configuration of the flux lines.

With increased magnetic field applied to the superconductor, the flux lines move closer to each other in the lattice. Reaching the upper critical field B_{c2}, the normal conducting cores of the fluxoids overlap, causing a phase transition from superconducting state to normal conducting state (quench).

The upper critical field B_{c2} of the type II superconductors is much higher than the critical field of type I superconductors. For superconducting magnets, especially for high magnetic fields, only type II superconductors can be applied. The most frequently used practical type II superconductors are metallic alloys or intermetallic compounds, like NbTi, Nb_3Sn (the only elemental type II superconducting materials are niobium, vanadium, technetium).

Table 1.2 Critical temperatures and fields of principal technical superconductors (after Knoepfel 2000)

	NbTi	**Nb_3Sn**	**HTS materials**
T_{c0} (K)	9.1	18.3	~90
B_{c0}(T)	14	24.5	>100

Critical Current Density

In type I superconductors, according to Silsbee's rule, the critical current is the current which gives rise to the critical magnetic field at the surface. In type II superconductors, the critical current corresponds to the point at which the fluxoid lattice starts to move, producing a voltage drop across the superconductor and the specimen becomes resistive. Motion of the fluxoids is due to the Lorentz force.

The critical current for a given type II superconductor is extremely sensitive to the crystalline structure. Any given alloy will show little change in critical temperature or upper critical field with changes in metallurgical treatment (cold work or annealing), but critical currents will show wide variations (Montgomery 1969). In the so called hard superconductors with crystal lattice imperfections (such as grain boundaries, dislocations or compositional variations), the flux lines can become pinned. The strength of the pinning is described by the pinning force, and the critical current of a type II superconductor is a function of its maximum pinning strength.

1.1.4 Superconducting Magnets

The design of superconducting magnets differs from that of resistive winding magnets in that one is no longer concerned with power dissipation as a parameter, but instead with the relationship between current density and the required amount of superconductor (Montgomery 1969).

In superconducting magnets the conductor is kept in the superconducting state during normal operation. The allowed current density decreases with increasing applied field seen by the conductor, and approaches zero at an upper critical field. Due to the existence of an upper critical field for superconductors, the achievable magnetic field is also limited in superconducting magnets, even if the geometry factor h_0 in eq.1.1 (Aubert 1991) could be made infinite.

Present superconducting magnet technology is based on LTS limiting the fields to about 22T. Application of HTS at low temperatures increases their current carrying capabilities and due to their very large critical fields makes them promising candidates for high field generation (see figure 1.3). It is possible that superconducting magnets with field strength of 50T and beyond can be built in the future (Schneider-Muntau 2006) based on HTS conductors operating at liquid helium temperature.

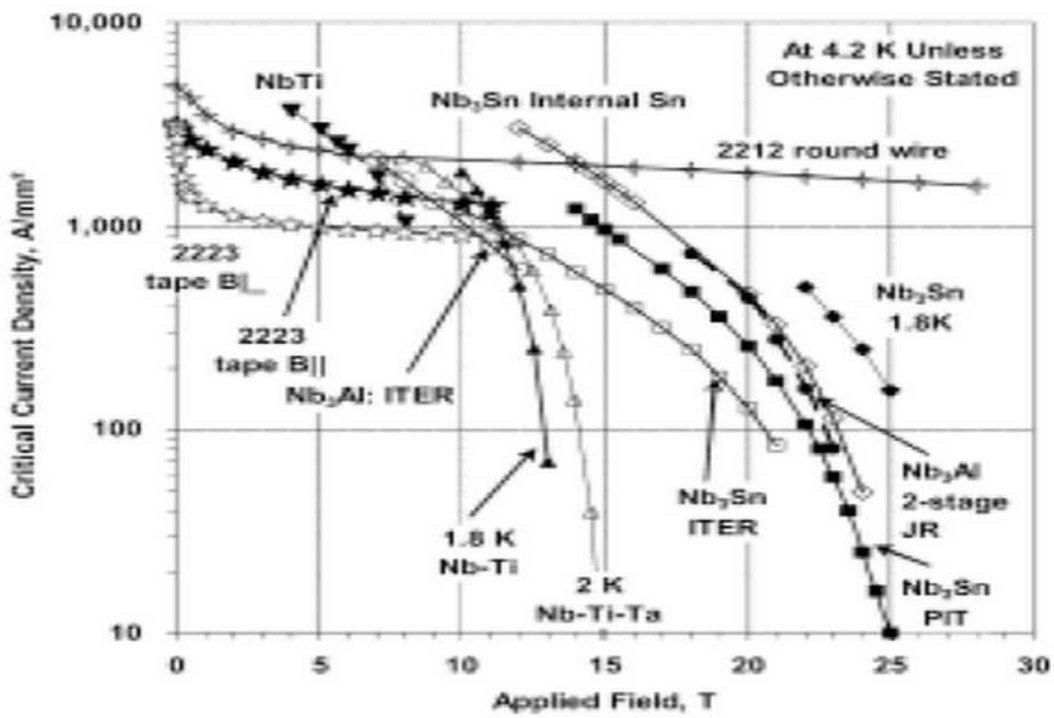

Figure 1.3 Critical current density vs. applied field for the typical superconductors (Lee 2006).

1.1.5 Hybrid Magnets

A resistive magnet can be surrounded with a superconducting magnet (Wood and Montgomery 1966) to further increase the field in the bore. In these hybrid magnets the outer, low field region of the resistive magnet is occupied by a large bore superconducting magnet, generating the booster field for the inner resistive magnet.

The hybrid magnet technology provides the most economical way to achieve the highest steady state magnetic fields. Currently the highest continuous magnetic field (~ 45 T) is generated by a hybrid magnet at the National High Magnetic Field Laboratory. The resistive insert of the hybrid uses 30 MW of electrical power to produce 31 T on axis, the remaining 14 T being produced by the superconductor "outsert" (the surrounding magnet section).

1.2 Importance of Force Reduction

As outlined before, the two major design issues in high field magnet technology are heat dissipation in the conductors and mechanical stresses due to the electromagnetic forces. At low fields magnet design is mainly dominated by heat evacuation problems. But, the problem of heat load does not limit the achievable field in a magnet. Whatever the magnet design, it is possible to evacuate the heat from the magnet with an appropriate circulation of coolant in the magnet (Aubert 1991).

At high fields magnet design is dominated by stress considerations. In a uniform current distribution solenoid, the strength of available materials limits the maximum achievable field, even if the magnet has an infinite geometry (h_0 is infinite in eq.1.1). However, with appropriate current distribution the achievable field is not limited by stresses in resistive magnets (Aubert 1991).

One can conclude that for resistive magnets with proper current distribution there is no principal limit to the generation of the highest continuous fields except for economics. Note, that every additional 5 T means doubling the power installation and the cooling infrastructure (Schneider-Muntau 1982). Also, the size of the magnet grows exponentially with the field level (Schneider-Muntau 2004), so everything must be done to reduce their size in precedence over minimizing their power consumption (Aubert 1991).

In the case of superconducting magnets the reduction of the acting forces are of even greater significance. Mechanical stresses which build up as the field is increased in a magnet could induce a sudden motion of a loose turn in superconducting magnets (Berlincourt 1963). Even microscopic movements of the conductors under the effect of Lorentz forces can generate enough frictional heat to cause the magnet to quench. Any reversion from the superconducting to the normal conducting state of even a small length of the conductor (quench) creates ohmic heating and an expanding normal conducting zone is created. The resulting temperature rise can exceed the melting point of the conductor and cause destruction of the magnet. Under smaller Lorentz forces, there is less chance of winding motion in force-reduced coils. In this way, the force-reduced superconducting coil is less capable to quench from local frictional heat generated by any wire motion.

The problems caused by large acting Lorentz forces are further complicated by the fact that superconductors for high field applications (mainly Nb_3Sn) and the new high temperature superconductors (HTS) are pressure sensitive. Reduction of stress and strain is especially important for high temperature superconductors which are brittle ceramics. Their critical currents and therefore their current carrying capacity are reduced under strain and stress (see appendix on strain dependence of Nb_3Sn critical parameters). The Lorentz forces acting in conventional coil configurations and the rather limited mechanical properties of the available conductors limit the feasibility of high field superconducting magnets (90% of the magnet volume is reinforcement with high strength steel). Because of size, cost would be prohibitive for standard applications (Schneider-Muntau 2006).

The two parts of hybrid magnets, i.e., the normal conducting insert and the superconducting outsert, mutually affect each other. The outer field of the insert coil increases the local field seen by the superconductor in the outsert and further limits its performance. Vice versa, the inner field generated by the superconducting outsert puts additional stress on the insert windings (Schneider-Muntau 2006). High forces acting between the resistive insert and superconducting outsert also have to be considered in the cryostat design and the suspension of the superconducting coils (Schneider-Muntau 1982).

In summary, the biggest problem of high field magnet design is the handling of the extreme forces in the magnet winding caused by the interaction of the high magnetic field and the current.

1.3 Scope

In the next chapter, I will introduce the main concepts of force-free magnetic fields, since it provides the fundamentals of the method of force-reduction in electromagnets. After introducing force-free magnetic fields and its possible applications, I'll overview previous methods and concepts of force-reduced magnets to gain more information and to investigate the main design issues.

In this work, I will focus on force-reduced solenoids (these solenoids are less studied in the literature) and higher fields can be generated by solenoids. In chapter 3, I will provide the details of my method of simulating force-reduced solenoids based on the concepts of force-free magnetic fields. This chapter will also provide the development of the model windings and their main features. I *won't* consider effects of iron and magnetization (iron core magnets) and I *won't* consider effects of eddy currents. The medium in the bore is assumed to be vacuum (or air). In chapter 4, I will apply and test the model in simpler monolayer coils, examine their properties and the origins of Lorentz forces. After examining the main properties of force-reduced monolayer solenoids, I will present the conceptual design of a 25-T force-reduced solenoid with novel winding scheme (chapter 5). The force-reduced winding scheme will be compared to conventional solenoids, and the results will be discussed.

Chapter 2

Force-Free Magnetic Fields and Force-Reduced Magnets

2.1 Force-Free Magnetic Fields

2.1.1 The Force-Free Condition

The magnetic field is said to be force-free in a region if the magnetic field is parallel to the direction of the current flow everywhere in that region. In other words, force-free magnetic fields exert no force on the conducting material (Zaghloul 1990).

For force-free magnetic fields two conditions must hold:

1. According to the definition of the force-free magnetic field, the Lorentz force must vanish, so for the magnetic force density:

$$\mathbf{f} = \mathbf{j} \times \mathbf{B} = 0 \tag{2.1}$$

2. The second condition arises from Maxwell's equations, that is, any magnetic field is source less (this is the condition for non-existence of magnetic monopoles or also called "solenoid condition"):

$$\boldsymbol{\nabla} \cdot \mathbf{B} = 0 \tag{2.2}$$

The $\mathbf{j} \times \mathbf{B} = 0$ condition is satisfied if: (*a*) $\mathbf{j} = 0$; (*b*) $\mathbf{B} = 0$; or (*c*) $\mathbf{j} = \alpha \cdot \mathbf{B}$. The α scale function is called as force-free function or factor (Yangfang 1983). This α force-free function is a scalar function of space and/or time, or might be constant (Knoepfel 2000).

The (a) and (b) simple solutions are special cases of the third (c) solution when $\alpha = 0$ (so $\mathbf{j} = 0$) and $\alpha = \infty$ (so $\mathbf{B} = 0$), respectively. Inserting $\mathbf{j} = \alpha \cdot \mathbf{B}$ into Ampere's law (see appendix eq. A.4) one obtains the force-free condition:

$$\nabla \times \mathbf{B} = \mu \cdot \alpha \cdot \mathbf{B} \tag{2.3}$$

As it can be seen, force-free fields do not automatically obey the superposition principle (G. E. Marsh 1996). Since $\nabla \times (\mathbf{B}_1 + \mathbf{B}_2) = \mu_1 \cdot \alpha_1 \cdot \mathbf{B}_1 + \mu_2 \cdot \alpha_2 \cdot \mathbf{B}_2$, thus $\mathbf{B}_1$ and $\mathbf{B}_2$ satisfy the force-free condition only if $\mu_1 \cdot \alpha_1 = \mu_2 \cdot \alpha_2$.

At first sight, the force-free condition is in contradiction with the Biot-Savart law, that is $d\mathbf{B}$ (at some field point) caused by a current element $Id\mathbf{l}$ (at some source point) is orthogonal to $d\mathbf{l}$. However, from the Biot-Savart law, it does not follow that the magnetic field $\mathbf{B}(\mathbf{r})$ caused by a current density $\mathbf{j}(\mathbf{r})$ is (locally) orthogonal to $\mathbf{j}(\mathbf{r})$. The reason for this is that orthogonality does not obey the superposition principle (Brownstein 1987) . Also, note that the following assumptions are involved in the definition of the force-free condition:

- The displacement current term (in eq. A.4) was ignored in the derivation of the force-free condition. This case is termed as magnetohydrodynamic approximation.
- The medium is isotropic and homogeneous, so material parameters (like conductivity, permeability and permittivity) are independent of space and time.

Both conditions are of course fulfilled in most situations.

Depending on the α parameter, force-free magnetic fields can be studied when α is a constant in space and time, or when α is a scalar function of space and time. According to the value of the force-free parameter, the following three major types of force-free magnetic fields are distinguished in the literature:

- Potential force-free magnetic fields (if $\alpha = 0$, so $\mathbf{j} = 0$).
- Linear (or constant α) force-free magnetic fields (if α is constant, but nonzero).
- Nonlinear (or non-constant α) force-free magnetic fields (if α is a scalar function of space and time).

In the next sections, a brief overview of the two major types of force-free magnetic fields is presented to introduce their major properties.

2.1.2 Linear Force-Free Magnetic Fields

The force-free current density $\mathbf{j} = \alpha \cdot \mathbf{B}$ together with Ohm's law (eq. A.5) results:

$$\mathbf{E} = \frac{\alpha}{\sigma}\mathbf{B} \tag{2.4}$$

If α is constant, substitution of $\mathbf{E}$ into the dynamic Maxwell's equations (equations A.3 and A.4) gives:

$$\nabla \times \mathbf{E} = \frac{\alpha}{\sigma}\nabla \times \mathbf{B} = -\frac{\partial \mathbf{B}}{\partial t} \tag{2.5}$$

and

$$\nabla \times \mathbf{B} = \mu \cdot \mathbf{j} + \mu \cdot \varepsilon \frac{\partial \mathbf{E}}{\partial t} = \mu \cdot \alpha \cdot \mathbf{B} + \frac{\mu \cdot \varepsilon \cdot \alpha}{\sigma} \frac{\partial \mathbf{B}}{\partial t}. \tag{2.6}$$

Substitution of eq. 2.5 into eq. 2.6 gives:

$$-\frac{\sigma}{\alpha}\frac{\partial \mathbf{B}}{\partial t} = \mu \cdot \alpha \cdot \mathbf{B} + \frac{\mu \cdot \varepsilon \cdot \alpha}{\sigma}\frac{\partial \mathbf{B}}{\partial t},$$

$$-\left(\frac{\sigma}{\alpha} + \frac{\mu \cdot \varepsilon \cdot \alpha}{\sigma}\right)\frac{\partial \mathbf{B}}{\partial t} = \mu \cdot \alpha \cdot \mathbf{B}\,,$$

it results:

$$\mathbf{B}(\mathbf{r}, t) = \mathbf{B}_0(\mathbf{r}) \cdot e^{-\left(\frac{\sigma\mu\alpha^2}{\sigma^2+\mu\varepsilon\alpha^2}\right)t} \tag{2.7}$$

In magnetohydrodynamic approximation the force-free solution can be obtained similarly. In this case the displacement current term is ignored in the Ampere – Maxwell law, and the force-free condition (eq. 2.3) can be directly plugged in, so

$$\nabla \times \mathbf{E} = \nabla \times \left(\frac{\alpha}{\sigma}\mathbf{B}\right) = \frac{\alpha}{\sigma}\nabla \times \mathbf{B} = \frac{\mu\alpha^2}{\sigma} \cdot \mathbf{B},$$

and with eq. A.3:

$$\nabla \times \mathbf{E} = -\frac{\partial \mathbf{B}}{\partial t} = \frac{\mu\alpha^2}{\sigma} \cdot \mathbf{B}.$$

It results:

$$\mathbf{B}(\mathbf{r}, t) = \mathbf{B}_0(\mathbf{r}) \cdot e^{-\left(\frac{\mu\alpha^2}{\sigma}\right)t}. \tag{2.8}$$

The solutions (eq. 2.7 and 2.8) describe the time dependence of force-free magnetic fields. Properties of the solutions (both in magnetohydrodynamic approximation and in non-magnetohydrodynamic case):

- The vectors and their derivatives are parallel: $\mathbf{B} \parallel \mathbf{j} \parallel \frac{\partial \mathbf{B}}{\partial t} \parallel \frac{\partial \mathbf{E}}{\partial t}$.
- The force-free magnetic field is static, if $\alpha = 0$ or $\sigma = 0$, otherwise decaying.

2.1.3 Nonlinear Force-Free Magnetic Fields

If α is a scalar function of space and time ($\alpha = \alpha(\mathbf{r},t)$ and $\mathbf{E} = \frac{\alpha(\mathbf{r},t)}{\sigma} \cdot \mathbf{B}$), then the curl equations of Maxwell equations have the forms of

$$\nabla \times \mathbf{E} = \frac{\alpha}{\sigma} \nabla \times \mathbf{B} + \frac{1}{\sigma} \nabla \alpha \times \mathbf{B} = -\frac{\partial \mathbf{B}}{\partial t} \tag{2.9}$$

and

$$\nabla \times \mathbf{B} = \mu \cdot \alpha \cdot \mathbf{B} + \frac{\mu \cdot \varepsilon \cdot \alpha}{\sigma} \frac{\partial \mathbf{B}}{\partial t} + \frac{\mu \cdot \varepsilon}{\sigma} \frac{\partial \alpha}{\partial t} \mathbf{B} \tag{2.10}$$

Substitution of $\partial \mathbf{B} / \partial t$ from eq. 2.9 into eq. 2.10 gives:

$$\nabla \times \mathbf{B} = \left(\mu \cdot \alpha + \frac{\mu \cdot \varepsilon}{\sigma} \frac{\partial \alpha}{\partial t} \right) \mathbf{B} - \frac{\mu \cdot \varepsilon \cdot \alpha}{\sigma} \left(\frac{\alpha}{\sigma} \nabla \times \mathbf{B} + \frac{1}{\sigma} \nabla \alpha \times \mathbf{B} \right),$$

so

$$\nabla \times \mathbf{B} = \left(\frac{\mu \cdot \sigma^2}{\sigma^2 + \mu \cdot \varepsilon \cdot \alpha^2} \right) \left(\alpha + \frac{\varepsilon}{\sigma} \frac{\partial \alpha}{\partial t} \right) \mathbf{B} - \left(\frac{\mu \cdot \varepsilon \cdot \alpha}{\sigma^2 + \mu \cdot \varepsilon \cdot \alpha^2} \right) \nabla \alpha \times \mathbf{B}.$$

It means if α is a scalar function of space and time, the force-free condition (eq. 2.3) is satisfied only, when $\nabla \alpha \parallel \mathbf{B}$ or $\nabla \alpha = 0$.

2.1.4 General Force-Free Magnetic Field Solutions

Force-free magnetic fields and their solutions in different coordinate systems (with some conditions) were studied by several authors, and the reader is referred to the literature on them. Here, only the general approaches are provided toward the force-free magnetic field solutions. Methods of obtaining solutions to the force-free field condition fall into two broad classes: those where α is a constant, and those where α is a function of space and time (G. E. Marsh 1996). As it will be shown, when α is not constant, the problem results in a non-linear equation.

First, consider the case when α is constant in space and time. Taking the curl of the force-free condition (eq. 2.3) and applying the solenoid condition from the Maxwell's equations gives:

$$\boldsymbol{\nabla} \times (\boldsymbol{\nabla} \times \mathbf{B}) = \boldsymbol{\nabla}(\boldsymbol{\nabla} \cdot \mathbf{B}) - \boldsymbol{\nabla}^2 \mathrm{B} = -\boldsymbol{\nabla}^2 \mathbf{B},$$

and

$$\boldsymbol{\nabla} \times (\boldsymbol{\nabla} \times \mathbf{B}) = \boldsymbol{\nabla} \times (\mu \cdot \alpha \cdot \mathbf{B}), \text{ so}$$

$$\boldsymbol{\nabla} \times (\mu \cdot \alpha \cdot \mathbf{B}) = -\boldsymbol{\nabla}^2 \mathbf{B}.$$

If α is constant, then:

$$\boldsymbol{\nabla} \times (\mu \cdot \alpha \cdot \mathbf{B}) = \mu \cdot \alpha(\boldsymbol{\nabla} \times \mathbf{B}) = (\mu \cdot \alpha)^2 \mathbf{B} = -\boldsymbol{\nabla}^2 \mathbf{B}, \text{ so}$$

$$\boldsymbol{\nabla}^2 \mathbf{B} + (\mu \cdot \alpha)^2 \mathbf{B} = 0. \tag{2.11}$$

The general form of solution to the vector wave equation 2.11 can be found in the following way (Zaghloul, Marsh). The scalar function Ψ satisfies the scalar Helmholtz equation:

$$\boldsymbol{\nabla}^2\Psi + (\mu \cdot \alpha)^2\Psi = 0.$$

Hansen showed, that three and only three vectors can be formed out of Ψ, such that they satisfy the original vector wave-equation (Hansen 1935) . The three vectors are: (i) $\mathbf{L} = \boldsymbol{\nabla}\Psi$, (ii) $\mathbf{P} = \boldsymbol{\nabla} \times \Psi\mathbf{r}$ (poloidal term), (iii) $\mathbf{T} = \boldsymbol{\nabla} \times \boldsymbol{\nabla} \times \Psi\mathbf{r}$ (toroidal term), where $\mathbf{r}$ is position vector.

Then, the general solution of the original vector field equation 2.11 is:

$$\mathbf{B} = \mathrm{a}\mathbf{L} + \mathrm{b}\mathbf{P} + \mathrm{c}\mathbf{T}. \tag{2.12}$$

The constants a, b and c are chosen so the solution satisfies the solenoid condition and the force-free condition. The solenoid condition implies a = 0, and the force-free condition yields b = $\mu\alpha$c.

Now, consider the case when α is a function of space and time ($\alpha = \alpha(\mathbf{r},t)$). Applying the double curl operation of $\mathbf{B}$ together with the force-free condition gives:

$$\boldsymbol{\nabla} \times (\boldsymbol{\nabla} \times \mathbf{B}) = \boldsymbol{\nabla} \times (\mu \cdot \alpha \cdot \mathbf{B}) = \mu \cdot \alpha(\boldsymbol{\nabla} \times \mathbf{B}) + \mu \cdot \boldsymbol{\nabla}\alpha \times \mathbf{B}.$$

At the derivation of equation 2.11 it was shown before that $\boldsymbol{\nabla} \times (\mu \cdot \alpha \cdot \mathbf{B}) = -\boldsymbol{\nabla}^2\mathbf{B}$, so:

$$-\boldsymbol{\nabla}^2\mathbf{B} = (\mu \cdot \alpha)^{\mathbf{2}}\mathbf{B} + \mu \cdot \boldsymbol{\nabla}\alpha \times \mathbf{B},$$

$$\mu \cdot \boldsymbol{\nabla}\alpha \times \mathbf{B} = (\mu \cdot \alpha)^{\mathbf{2}}\mathbf{B} + \boldsymbol{\nabla}^2\mathbf{B} \ .$$

This equation does not possess a general solution, and usually must be solved numerically (Low 2001).

2.1.5 Applications of the Force-Free Magnetic Field Concept

The concepts and theory of force-free magnetic fields were first introduced in astrophysics to allow coexistence of large currents and large magnetic fields in stellar material (Lust & Schulte 1954). In plasma physics, a simplified condition for pressure equilibrium is given by:

$$\frac{1}{\mu}(\nabla \times \mathbf{B}) \times \mathbf{B} = \nabla \mathrm{p},$$

where p is the gas pressure.

In many astrophysical applications the gas pressure p can be small enough. For example in the sun's chromosphere and in the corona the gas pressure is negligible, so the right hand side of the pressure equilibrium condition can be set equal to zero (G. E. Marsh 1996). In these cases the magnetic field must be approximately force-free in the plasma (since the left hand side is the force density itself).

The analog equation to the force-free magnetic field condition also appears in hydrodynamics:

$$\nabla \times \mathbf{v} = \Omega \cdot \mathbf{v},$$

where $\mathbf{v}$ is the fluid velocity, and Ω is constant or a function of position. Solutions where Ω is a function of space are known as Beltrami fields, while constant Ω solutions are termed Trkalian fields (MacLeod 1993).

Application of the force-free magnetic field concepts also plays an important role in high-field magnet design. One of the main problems in high-field magnets is the presence of huge electromagnetic stresses that are due to the Lorentz force acting on the coil. By minimizing the angle between the current density vector and the field vector in the winding, one could approximate force-free coil configurations in order to reduce the stresses in the magnet.

Force-free magnetic field principles can be applied not only for normal conducting magnets, but also for superconducting magnet design. It is even more important to reduce the forces in a superconducting winding, because most of the applied superconductors are brittle and strain sensitive, and any small displacement of the superconducting wires can cause a transition from superconducting to normal conducting state. Another advantage of near force-free magnetic configurations is the possibility to raise the current density limits of type II superconductors in superconducting magnets. These latter two applications will be discussed in more details in the followings.

2.2 Force-Free Magnetic Fields and Superconductors

Practically useful superconductors are type II superconductors. When an external magnetic field is applied, type II superconductors behave like type I materials up to the first critical field. After the first critical field, the field penetrates inside the superconductor and flux line lattice is formed, as it was described in the introduction. Depending on the external field orientation (relative to the current flow), the critical current density is different in the superconductor.

2.2.1 Transverse Applied Field in Type II Superconductors

Assume that a current flows through a type II superconducting sample having transverse applied field. Due to the Lorentz force, the flux lines tend to move in the superconductor. The motion of flux lines should be prevented in order to keep the material in superconducting state (see introduction). To prevent motion of flux lines, pinning centers (impurities, vacancies, dislocations etc) are introduced into the superconducting material (by metallurgical processes) to pin the flux lines to them. In equilibrium, the $\mathbf{f}_{\mathrm{P}}$ pinning force density (exerted by the pinning centers on the flux lines) balances the Lorentz force density:

$$\mathbf{j} \times \mathbf{B} + \mathbf{f}_{\mathrm{P}} = 0 \tag{2.13}$$

As the transport current increases, flux flow occurs when the Lorentz force on the flux line lattice exceeds the pinning force of the pinning centers. So there is a critical current beyond which a voltage is detected along the sample indicating the onset of flux flow (flux flow voltage), and the sample becomes resistive (flux flow resistance) (Anderson and Kim 1964).

2.2.2 Longitudinal Applied Field and Force-Free Current Flow

From the force-balance equation (eq. 2.13), Josephson suggested that with finite pinning force it is possible to increase the critical current in a superconductor by changing the angle between **j** and **B** (Josephson 1966). The critical current is highest in longitudinal geometry when the current in the superconductor and the applied field are parallel. Enhanced critical current in longitudinal geometry has been confirmed for several superconductors (see for example Cullen et al. 1963, Callaghan 1963, Boom et al. 1970, Timms et al. 1973 etc.).

The higher critical current value in longitudinal case can be explained by force-free current as follows. The field of the current and the applied field are perpendicular along the wire. The vortices aligning along these two perpendicular fields will tend to become entangled, and it leads to a force-free, helical flux line lattice (see Bergeron 1963, Walmsley 1972, and references therein).

It can be assumed that the current flows along the vortices comprising the flux line lattice. The azimuthal component of the force-free current flow will generate an axial magnetic field such that there is an enhancement of the magnetic flux within the superconducting wire (Bergeron 1963). As the applied current increasing, there is a critical current density ($j_{c\parallel}$) above which flux flow voltage is observed, and this $j_{c\parallel}$ is greater than the transverse critical current density ($j_{c\perp}$). The onset of flux flow resistance and voltage can be explained by measurements of the magnetization of the sample (see figure 2.1) and with the assumption of helical flux line lattice (Marsh 1994).

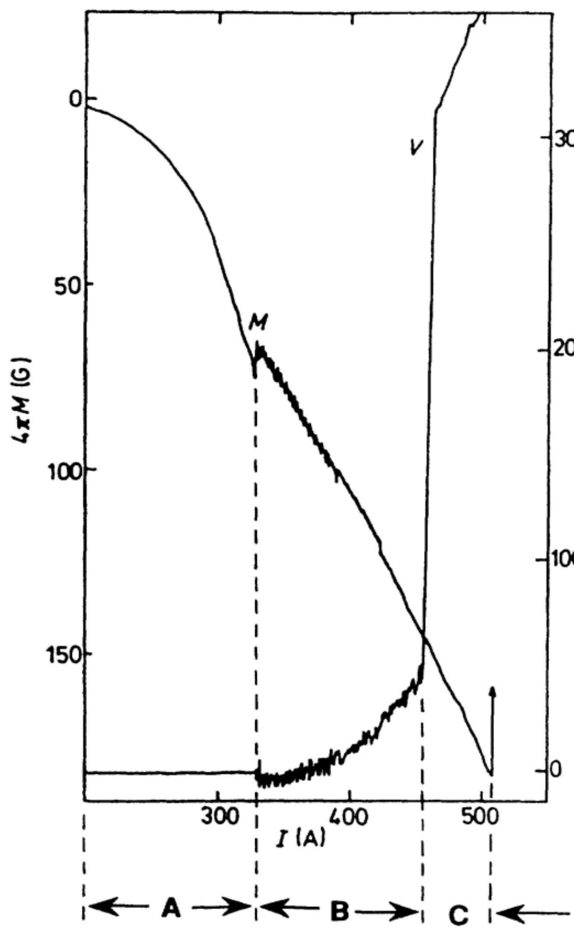

Figure 2.1 Magnetization and flux flow voltage as a function of current (G. E. Marsh 1994)

Increasing the current in the sample, there is a non-linear increase of paramagnetic moment (region *A* on figure 2.1). This implies that the flux line lattice must alter its geometry as follows. The angle the helical flux line lattice makes with the symmetry axis must, on the average, be increasing as the current increase. In this way the lattice gives rise to a greater current-induced magnetization than would result from only an incremental increase in current.

Further increasing the current in the sample, flux flow voltage appears on the sample when $j > j_{c\parallel}$. As the flux flow voltage appears, the paramagnetic moment increases linearly with the current (region *B* and *C* on figure 2.1). The linear increase in magnetization implies that the angle the helical flux line lattice makes with the symmetry axis must, on the average, be constant. So there is no net additional geometric contribution to the paramagnetic moment from the flux line lattice (see Marsh 1996 and references therein). Above the critical current, the flux line lattice deforms spontaneously and the flux line helices grow until they cut other flux lines or hit the surface of the specimen (Brandt 1995). In these cases the initially force-free configuration develops an instability (called helical instability) and the $\mathbf{B} \parallel \mathbf{j}$ condition is violated. The current configuration is no longer force-free and flux flow resistance appears.

It should be noted that in force-free configuration, the current could be carried without pinning in the superconductor (according to eq. 2.13) however, the force-free current in the superconductor tends to be unstable unless pinning centers stabilize it (Matsushita 1981). Absolutely straight flux-lines (parallel both to the applied current and field) are also not stable (Clem 1977). Furthermore, force-free current flow was also observed in longitudinal arrangement when persistent currents were induced in type II superconductors (Timms and LeBlanc 1974). Magnetization measurements of the specimen also indicated a tilted pattern circulation of the induced current such that the current tend to flow parallel to the total magnetic induction.

In summary, there is a possibility to increase the critical current density in superconducting magnets (Callaghan 1963) if the current in the superconductor is tend to be aligned with the field (in the winding).

2.3 Force-Reduced Magnets

2.3.1 The Virial Theorem

A practical magnet must have finite size. For finite size magnetic configurations, the virial theorem limits the volume that can be force-free. It means that stresses can be eliminated in a given region, but they cannot be cancelled everywhere (G. E. Marsh 1996).

The virial theorem gives a relationship between the time averaged potential energy and the time averaged kinetic energy T of any closed system of mass points with position vectors $\mathbf{r}_i$ subject to applied forces $\mathbf{f}_i$ (G. E. Marsh 1996):

$$\langle \int \mathbf{f} \cdot \mathbf{r} \, dV \rangle + 2\langle T \rangle = 0.$$

The virial theorem, originally introduced in the kinetic theory of gases, was extended by Chandrasekhar and Fermi to include magnetic fields (Moon 1984). This virial condition can be obtained from the field vectors (Chandrasekhar 1961) or from Maxwell's stress tensor (Parker 1958). Parker assumed the wires in a magnet to be perfectly conducting classical fluids.

For equilibrium configurations the kinetic energy vanishes. Since the forces are then constant in time, the virial theorem gives:

$$\int \mathbf{f} \cdot \mathbf{r} \, dV = 0.$$

The applied force consists of volumetric forces due to the magnetic field and volumetric forces of constraint ($\mathbf{f}_c$). So the total volumetric force density exerted on the *i* wires is:

$$\mathbf{f}_{\mathrm{i}} = \mathbf{f}_{\mathrm{ci}} + \frac{\partial M_{\mathrm{ij}}}{\partial \mathrm{x}_{\mathrm{j}}},$$

and the virial condition is:

$$\int \left(\mathrm{f}_{\mathrm{ci}} \cdot \mathrm{x}_{\mathrm{i}} + \frac{\partial M_{\mathrm{ij}}}{\partial \mathrm{x}_{\mathrm{j}}} \mathrm{x}_{i} \right) d\mathrm{V} = 0,$$

where M_{ij} is Maxwell's stress tensor:

$$\mathrm{M}_{\mathrm{ij}} = \frac{\mathrm{B}_{\mathrm{i}}\mathrm{B}_{\mathrm{j}}}{\mu} + \frac{\delta_{\mathrm{ij}}}{2\mu} \mathrm{B}^2.$$

The second term in the virial integral can be written as:

$$\int \frac{\partial M_{\mathrm{ij}}}{\partial \mathrm{x}_{\mathrm{j}}} \mathrm{x}_{i} \, d\mathrm{V} = \int \left[\frac{\partial}{\partial \mathrm{x}_{\mathrm{j}}} \left(\mathrm{M}_{\mathrm{ij}} \mathrm{x}_{\mathrm{i}} \right) - \mathrm{M}_{\mathrm{ij}} \delta_{\mathrm{ij}} \right] d\mathrm{V}.$$

In this equation, the first term on the right hand side is a volume integral of a divergence and can be converted to a surface integral by Gauss's theorem. Doing this integral transformation on the first term and substituting the Maxwell's stress tensor into the second term yields:

$$\frac{1}{2\mu_0} \int \mathrm{B}^2 d\mathrm{V} = -\int \mathrm{f}_{\mathrm{ci}} \cdot \mathrm{x}_{\mathrm{i}} \, d\mathrm{V} - \int \mathrm{M}_{\mathrm{ij}} \mathrm{x}_{\mathrm{i}} \, dS. \tag{2.14}$$

The left hand side of this equation is the total energy of the magnetic field, and assumed not to be zero. The two terms on the right hand side of this equation show, that in a finite size magnetic configuration one must have either (Parker 1958):

- inwardly directed internal forces of constraint f_{ci} (first term) or
- inwardly directed external forces (second term) exerted by external currents.

Furthermore, since the field cannot vanish on the surface S, there must be external forces to support the outwardly directed magnetic pressure due to the nonzero magnetic energy in the magnet. Even if the field is force-free, so the internal force (f_{ci}) vanishes, the magnet must be supported by surface loads (G. E. Marsh 1996).

2.3.2 Application of the Virial Theorem in Practice

The virial theorem expressed in form of equation 2.14 is true for an ideal, closed magnetic system. In a real magnet the forces that counteract the magnetic pressure are typically bigger than the magnetic field energy of system under consideration:

$$\frac{1}{2\mu}\int \mathrm{B}^2 dV \leq -\int \mathrm{f_{ci}} \cdot \mathrm{x_i}\, dV - \int \mathrm{M_{ij}}\, \mathrm{x_i}\, dS. \tag{2.15}$$

This form of the virial theorem sets a lower limit on the mass of the support structure. The left hand side of eq. 2.15 is the stored E energy in the magnet, so it can be written as:

$$\frac{1}{2\mu}\int \mathrm{B}^2 dV = \mathrm{E} \leq \sigma_\mathrm{w} \mathrm{V}, \tag{2.16}$$

where the acting stress σ_w is assumed to be constant throughout the V volume of the support structure. If ρ and M are the density and mass of the structural material respectively, then equation 2.16 determines a lower limit on the mass of the structural material (G. E. Marsh 1996):

$$\mathrm{M} \geq \frac{\rho \cdot \mathrm{E}}{\sigma_\mathrm{w}}.$$

For a maximum allowed stress in the material the above equation determines the minimum possible mass, or in other words, if some of the structural material is not stressed to the maximum allowed level of σ_W, then the total mass of the structure must be increased in order to store a given magnetic energy. Applying the above equation to existing magnets, Moon found that existing MHD and thermonuclear fusion magnets are heavier by an order of magnitude than the limit imposed by the virial theorem (Moon 1982). This means, that structural mass reduction is possible. The structural mass of the magnet can be minimized, by reducing the internal Lorentz forces in the magnet and supporting the system externally at the surface (Hill, Amm & Schwartz 1994).

2.3.3 Force-Reduced Magnet Studies

The possibility of applying the force-free magnetic field principles to magnet design has already been recognized in the 1950s (Lust & Schlute 1954). Since then an increasing number of articles offered solutions to force-free magnetic fields for various geometries. But, for several reasons, the proposed solutions are more of academic interest and hardly applicable directly to magnet manufacturing (Bouillard 1992). Here are some of the issues.

Theoretical solutions often assume some perfect symmetry. In a practical magnet there are regions of magnetic field, where no conductors are present. Currents, for example, are not present in the bore of the magnet, and even the winding cross-section is not completely packed with conductors (this is described by the packing factor in magnet design). It means that solutions, where α is constant everywhere in the magnet, are not practical solutions (Furth, Levine & Waniek 1957). According to $\mathbf{j} = \alpha \mathbf{B}$ condition (see eq.

2.3), α must be zero at least in the bore of the magnet (where currents are not present), and non-zero in the winding section of the magnet.

Also, a practical magnet must have a finite coil size, made out of conductors with given cross section. Force-free fields cannot be created in a real magnet because the winding has finite dimensions and its current distribution has discrete character (Shneerson et al. 1998). As it was also shown from the virial theorem, a finite size magnet cannot be completely force-free. Even if one assumes the opposite to be true, it is unnecessary to construct a fully force-free magnet, since the solid coil itself can withstand certain forces (Yangfang 1983). However, approximately force-free regions in a coil are possible to achieve. In such cases Lorentz forces are eliminated in a given region (force-free region) of a magnet, but they are actually displaced to the periphery of the force-free region (Bouillard 1992). In this way forces can be redistributed to a region where they can be compensated by a support structure more conveniently. Since the Lorentz forces are not completely zero, but are significantly reduced, these magnets are usually called “force-reduced”, “force-balanced” or “quasi-force-free” magnets in the literature.

Different types of force-reduced magnet geometries were studied in the relevant literature. Most of these studied magnet configurations have cylindrical (solenoidal) or toroidal geometry as explained below.

2.3.4 Solenoidal Magnets

For cylindrically symmetric geometries Lundquist developed a force-free magnetic field solution with field having zero radial field component (Lundquist 1951) . Assuming an infinitely long magnet where the remaining components have only radial dependence of the field, the field in cylindrical coordinates can be written as:

$$\mathbf{B} = \mathbf{B}(\mathbf{r}) = \mathrm{B_r}(\mathrm{r})\mathbf{e}_\mathrm{r} + \mathrm{B_\varphi}(\mathrm{r})\mathbf{e}_\varphi + \mathrm{B_z}(\mathrm{r})\mathbf{e}_\mathrm{z}.$$

If the radial field component $\mathbf{B}_\mathrm{r}$ is zero, then the force-free condition (eq. 2.3) becomes:

$$\nabla \times \mathbf{B} = -\frac{\mathrm{dB_z(r)}}{\mathrm{dr}}\mathbf{e}_\varphi + \frac{1}{\mathrm{r}}\frac{\mathrm{d[rB_\varphi(r)]}}{\mathrm{dr}}\mathbf{e}_\mathrm{z} = \mu\alpha(\mathrm{r}) \cdot \mathbf{B}(\mathrm{r}).$$

Or, for the components separately:

$$\frac{1}{\mathrm{r}}\frac{\mathrm{d}[\mathrm{r}\mathbf{B}_\varphi(\mathrm{r})]}{\mathrm{dr}} = \mu \cdot \alpha(\mathrm{r}) \cdot \mathrm{B_z}(\mathrm{r}),$$

$$-\frac{\mathrm{dB_z(r)}}{\mathrm{dr}} = \mu \cdot \alpha(\mathrm{r}) \cdot \mathrm{B_\varphi}(\mathrm{r}).$$

The Lundquist solution (figure 2.2) to this equation system is a constant α solution (α (r) = α_0 = const.), and therefore is not applicable directly to magnet design. It does not provide a bore region, where currents are not present.

A set of non-constant α solutions with cylindrical symmetry and also with vanishing radial field component were derived by Marsh (1996). However, either the solution from Marsh, or the solution from Lundquist, has infinite axial length, therefore they are of limited relevance for magnet design.

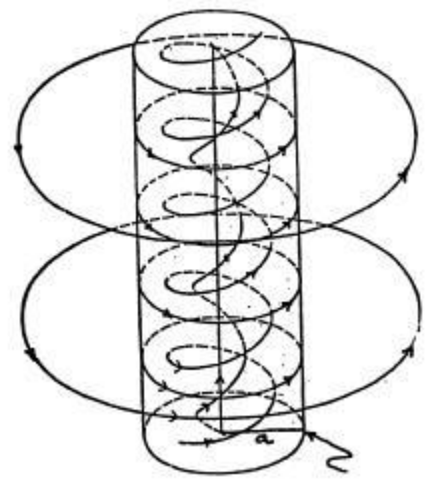

Figure 2.2 Field lines of the constant α Lundquist solution (Lundquist 1951).

Considering the shape of the cross-section in cylindrical geometries, Van Bladel argued, that circular boundaries and fields with circular symmetry yield the only solution if one establish force-free current distributions in cylindrical volumes (Van Bladel 1961). Any excursion from the circular symmetry reduces the degree of force reduction.

To derive finite structures from infinite cylinder solutions is a more difficult problem. A quasi-force free magnet concept was developed in St. Petersburg Technical University, Russia (Shneerson et. al 1998-2008) and its possible applications were studied by Schneider-Muntau at the National High Magnetic Field Laboratory, Florida. Their model solenoid consist windings with different current directions in multiple layers. The helical wires of the solenoid were bent back at the ends and then connected to collector ring to feed them. Their 3-layer model magnet had a very complex winding scheme (see figure 2.3).

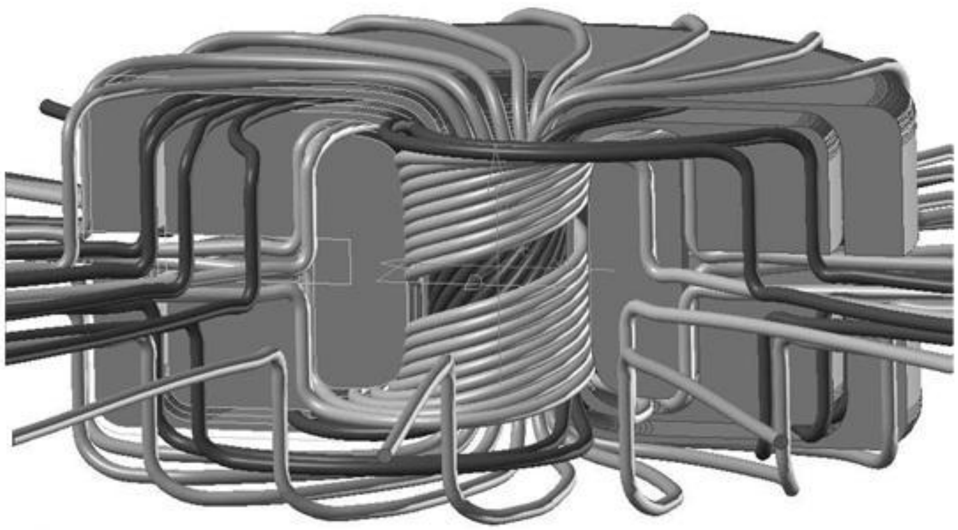

Figure 2.3 Spatial arrangement of the wires in a quasi force-free winding (Shneerson et. al 2005).

2.3.5 Toroidal Magnets

In toroidal coordinates, no exact analytical solution is known for non-constant α fields. In cylindrical coordinates and in toroidally curved cylindrical coordinates (R, φ, z) the Helmholtz equation is separable, but in toroidal coordinates it is non-separable (Buck 1965). Even if α is constant, the force-free equation does not appear to be directly soluble (G. E. Marsh 1996). An approximate constant α solution in toroidal coordinates was proposed by Buck (figure 2.4), while a non-constant α solution was given for example by Yangfang and Luguang (1983).

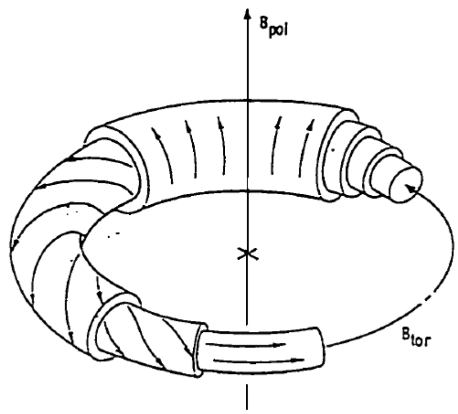

Figure 2.4 Toroidal force-reduced winding scheme (Buck 1965).

Two major types of force-reduced toroidal magnet designs can be distinguished (Furth et al. 1988). The first type of force-reduced toroids generates primarily toroidal magnetic field inside the torus. In this type of toroidal magnets (figure 2.5 a.) the ratio of major to minor radius (R/a) is large.

The second type of force-reduced toroids generates a poloidal field (outside, at the axis of the torus) and a toroidal field (inside the torus). The exterior poloidal field (see figure 2.5 b.), generated along the toroid axis, is easily accessible for experiments. These proposed toroids have low R/a value to produce high magnetic field in a small experimental volume.

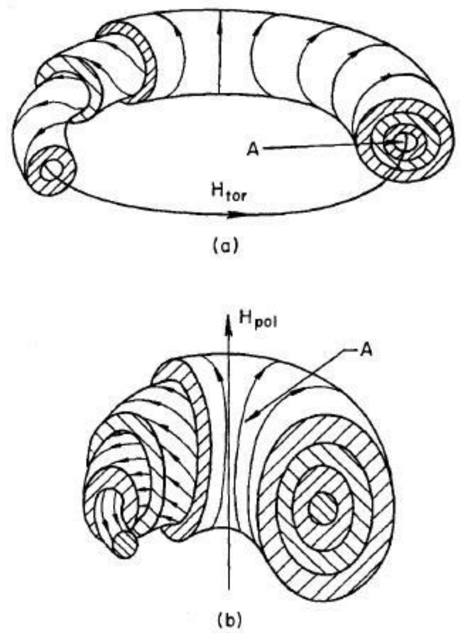

Figure 2.5 Force-reduced toroids with small and large aspect ratio.The experimental region is marked by *A* (Furth et al.1988).

In the first case of toroids, the pressure acting on the winding is reduced like the square of the ratio of the minor to major diameters, so large aspect ratio is preferred. In the second type of toroids, where the aspect ratio is smaller, multiple layer (or multi-stage) coil structures are desired to reduce the pressure on the winding (Furth, Levine & Waniek 1957). A simple layer force-reduced coil may be also used, but with a force-bearing shell outside.

In conventional toroidal arrays, large, radially inward forces act on the inner legs of the toroid. These forces must be supported either by wedging or bucking, hence conventional toroids are inherently wasteful of structural material. An improved force-reduced toroid was designed and studied by Hill, Amm and Schwartz (1994) based on the force-free toroidal solution of Furth et al. (1957):

$$j_r = A\, k \sin(kz)\ J_1\left(r\sqrt{\alpha^2 - k^2}\right)$$

$$j_\varphi = A\, \alpha \cos(kz)\ J_1\left(r\sqrt{\alpha^2 - k^2}\right)$$

$$j_z = A\sqrt{\alpha^2 - k^2}\cos(kz)\ J_0\left(r\sqrt{\alpha^2 - k^2}\right),$$

where the constants k and A describe the size of the toroid, and J_n is the Bessel function of the first kind of order n.

This solution represents a solid square toroid when $0 \leq \varphi \leq 2\pi$. However, this solution is a constant α solution, so it is not practical for magnet design because of the lack of a working magnetic bore. In order to provide a hollow toroidal bore, this force-free solution was modified with a conventional dee-shaped toroid design (Hill et al. 1994).

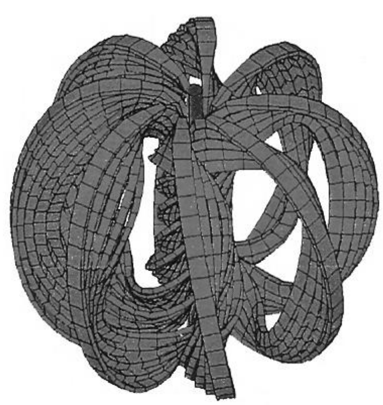

Figure 2.6 Modified squared toroid winding scheme (Amm 1996).

In the “modified square toroid” (MST), the force-free square toroid solution was applied to create the twisted current path of the inner legs, but conventional dee-shape design was applied for the outer legs (figure 2.6). The top of the MST magnet represents the boundary of the force-reduced system, so peak forces occur in this region of the MST. In the inner leg of the MST, the radial force is 2 to 3 times less than in conventional toroid winding (Hill, Amm and Schwartz 1994).

One of the disadvantages of toroidal geometries is that for most experiments the toroidal field is not accessible conveniently. Toroidal coil configurations however, would be potentially useful for inductive energy storage systems (Luongo 1996), or in high energy particle accelerators to form part of the guide field. Mawardi (1975) proposed a force compensated energy storage concept, where the poloidal and toroidal current components are decomposed to flow in separate layers (figure 2.7). In case of solenoids, this method of paired orthogonal current layers was also studied by Shneerson et al.

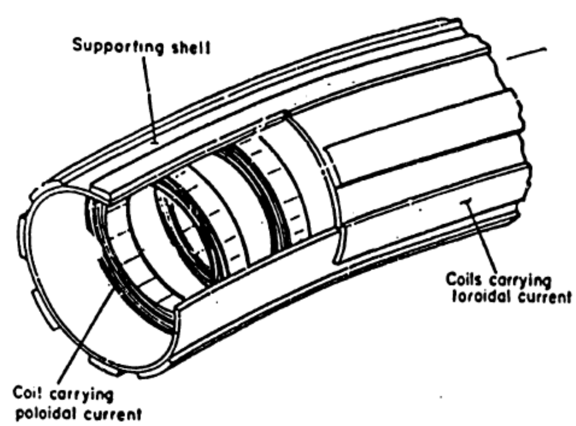

Figure 2.7 Force-reduced toroidal coil concept (Mawardi 1975).

The expansive force of the inner poloidal current layer is supported by the compressive force of the outer toroidal current layer. For large-scale supercondcuting magnetic energy storage (SMES) systems Nomura et al. developed a toroidal model magnet with force-balanced helical coil configuration (Nomura 1999).

Another major application of force-reduced toroidal configurations is for plasma containment in fusion reactors (Miura et al. 1994). The thermonuclear yield at a given temperature is proportional the squared of the ion concentration and hence, it is increased with the fourth power of the magnetic field strength. Therefore, in an ideal thermonuclear generator the technical limit for reaction yield is imposed by the mechanical forces in the magnet system that maintains the high magnetic field (Georgievsky et al. 1974).

In different fusion magnet designs (such as stellarators, heliotrons and torsatrons) loosely wound helical windings can generate the toroidal and poloidal magnetic fields (figure 2.8). Georgievsky et al. showed the advantages of the torsatron type geometry in applications of force-reduced toroidal systems for producing stellarator-type traps.

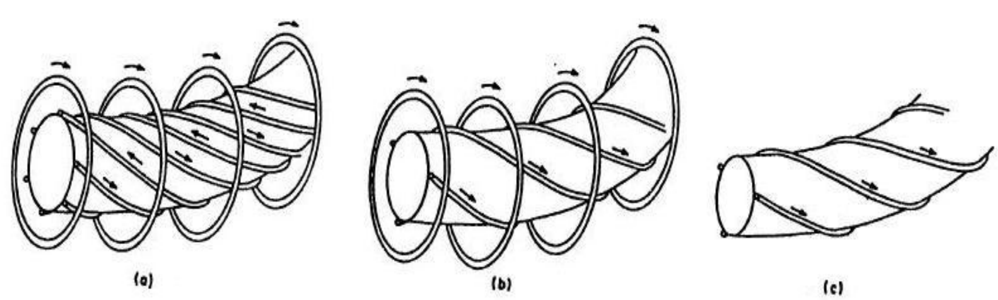

Figure 2.8 Winding scheme of (a) stellarator, (b) heliotron, (c) torsatron (Thome 1982).

Few experimental superconducting force-reduced toroid were also made and studied. Improved critical currents were confirmed. The critical currents of NbZr in the two NASA force-reduced toroids were 60 and 63 amperes compared with 17 to 20 amperes of conventional coils wound with the same material (Boom and Laurence 1970). Different helically wound force-balanced model toroids were also made in Japan using HTS superconductors (Nomura et al. 2002) and NbTi (Nomura et al. 2004).

The main advantage of toroids in the mentioned applications is the self-contained, closed field inside the torus. However, this toroidal field is hardly accessible for experimental purposes. On the other hand, the greater geometric complexity is another drawback of force-reduced toroids (Furth, Jardin, & Montgomery, 1988; Amm, 1996). The fabrication of the Japanese force-balanced superconducting coil, made by hand, took four month for three researchers (Nomura et al. 2007). It indicates that manufacturing of these coil configurations (especially in large-scale applications) involves many technical challenges.

2.4 Variable Pitch Magnet Concept

The basic equations that lead to the force-free condition reveal that a force-free magnetic field must possess vorticity and no divergence. So the force-free field is a rotational and solenoidal magnetic field. It results in a characteristic twisting of the field lines and hence the currents.

The handedness of the rotation is determined by the sign of α, and the period by the absolute value of α (G. E. Marsh 1996). In this force-free field, the lines of force are helices on coaxial cylinders with the pitch of H_z/H_φ varying along the radial direction r (Knoepfel 2000).

The pitch angle of a solenoid winding can be defined as the ratio of the magnitudes of the axial current density vector and the azimuthal current density vector. One can build an approximately force-free coil by winding the conductor in multilayered helices with radially dependent pitch angle $j_z(r)$ / $j_\varphi(r)$. The pitch angle of the current density vector can be varied with the radius in a winding system of N layers. The solution of a winding system of N layers with different pitch angle was used in the Shneerson model magnet (see figure 2.3 neglecting the outer parts). This method of winding excludes a radial current density. The axial current gives rise to a tangential field component and the tangential current to an axial field component. In a short coil both current components give rise to a radial field component too (Zijlstra 1967).

Chapter 3

Design Method and Optimization

The goal is to design and study a force-reduced solenoid based on the concept of variable pitch magnets. In this chapter, I describe the method of conductor path simulation and the way how the force-reduced configuration can be found based on this method. The applied design method was not used before to simulate force reduced solenoids. Some general properties of monolayer and multilayer force-reduced solenoids will be also shown here.

3.1 Filamentary Approximation

The design and optimization of the force-reduced magnet are based on filamentary approximation. In filamentary approximation of conductors, the linear dimension of the conductor cross section is much smaller than all other dimensions (Knoepfel 2000).

Approximation of the conductor by series of filamentary straight sections is particularly useful for numerical computations of magnetic fields and electromagnetic forces (Knoepfel 2000). Filamentary approximation can be often applied successfully also for conductors or coils of any shape, not necessarily circular and coaxial.

3.1.1 Conductor Path Generation

According to the variable pitch magnet concept, in an approximately force-free solenoidal magnet the conductor path follows helices on cylindrical cross-section. The programming of the helical conductors with several variable parameters was performed in MATLAB (version 7.0.4). The main programs can be found in the appendix.

The helical conductor path is generated by series of points connected to each other to form a filamentary wire of straight wire element sections. Direction can be assigned to the wire elements (according to the direction of the current flow), to form wire element vectors (d**l**). In this way the wire is approximated by a polygon of straight, infinitesimally thin wire element vectors (d**l**), that also represents the direction of the current flow in the wire (see figure 3.1). With a sufficiently large number of elements any winding configuration can be described with high precision.

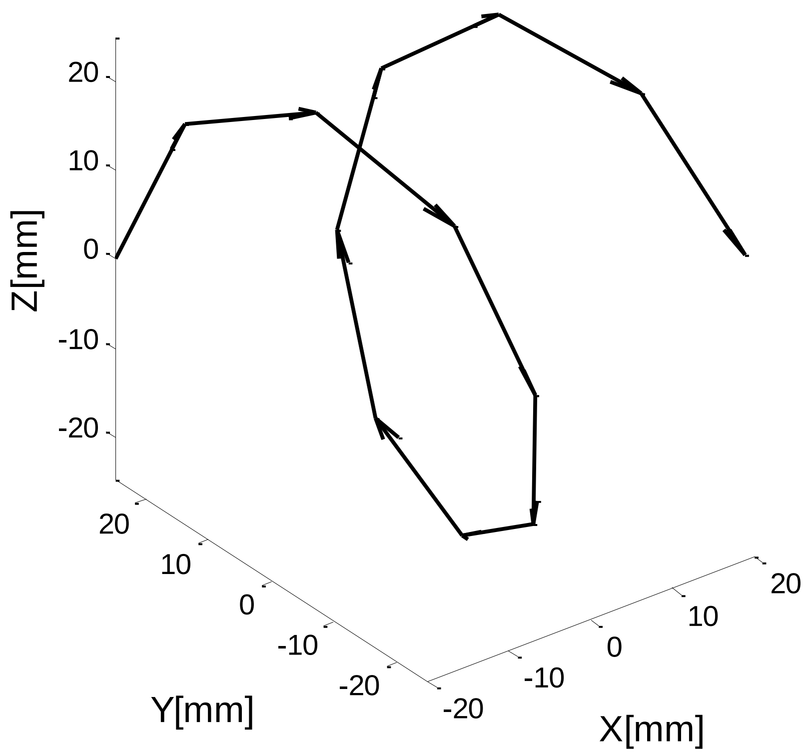

Figure 3.1 Sample of wire element vectors obtained by the simulation.

For the filamentary wire elements:

$$\mathbf{j}\mathrm{dV} \cong \mathrm{jsd}\mathbf{l} \cong \mathrm{Id}\mathbf{l},$$

where I = js is the total current flowing in the conductor of volume dV; s is the cross-sectional area of the conductor; **j** is the current density vector; I**dl** is the current element vector (distinguishing it from the wire element vector d**l)**.

The Cartesian coordinates of the points describing the helical conductor paths can be given with the following parametric equations (see also figures 3.2 and 3.3):

$$\mathrm{X} = \varphi \cdot \mathrm{L}/(2\pi \mathrm{n}) - \mathrm{L}/2,$$

$$\mathrm{Y} = \mathrm{R}\cos\ (\varphi + \mathrm{m} \cdot \varepsilon),$$

$$\mathrm{Z} = \mathrm{R}\sin\ (\varphi + \mathrm{m} \cdot \varepsilon),$$

where R is the radius of the cylindrical layer; φ is the azimuthal angle that goes from 0 to $2\pi n$, with n number of turns in the helix. The length of the solenoid layer is L and the helix is centered around zero. The phase angle difference ε between the conductors along the circumference of the solenoid is set to $2\pi/w_l$, where w_l is the total number of wires along the circumference of the solenoid layer l and m goes from 1 to w_l.

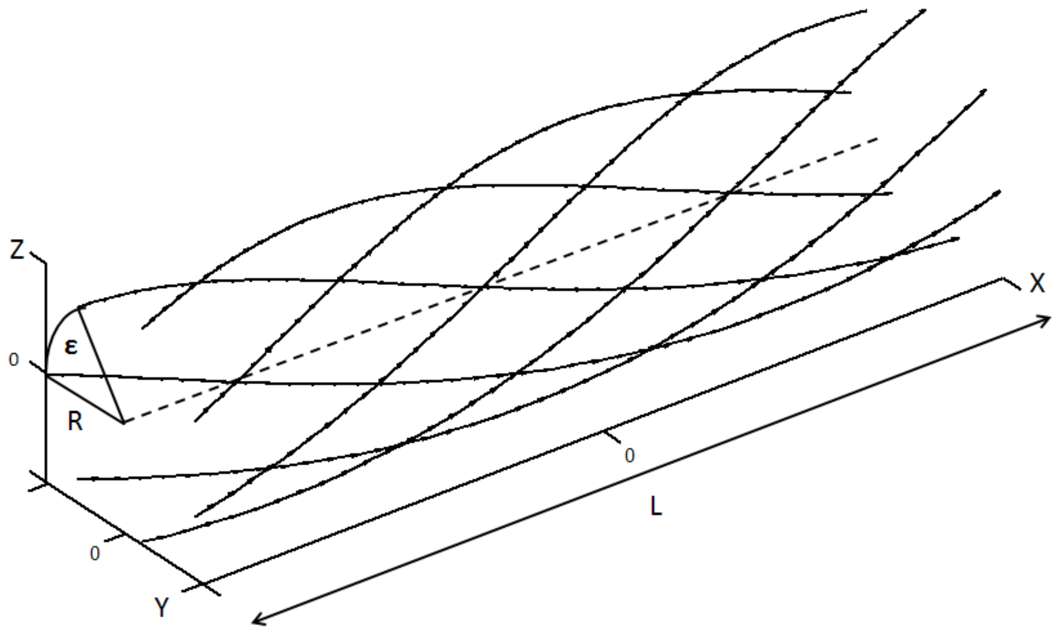

Figure 3.2 Helix geometry in MATLAB. L: total length of the solenoid; R: radius of the helices; ε: is the phase shift between the helices.

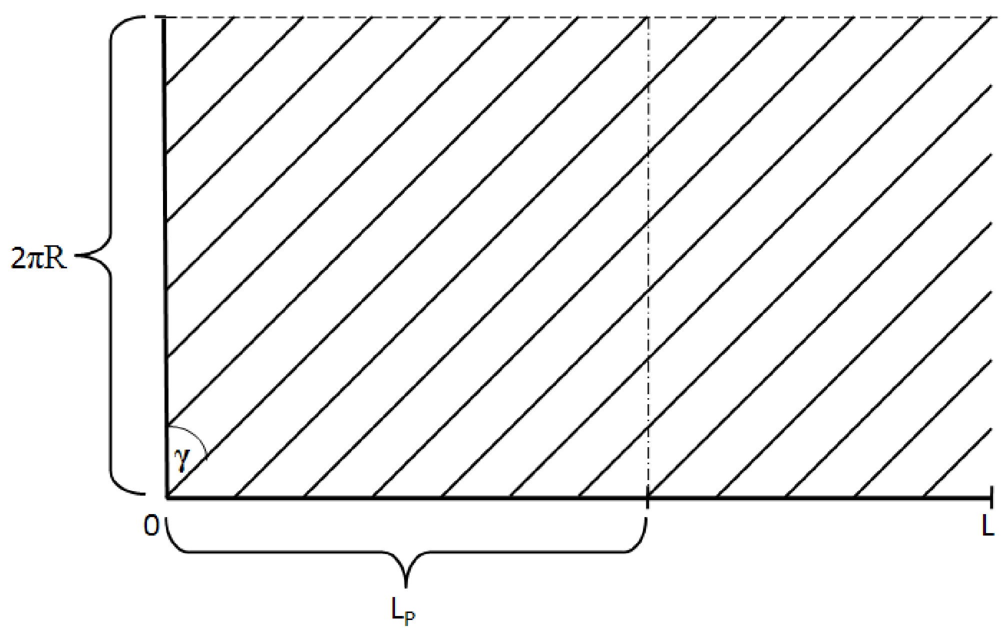

Figure 3.3 Unrolled view of a helix with 7 filamentary wires. L_p is the pitch length of the filaments; R is the radius of the helices; L is the length of the solenoid.

The pitch angle γ of the helices is measured from the cross-sectional plane (perpendicular to the solenoid axis), see figure 3.2. If L_p is the pitch length of the helices, i.e., the advance in the axial coordinate x per azimuthal advance of 2π (see figure 3.3), then

$$\tan(\gamma) = L_p/(2\pi R) = L/(2\pi Rn) \text{ , so: } X = \varphi \cdot R \cdot \tan(\gamma) - L/2.$$

It follows from the definition of the pitch angle, that a conductor with $\gamma = 0^{\circ}$ corresponds to an ideal solenoid, while conductors with $\gamma = 90^{\circ}$ represent parallel straight wires along the circumference.

3.1.2 Geometry Input Parameters and Code Description

The main parameters of the magnet geometry design are summarized in table 3.1. These parameters are used as input parameters in the MATLAB code to generate and plot the filamentary helical conductor path in '3D'. A sample input of the code and the calling routine of its main MATLAB functions are given in the appendix.

The code was written in a way that it is able to simulate multiple conductor layers. The number of possible layers is not limited and it is given by the user. In each conductor layer of the magnet, the input parameters can be varied separately and easily by the user. Additionally, one can also specify the cross-sectional parameters (width and thickness) of the conductors that form the helices. In this case the program automatically checks the input parameters to make sure that the conductors are not in contact and the magnet is feasible.

Table 3.1 Geometry Input Parameters of the Simulation

Main Geometry Parameters Of the Simulation
Total number of layers: N
Number of wires in the layers: w_l
Radii of the layers: R_l (mm)
Lengths of the layers: L_l (mm)
Pitch angle of the wires in the layers: γ_l (degree)

3.2 Magnetic Field Calculations

The magnetic field contribution of each straight filamentary element can be given in a simple closed form based on Biot – Savart law.

If d**l** is a filamentary wire element vector (pointing in the direction of current flow) that carries a current I and **r** is a vector from the wire element vector to a test point P, then the elemental magnetic induction vector d**B** at the test point P is given in magnitude and direction by:

$$\mathrm{d}\mathbf{B} = \mathrm{k}\,\mathrm{I}\frac{(\mathrm{d}\mathbf{l}\times\mathbf{r})}{|\mathbf{r}|^3}.$$

This is the Biot and Savart law, where the constant k depends in magnitude and dimension on the system of units used. In SI units and for vacuum, $\mathrm{k} = \frac{\mu_0}{4\pi} = 10^{-7} N \cdot A^{-2}$, or

$k = 10^{-7}$ H/m (Jackson 1999). Here, μ_0 is the magnetic permeability of vacuum: $\mu_0 = 4\pi \cdot 10^{-7} N \cdot A^{-2}$.

Based on filamentary approximation, the calculation of the magnetic induction was programmed in MATLAB as follows. If the position of the test point P is given by the vector $\mathbf{p}_t$, and the position of the i-th current element center is given by $\mathbf{p}_{ci}$, then $\mathbf{r} = \mathbf{p}_t - \mathbf{p}_{ci}$. The position vectors of each neighboring points on the polygonal helix are $\mathbf{p}_i$ and $\mathbf{p}_{i+1}$, so the i-th current element vector can be expressed as: $\mathrm{d}\mathbf{l}_i = \mathbf{p}_{i+1} - \mathbf{p}_i$. The magnetic induction vector can be written in terms of these position vectors as:

$$\mathbf{B}_i(\mathbf{p}_t) = k\, I \frac{(\mathbf{p}_{i+1} - \mathbf{p}_i) \times (\mathbf{p}_t - \mathbf{p}_{ci})}{|\mathbf{p}_t - \mathbf{p}_{ci}|^3},$$

where $\mathbf{B}_i(\mathbf{p}_t)$ is the magnetic induction vector at a test point P due to wire element $\mathrm{d}\mathbf{l}_i$.

The superposition principle holds for the magnetic fields because they are the solution to a set of linear differential equations, namely the Maxwell's equations, where the current is one of the "source terms". So the total magnetic induction vector **B** at point P can be obtained by the vector summation of all elemental magnetic induction vectors due to a polygon of filamentary wire elements (Knoepfel 2000):

$$\mathbf{B}(\mathbf{p}_t) = \sum_i \mathbf{B}_i(\mathbf{p}_t).$$

The test point(s) can be chosen inside and outside the bore, and also on the wire element center(s) (excluding the "source" current element itself of course). The magnitude and the direction of the current in the conductor filaments of a layer can be different for each layer and they are specified by the user as input variables of the simulation.

Validation of the field calculations was performed independently on a 3-layer solenoid, and the obtained results are in good agreement (Goodzeit 2008). The details of the validation are given in the appendix.

3.3 Force Calculations

The magnetic Lorentz force acting on the wire can be calculated in filamentary approximation as follows.

Consider current I of q charges in a conducting wire with cross-sectional area $\Delta\mathrm{s}$ and length $\Delta\mathrm{l}$. The wire is in a **B** magnetic field. In the wire, n number of charges per unit volume drift with velocity **v** parallel to the wire element vector d**l**. Hence the current in the wire is $\mathrm{I}\mathrm{d}\mathbf{l}/\Delta\mathrm{l} = (\mathrm{q}\,\mathrm{n}\,\Delta\mathrm{s})\,\mathbf{v}$. The magnetic Lorentz force d**F** acting on the electrons and transmitted onto the material per Δl length of the wire is $\mathrm{d}\mathbf{F} = \mathrm{qn}\Delta\mathrm{s}\Delta\mathrm{l}(\mathbf{v}\times\mathbf{B})$. Thus the force expressed with the current I flowing in the conductor is:

$$\mathrm{d}\mathbf{F}_{\mathrm{B}} = \mathrm{I}(\mathrm{d}\mathbf{l}\times\mathbf{B}).$$

This is the so called Biot-Savart force (Knoepfel 2000), and it gives the force acting on the Id**l** current element vector in magnetic field **B**. The **B** magnetic induction vector at the d**l** wire element vector can be given by the Biot-Savart law as it was described before, so the Biot-Savart force on the wire elements can be simulated (see figure 3.4).

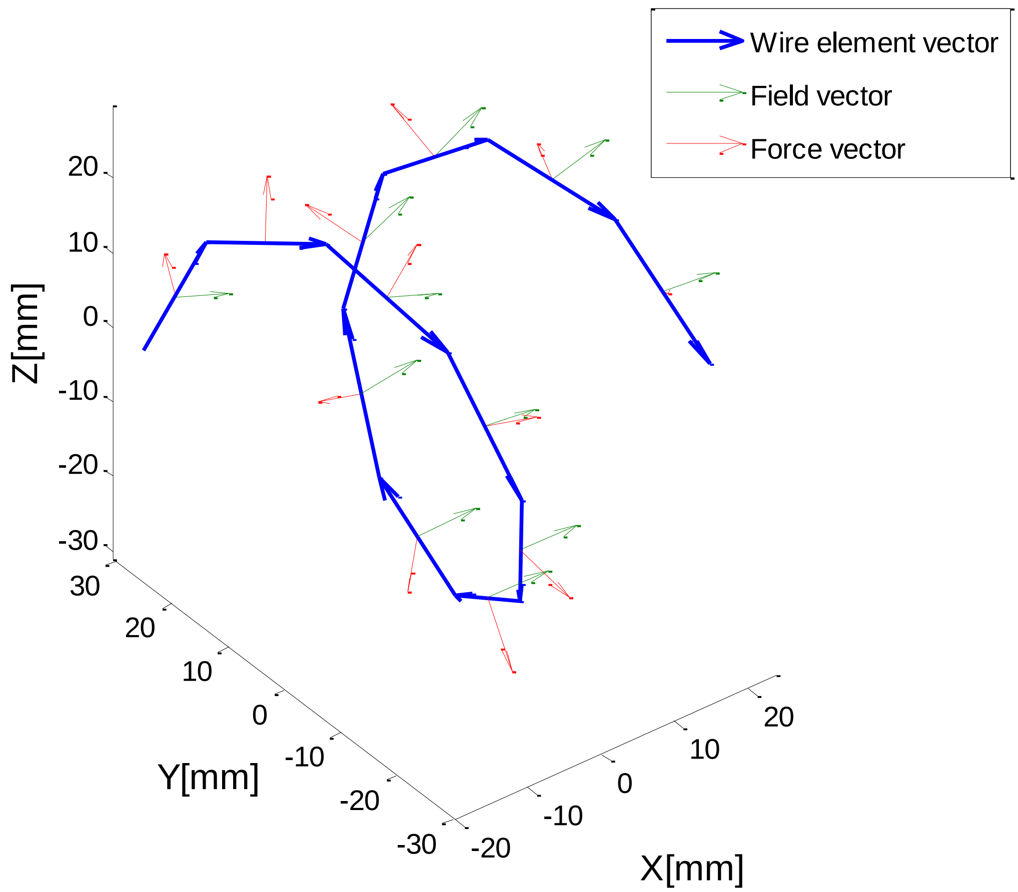

Figure 3.4 Presentation of Biot-Savart force vectors (red) and the field vectors (green) using filamentary approximation. The field and force vectors were calculated at the center of the wire element vectors (blue).

3.4 Optimization Using Force-Free Magnetic Field Theory

One of the main reasons why filamentary approximation was used is because it allows fast optimization of the winding configuration. The goal of the magnet optimization is to find a force-reduced configuration for a given number of conductor layers. The method of the magnet optimization is based on the theory of force-free magnetic fields.

3.4.1 Optimization Based on Force-Free Magnetic Field Theory

An approximately force-free coil can be built by winding the conductor in helices with a radially dependent pitch angle. The goal is to determine the optimal value(s) of pitch angle(s) for a given set of layer(s).

As it was discussed earlier, the magnetic field is force-free in a region if the magnetic field is parallel to the direction of the current flow in that region. It can be formulated by the Biot-Savart force in filamentary approximation as:

$$\mathrm{d}\mathbf{F}_{\mathrm{B}} = \mathrm{I}(\mathrm{d}\mathbf{l} \times \mathbf{B}) = 0, \text{if } \mathrm{d}\mathbf{l} \upuparrows \mathbf{B} \text{ or } \mathrm{d}\mathbf{l} \upharpoonleft\!\downharpoonright \mathbf{B}$$

The $\mathbf{B}$ total vector at a $\mathrm{d}\mathbf{l}$ wire element due to all other current elements in the magnet can be calculated by the Biot-Savart law. After calculating the $\mathbf{B}$ field vectors at each wire element in the magnet, the κ angle between each current element vector and the corresponding $\mathbf{B}$ vector can be determined ($\kappa = \measuredangle(\mathrm{d}\mathbf{l}, \mathbf{B})$).

According to the definition of the force-free magnetic fields, the Biot-Savart force acting on the winding can be reduced by minimizing the κ angle. The mathematical formulation of the magnet optimization is to minimize the κ angle between the field vector and the wire element vector by varying the γ pitch angle(s) of the winding in each l layer:

$$\text{Minimize } \kappa(\gamma_l),\ 0° < \gamma_l \leq 90°,\ l = 1 \ldots l_t\ ,$$

where l_t is the total number of layers. So the objective function of the optimization is the angle between the field vector and the current element vector. As a note: the main reason why I chose the κ angle to be minimized and not directly the force, is because this angle is the "cause": in order to reduce the force try to align the current element vectors and the field vectors. The other reason is practical: the calculation of the κ angles (scalars) requires less computational time than the calculation of forces (vectors), so the optimization code is faster in this way.

The optimization routine uses the commonly applied Nelder-Mead simplex method or amoeba method (Nelder and Mead 1965). The method finds the minimum of a scalar function of several variables (this is generally referred as multidimensional, nonlinear optimization). This simplex method is a direct search method (nonderivative optimization) that does not require any numerical or analytic gradients (Press, et al. 1988).

3.4.2 Monolayer Solenoids

Using the approach outlined above a pitch angle optimization has been performed for a single-layer solenoidal coil to determine the optimum pitch angle for different numbers of current carrying filaments. The optimization starts with specifying the basic geometry input parameters of the magnet layer.

The optimized pitch angle dependence on the number of filamentary wires is shown in figure 3.5 for a set of different radii coils (the length of the coils was fixed to 400 mm in the optimization).

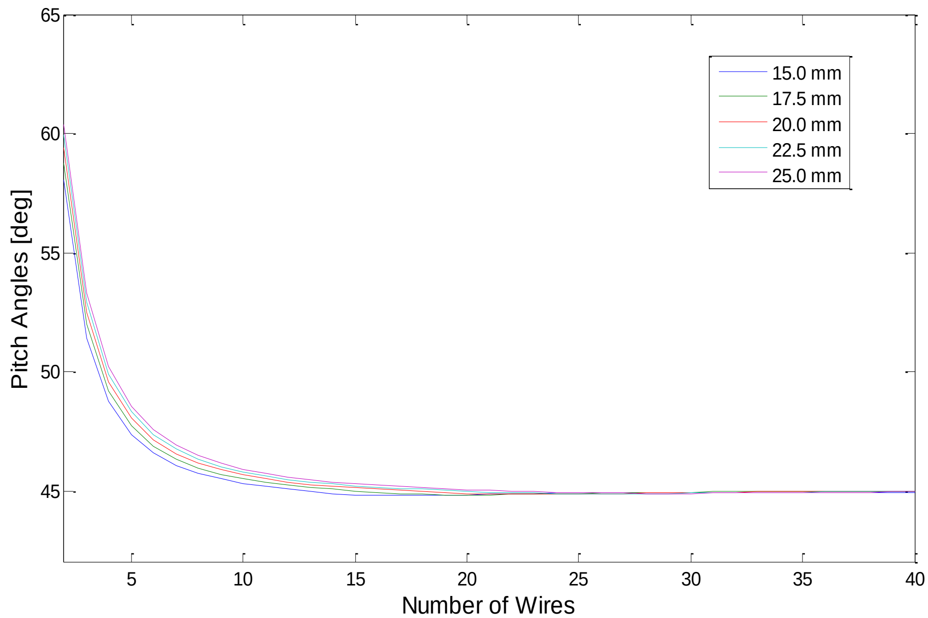

Figure 3.5 Optimized pitch angle as a function of number of wires (starting from 2) in monolayer solenoids for different radii from 15 mm to 25 mm.

As it can be seen, the ideal pitch angle of these coils converges to 45 degrees as the number of filamentary wires increase. Large number of uniformly distributed current filaments (current sheet approximation) would result also the same pitch angle (Furth et al. 1957). Helical windings with 45 degree pitch angle were also suggested by others to produce high magnetic fields (Hand and Levine 1962) and confirm the method being used in my optimization. The derivation of the 45 degree theoretical pitch angle will be discussed in the next chapter together with more details on magnetic fields and forces.

3.4.3 Multilayer Solenoids

The goal of the optimization is to determine the optimal pitch angle in each layer of a solenoid with multiple layers. The pitch angle of each layer was varied while the other main geometry parameters (see table 3.1) were the same in the layers (except the radii). The current magnitudes in the layers were fixed to be the same. In each layer the currents were set to flow in the same direction along the axis (see figure 3.7). Depending on the desired magnet design one can change each of these parameters.

To see how the pitch angles vary layer by layer, optimization was performed for seven different magnets with increasing total number of layers. Starting from a monolayer coil, additional layers were added with equal radial spacing, so the total number of layers in the last magnet is seven. The number of wires in each layer was set to 40 (well within the flat section of the curves in figure 3.5), and the radii of the coils increase with 5 mm increments starting with inner layer radius of 20 mm.

The results of the optimization runs are summarized in table 3.2 and figure 3.6. It shows the optimized pitch angles in each layer for the seven magnets with different total number of layers (N).

Table 3.2 Pitch angles of seven helical magnets with increasing total number of layers.

Total Number of Layers (N)	**Pitch Angles (degree)**						
1	45.39						
2	72.65	30.03					
3	77.45	56.15	23.94				
4	79.77	63.15	47.85	20.50			
5	81.16	67.02	55.21	42.60	18.13		
6	82.10	69.54	59.55	49.99	38.9	16.37	
7	82.79	71.31	62.48	54.47	46.18	36.1	14.99

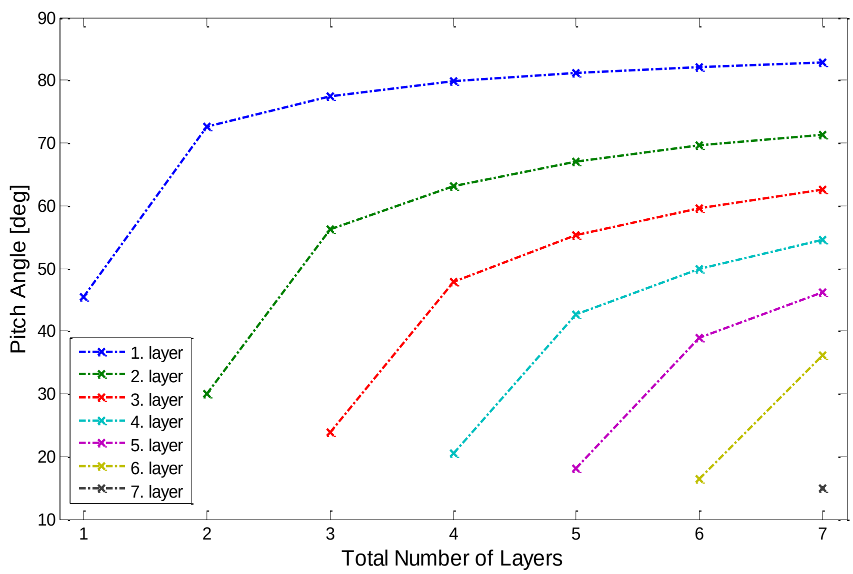

Figure 3.6 Pitch angle of the magnet layers as a function of total number of layers. The figure shows the values given in table 3.2.

From figure 3.6, the tendency of pitch angle variation can be seen readily. As the total number of layers increases in the magnet, the pitch angle of the inner layers converges to 90 degree (straight conductors parallel to the axis), while the pitch angles of the outer layers converges to 0 degree (ideal solenoid). The case of 4-layer magnet with the varying pitch angles is shown on figure 3.7 (for perspicuity only one wire filament is shown from each layer).

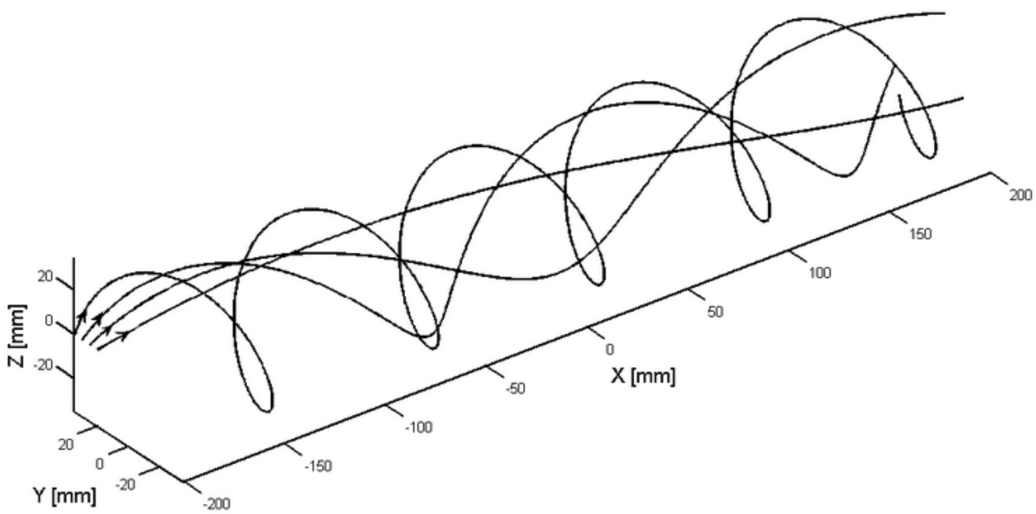

Figure 3.7 Four layer variable pitch magnet. Only one filamentary wire is shown from each layer (the arrows show the current direction in the layers).

The optimization results in table 3.2 and in figure 3.6 confirm that addition of force-free fields usually does not results in a new force-free configuration (see force-free condition eq. 2.3 and below). It can be explained as follows. Let' assume two monolayer force-reduced solenoids are given with slightly different radii ($R_1 \neq R_2$). The other geometry parameters and the currents of the force-reduced solenoids are the same ($L_1 = L_2$,

$w_1 = w_2$, $\gamma_1 = \gamma_2 = 45^o$). If the two layers are nested together, the co-axial 2-layer solenoid won't be force-reduced. The pitch angle of the second layer must be different than 45^o in order to obtain a force-reduced configuration with 2 layers (see table 3.2). For the two force-reduced monolayer solenoids the superposition principle would hold only if their radii would be the same ($R_1 = R_2$). This is equivalent of doubling the wires ($w = w_1 + w_2 = 2w_1$) in a force-reduced monolayer solenoid with $\gamma = 45^o$ (while maintaining equal spacing between the wires). It is also confirmed by figure 3.5: if high number of wires is doubled, the pitch angle remains 45^o for the force-reduced monolayer solenoid and the force-free field is maintained. The field and force of a monolayer force-reduced solenoid will be analyzed in the next chapter to gain more information.

Chapter 4

Force-Reduced Monolayer Solenoid

4.1 Pitch Angle of a Force-Reduced Monolayer Coil

The ideal pitch angle of a one layer helical winding is derived here using Ampere's law and Maxwell's stress equation. Then, the result will be compared to the pitch angle obtained from the optimization.

The coil of length L is made of w number of helical wires with common radius of R, and each carrying a current I. The γ pitch angle of the helical wires is measured from the cross-sectional plane (perpendicular to the axis of the coil). The field inside and outside of the magnet can be obtained easily by Ampere's law.

Field outside the magnet:

In this case the Ampere loop (for the line integral) is a circle with radius r > R, centered on the axis of the magnet. Because of symmetry reasons, the radial and axial field components are zero outside, away from the magnet. So, applying Ampere's law for the azimuthal field ($\mathbf{B}_{az}$):

$$\oint \mathbf{B}_{\mathrm{az}}\, \mathrm{d}\mathbf{l} = \mu_0 \cdot \mathrm{w} \cdot \mathrm{I}_{\mathrm{ax}},$$

where $\mathrm{I}_{\mathrm{ax}} = \mathrm{I} \cdot \sin\gamma$ is the current flowing in the axial direction.

Integration over the closed circular Ampere loop with radius r gives:

$$B_{az} = \frac{\mu_0 \cdot w \cdot I}{2\pi r} \sin\gamma \tag{4.1}$$

This is the magnitude of the azimuthal induction outside the magnet.

Field inside the magnet:

If n is the number of turns of each helix, the Ampere loop contains $n \cdot w$ number of helical turns along the total L_t length of the magnet. Along the axis, the radial and azimuthal components of the magnetic induction vanish for symmetry reasons.

Applying Ampere's law for the axial induction ($\mathbf{B}_{ax}$):

$$\oint \mathbf{B}_{ax} d\mathbf{l} = \mu_0 \cdot n \cdot w \cdot I_\varphi .$$

The azimuthal current that generates the axial field inside is: $I_\varphi = I \cdot \cos\gamma$, and the n number of turns is $n = L/L_p$ (L_p is the pitch length of the helices). After integrating over the total length, the Ampere's law results the axial field magnitude along the axis:

$$B_{ax} = \frac{\mu_0 \cdot w \cdot I}{L_p} \cos\gamma . \tag{4.2}$$

If $\gamma \to 0°$, then $L_p \to 0$ (since $L_p = 2\pi R \cdot \tan\gamma$). This is the ideal solenoid case, where the field becomes completely axial ($B_{az} = 0T$), according to equations 4.1 and 4.2. In case of one helical wire (w = 1), equation 4.2 results the familiar induction formula: $B_{ax} = \frac{\mu_0 \cdot n \cdot I}{L}$. If $\gamma \to 90°$, then $L_p \to \infty$, so the magnet consist straight conductors arranged around the circumference. In this case, according to equation 4.1 and 4.2, the field becomes completely azimuthal outside and the field inside is zero ($B_{ax} = 0$).

Pitch angle calculation for force-free case

After the derivation of the field components, one can apply Maxwell's stress equation which gives the total magnetic force acting on a finite body with surface S (Jefimenko 1989):

$$\mathbf{F} = \oint \mu\mathbf{H}(\mathbf{H}\cdot \mathrm{d}\mathbf{s}) - \frac{1}{2}\oint \mu \mathrm{H}^2 \mathrm{d}\mathbf{s}.$$

The field on the winding is perpendicular to the d**s** surface element of winding, so the first term in Maxwell's stress equation is zero. So, assuming constant μ: $\mathbf{F} = -\frac{1}{2\mu}\oint \mathrm{B}^2 \mathrm{d}\mathbf{s}$. Furthermore, on an element of the winding (see figure 4.1), only the outer and inner ΔS surfaces contribute to the total ΔF force on the element. Thus, the ΔF force magnitude on ΔS due to the magnetic pressure of the two field components is:

$$\Delta \mathrm{F} = \frac{\mu}{2}\left[-\left(\frac{\mathrm{w}\cdot \mathrm{I}}{2\pi \mathrm{R}}\sin\gamma\right)^2 + \left(\frac{\mathrm{w}\cdot \mathrm{I}}{\mathrm{L_p}}\cos\gamma\right)^2\right]\Delta \mathrm{S}.$$

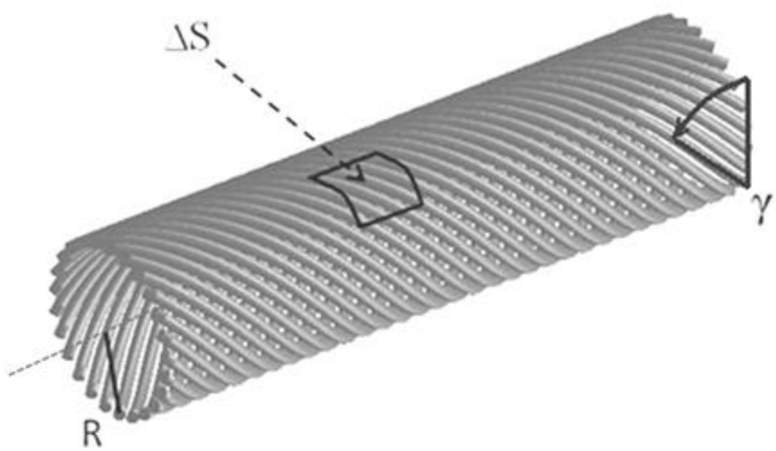

Figure 4.1 Schematic view of force-reduced monolayer winding obtained from the simulation. The pitch angle (γ) of the winding is 45 degree (see also figures 3.2 and 3.3).

In order to have a force-free coil, the magnetic pressure from outside must hold the magnetic pressure inside the magnet that tends to stretch the winding. So the equilibrium condition is:

$$\frac{w \cdot I}{2\pi R} \sin\gamma = \frac{w \cdot I}{L_p} \cos\gamma.$$

Since $L_p = 2\pi R \cdot \tan\gamma$, it results:

$$\tan\gamma = \cot\gamma.$$

Thus, for the coil to be force-free, the ideal pitch angle of the helices must be 45 degrees.

An optimization was performed on a sample magnet minimizing the κ angle between the current element vector and the induction vector on the wire elements. The main magnet parameters are given in table 4.1.

Table 4.1 Simulation parameters of the monolayer winding.

Radius	25 mm
Length	400 mm
Number of conductors	35
Current in each conductor	1000 A

The optimal pitch angle was found to be 45.6 degrees for this magnet. The small deviation from the ideal 45 degree is due to the relatively small number of filamentary wires. The distribution of κ angles on one wire filament along the length of the coil is shown on figure 4.2. By symmetry, it is sufficient to pick only one wire for plotting. As a comparison, helices with pitch angle other than 45.6 degree also shown (the other magnet parameters were the same as in table 4.1).

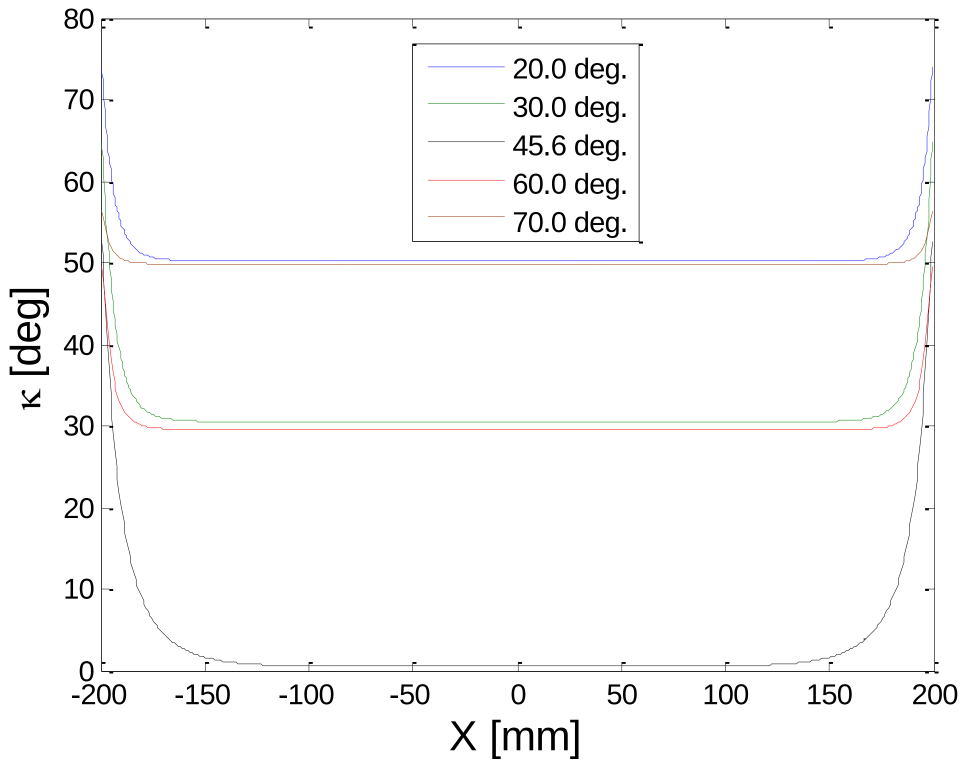

Figure 4.2 The κ angle distribution along the length of the winding for different pitch angle solenoids.

It is obvious, that at the ends of the ~45 degree pitch solenoid (and also for the others) the κ angle increase. This is due to the finite length of the coil. It is the end-effect problem of solenoids: at the ends of the coil the forces increase due to the stray magnetic field. The characteristics of the field and force distribution will be discussed next.

4.2 Magnetic Field of the Winding

4.2.1 Magnetic Field in the Bore

A simulation of magnetic field was performed in MATLAB on the 45.6 degree pitch angle magnet (with parameters given in table 4.1). The magnetic field distribution inside and outside the bore is shown on figure 4.3.

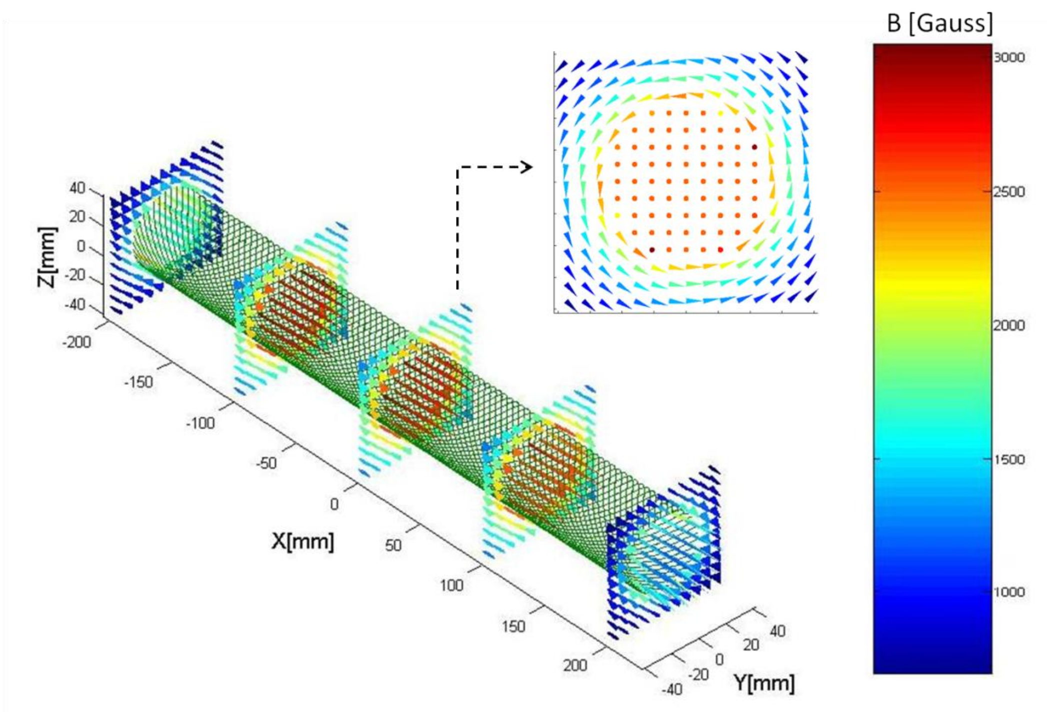

Figure 4.3 Magnetic field of a 45.6 degree pitch angle winding. An enlarged view of the field vectors in the cross-sectional midplane (at x = 0 mm) is also shown for clarity. The colorbar indicates the field magnitude. The parameters of the winding (green filaments) is given in Table 4.1.

Figure 4.3 clearly shows the main field components of a force-reduced monolayer solenoid: azimuthal field outside, and axial field inside the bore.

The azimuthal and axial field magnitude in the cross sectional midplane of the magnet (x = 0 mm) are shown on figure 4.4.

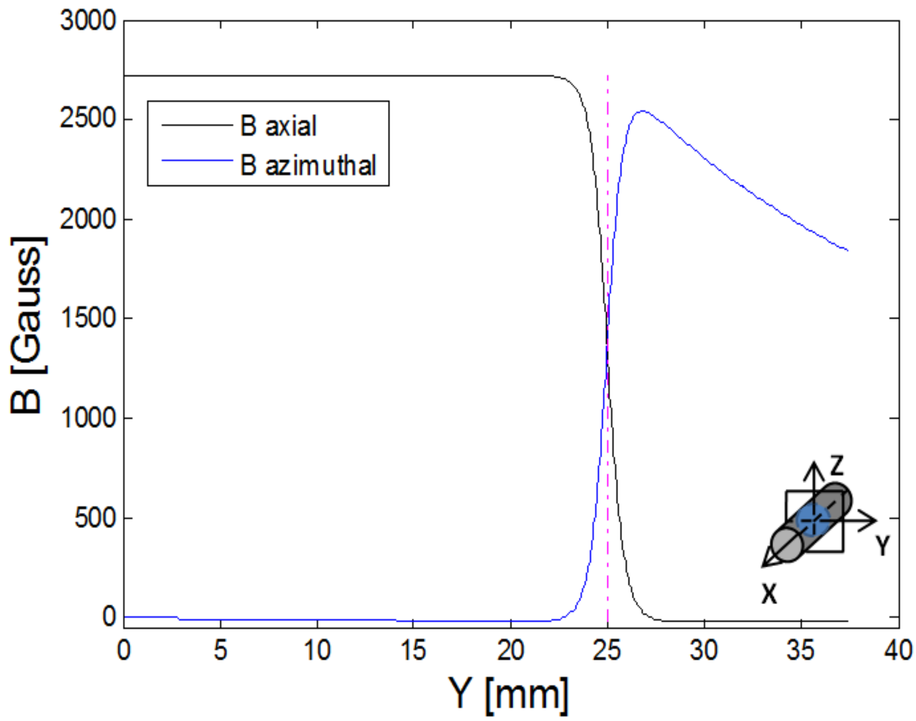

Figure 4.4 Axial and azimuthal field in the cross-sectional midplane (x = 0 mm and z = 0 mm) along the indicated y-axis. The magenta line indicates the position of the winding.

The winding is at R = 25 mm, marked by the magenta line. As it can be seen, at the vicinity of the winding the axial field magnitude (B_{ax}) is approximately equals to the azimuthal field magnitude (B_{az}). Using more wires, it can be shown that they are cloesly equal.

The on-axis axial field profile is shown on figure 4.5. As a comparison, solenoids with pitch angle other than 45.6 degrees are also shown (the other parameters, given in table 4.1, are the same). The ends of the solenoids are indicated by the magenta lines.

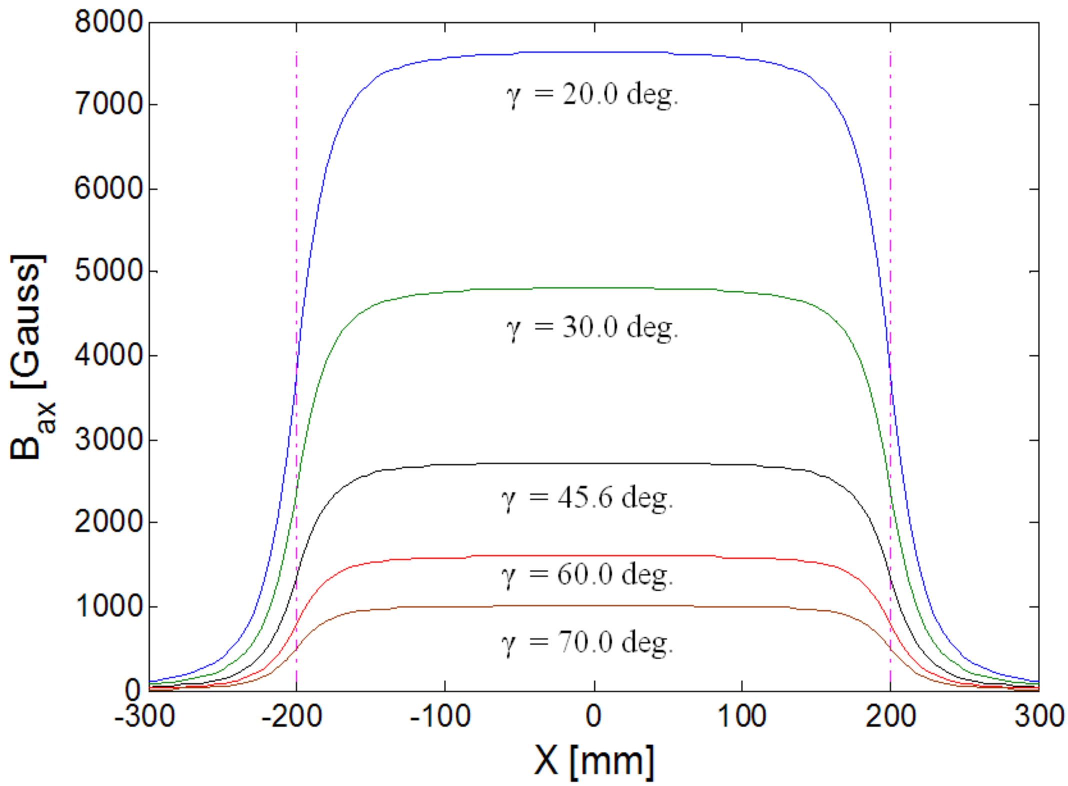

Figure 4.5 On-axis axial field profiles obtained from the simulation for different pitch angle solenoids. The magenta lines indicate the ends of the solenoid(s).

As a comparison, the axial magnetic field in the center of this magnet was also calculated using Ampere's law (eqn. 4.2) and the analytical formula (Smythe 1968):

$$B_{ax} = \frac{\mu_0}{4\pi}\frac{wI}{R}\left\{\frac{n\pi R\tan\gamma + d}{\left[R^2 + (n\pi R\tan\gamma + d)^2\right]^{\frac{1}{2}}} + \frac{n\pi R\tan\gamma - d}{\left[R^2 + (n\pi R\tan\gamma - d)^2\right]^{\frac{1}{2}}}\right\} \quad (4.3)$$

where d is the distance from the magnet center. The original formula was modified by the introduction of w in order to consider the number of helical filaments.

The calculated field values are shown in table 4.2 together with axial field value obtained from the simulation for the magnet center. It shows the good agreement of the fields obtained from the simulation and from the analytical form. The Ampere's law method provides only a rough estimation of the center field in the magnet.

Table 4.2 Axial field value calculations in the magnet center.

Calculation Method	**Axial Field (Gauss)**
$B_{0,ax}$ (from simulation)	2721.0
$B_{0,ax}$ (from eqn.4.3)	2720.8
$B_{0,ax}$ (from eqn.4.2)	1918.5

The current utilization of a magnet can be described by its transfer function. The transfer function (B/I) gives the generated field in the center of the bore per current flowing in the magnet. The transfer function was calculated from equation 4.3. Figure 4.6 shows the transfer function as function of pitch angle for several one layer solenoids with different number of wires.

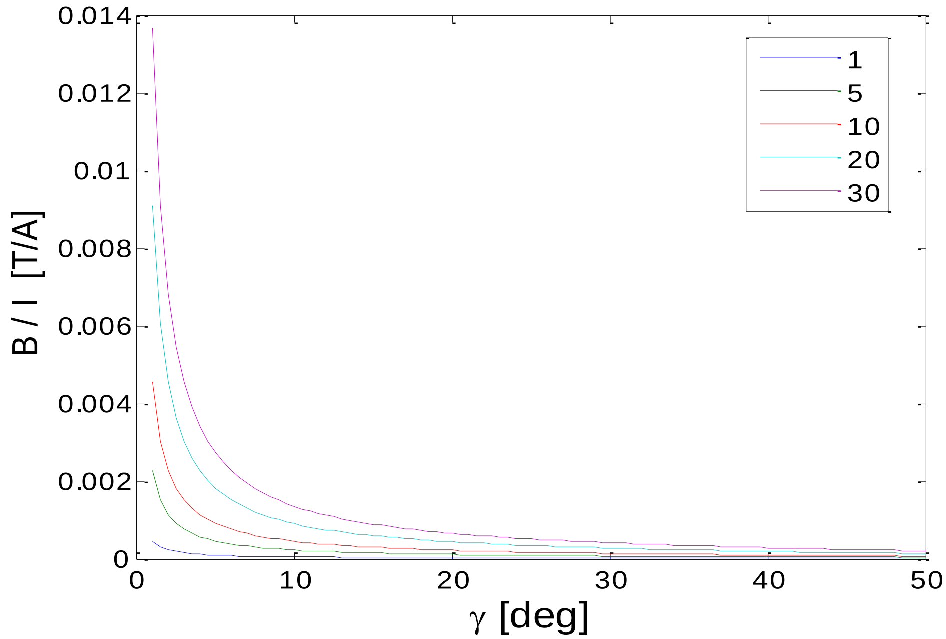

Figure 4.6 Transfer function as a function of pitch angle for five solenoids with different number of tilted wires.

At higher pitch angles, the transfer function drops significantly since the azimuthal current component in the solenoid is smaller and smaller. Compared to regular solenoids, the current utilization of force-reduced coils is worse, so more current is needed to generate the same axial field in the bore.

4.2.3 Magnetic Field at the Winding

Figure 4.7 shows the radial field on the winding for solenoids with different pitch angles (γ). The axial and azimuthal field on the winding for the same solenoids is shown on figure 4.8.

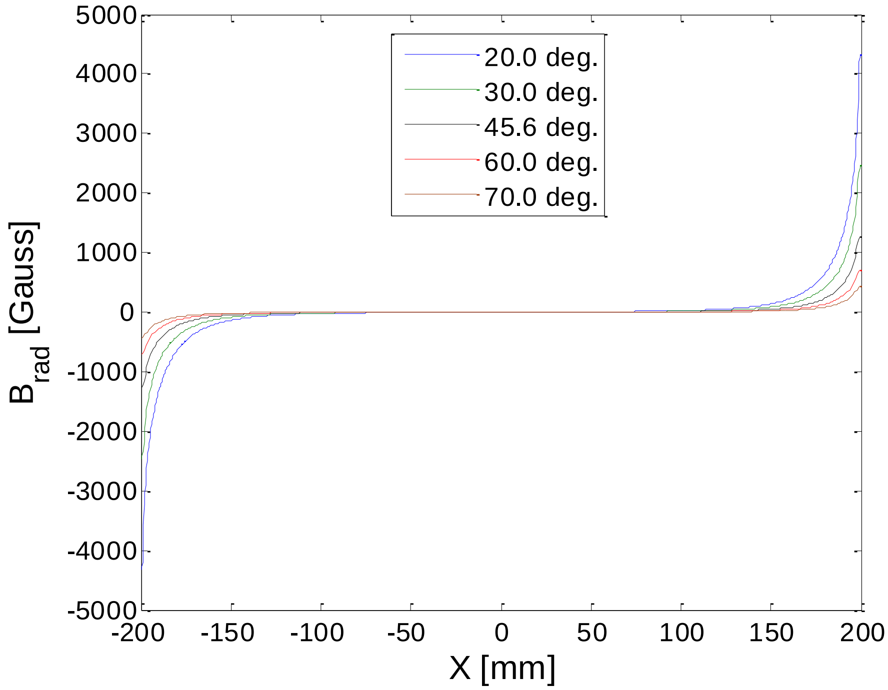

Figure 4.7 Radial field on the winding for five solenoids with different pitch angles.

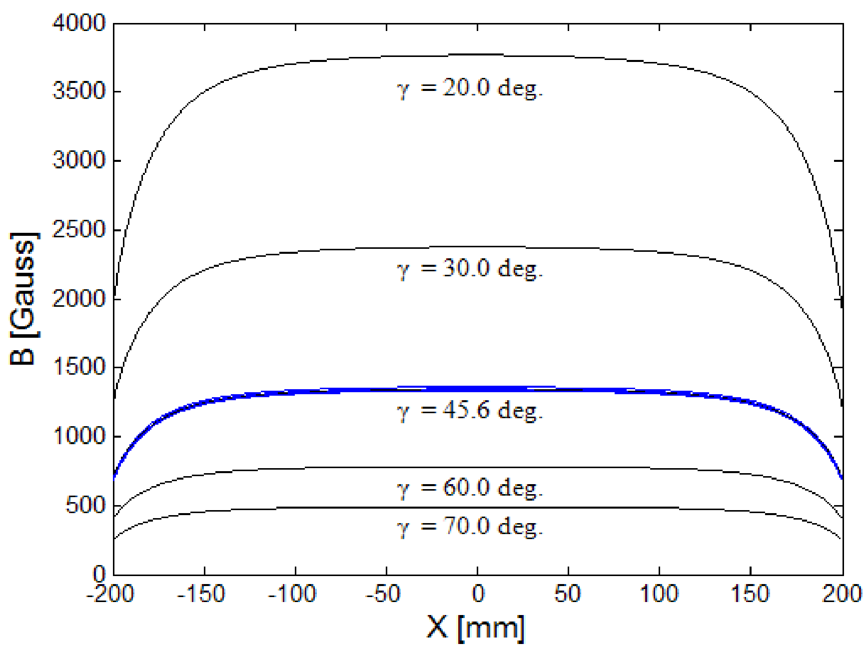

Figure 4.8 Axial field (black) and azimuthal field (blue) on the winding for solenoids with different pitch angles. The azimuthal field does not vary significantly with γ.

In agreement with the theory, the radial field increases at the ends (figure 4.7), due to the stray magnetic field. Solenoids with smaller azimuthal currents (higher pitch angles) have smaller radial fields at the ends of the magnet.

According to figure 4.8, the azimuthal field on the winding does not change significantly with the pitch angle of the wires in the coil. The azimuthal field on the winding is basically the same regardless of the pitch angle. This result (seemingly) is in contradiction with the result of the azimuthal field formula obtained from Ampere's law (eq. 4.1) that predicts γ dependence of B_{az}. The reason of this can be explained as follows.

Regardless of the pitch angle, the same current was required to flow in the wires. As one decreases the pitch angle of the wires, the azimuthal current component increases and the axial current component decreases, so their sum is always the total current. However, the number of turns along the length of the coil also increases with the decreasing pitch angle. This compensates the reduction of the axial current component, so the total axial current won't change along the length of the coil. The net axial current per unit length of the magnet will be the same regardless of the pitch angle if the total current per wire and the number of wires is the same. Therefore, due to the same axial current in the winding, the azimuthal field will be also the same.

As a summary of the field analysis, one can say that in the central zone of the winding $B_{ax} = B_{az}$ only if $\gamma = 45°$. If $\gamma < 45°$, the axial field is greater than the azimuthal field at the coil, so the bigger magnetic pressure inside tends to stretch the winding outward. If $\gamma > 45°$, the azimuthal field at the winding is greater than the axial field and it tends to compress the winding ("pinch effect"). In section 4.3 I will discuss the forces acting on the monolayer winding, and show their pitch angle dependence.

4.3 Forces on the Winding

4.3.1 Force Distribution on the Winding

Figure 4.9 shows the components and the magnitude of the Lorentz force acting on the winding of a force-reduced solenoid with pitch angle of 45.6 degrees (its parameters are given in table 4.1). The '3D' view of the force distribution on the winding is shown on figure 4.11. For the sake of visibility the number of wire elements was reduced (the filamentary wires are also shown on the figure in green).

For comparison, the same plots were generated for a solenoid that is able to produce approximately the same field in the center of the bore (figures 4.10 and 4.12). The number of turns of the solenoid was set so the length of the wire is equal to the total length of the wires in the force-reduced solenoid. The radius and the length of the solenoid were also set to the same as in the force-reduced case. The main parameters of the solenoid are summarized in table 4.3.

Table 4.3 Main parameters of the solenoid for comparison with the force-reduced solenoid.

Magnet Length (mm)	400
Radius (mm)	25
Number of Turns	85.8
Pitch Angle (deg.)	1.7
Current in the Wire (A)	1000

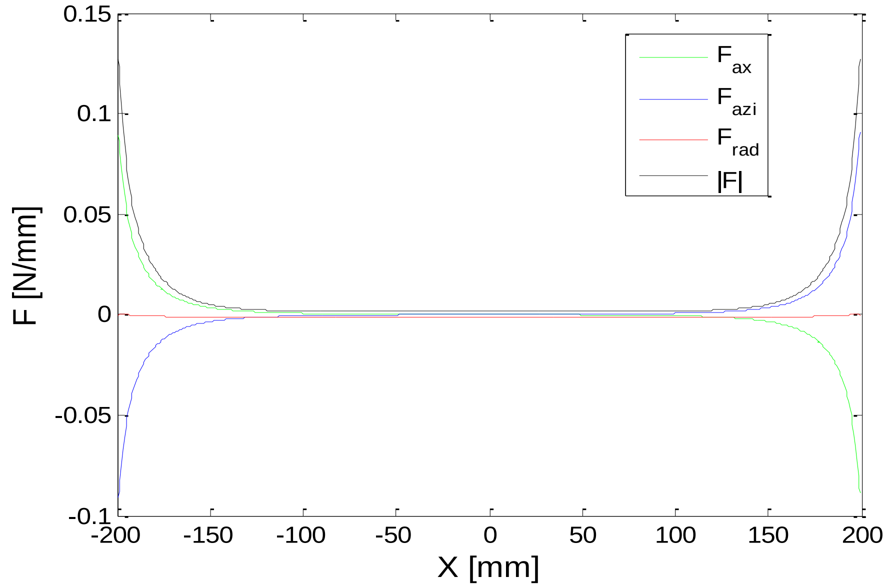

Figure 4.9 Lorentz force components acting on an individual conductor filament per unit length and its magnitude for the force-reduced solenoid.

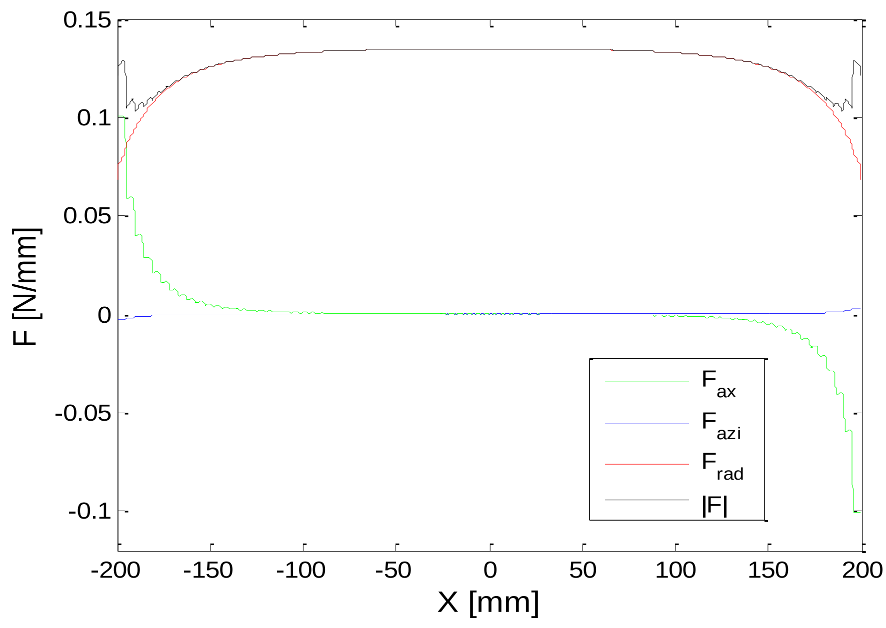

Figure 4.10 Lorentz force components acting on a conductor filament per unit length and its magnitude for the regular solenoid.

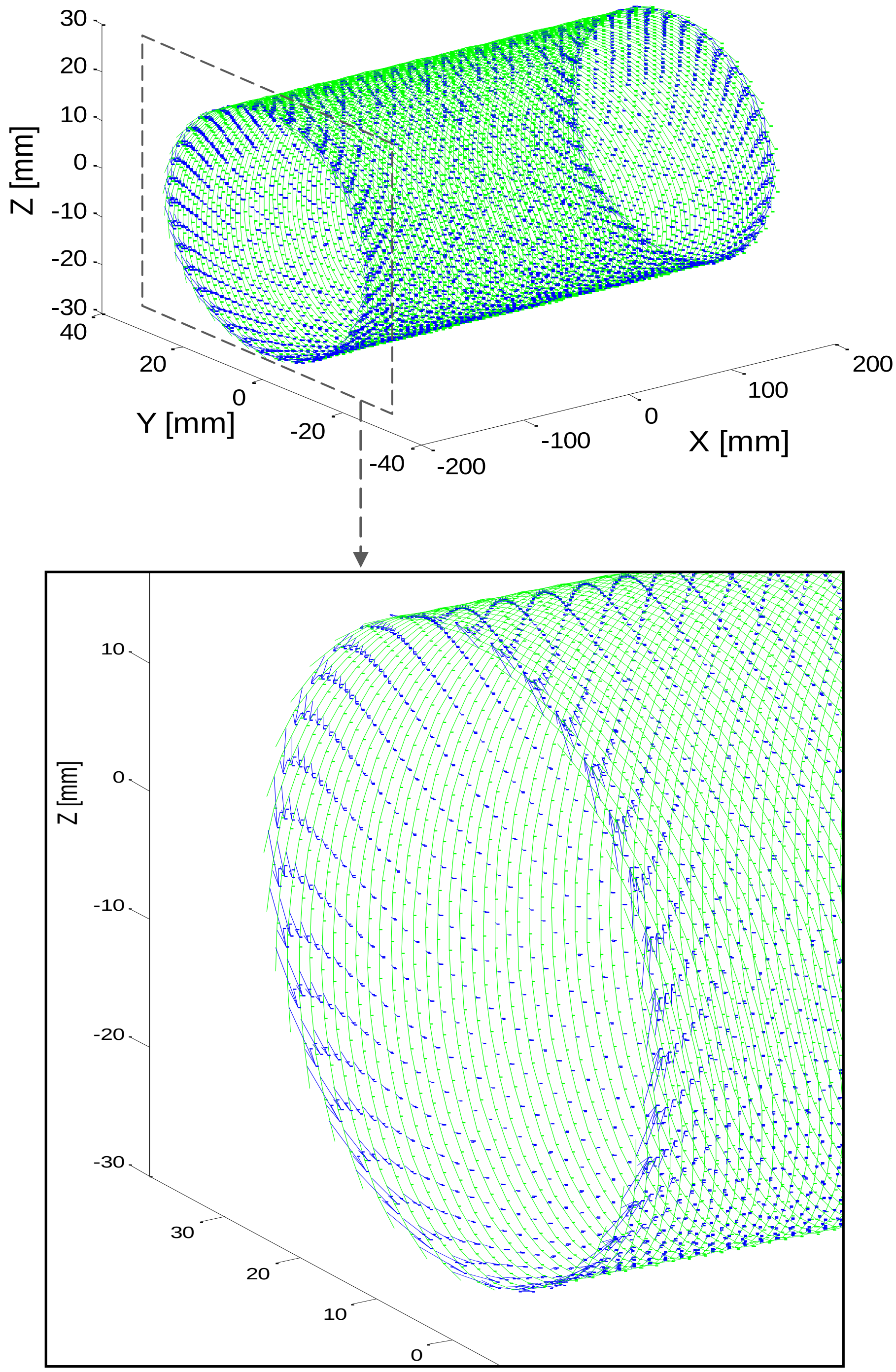

Figure 4.11 Distribution of force vectors (blue) on a force-reduced solenoid. The length of the vectors are proportional to the force per unit length acting at the position of the vector. For reasons of clarity an enlarged view of the coil end is also presented.

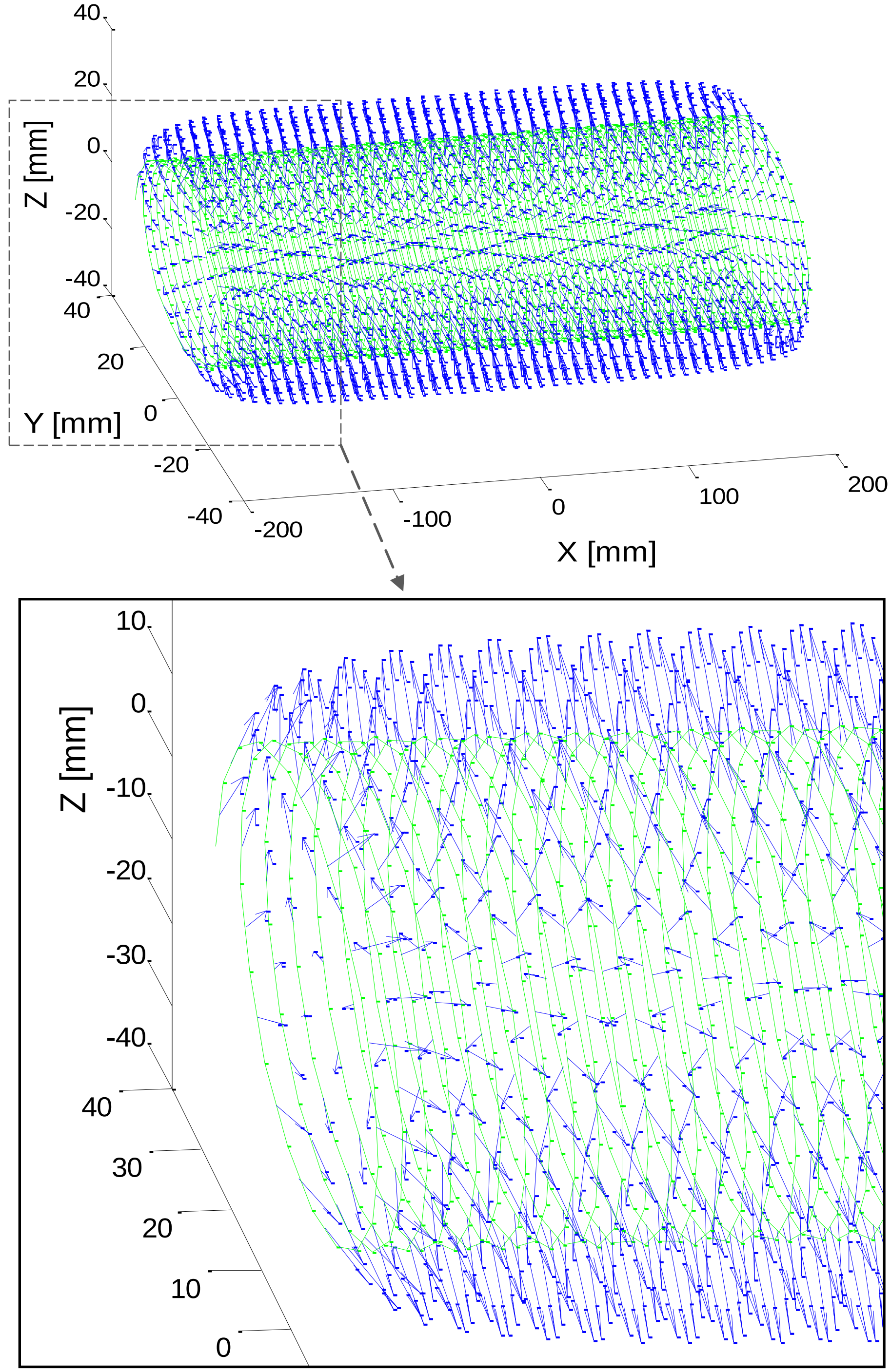

Figure 4.12 Distribution of force vectors (blue) on a regular solenoid. The length of the vectors are proportional to the force per unit length acting at the position of the vector. For reasons of clarity an enlarged view of the coil end is also presented.

4.3.2 Force Analysis

The main results of the force simulations and additional parameters are summarized in table 4.4 (subscript 'm' in the table indicates maximum value).

Table 4.4 Comparison of forces and additional parameters of a regular and a force-reduced solenoid. Subscript 'm' indicates maximum value.

	Regular Solenoid	Force-Reduced Solenoid
Pitch Angle, γ (deg.)	1.7	45.6
Current per Wire, I (A)	1000	1000
Number of Wires, w	1	35
Total Length of Wire (mm)	13483	19595
Field in Center, B_0 (Gauss)	2675	2721
$\lvert F\rvert_m$ (N/mm)	$1.349 \cdot 10^{-1}$	$1.271 \cdot 10^{-1}$
$F_{ax,m}$ (N/mm)	$1.006 \cdot 10^{-1}$	$8.890 \cdot 10^{-2}$
$F_{azi,m}$ (N/mm)	$3.000 \cdot 10^{-3}$	$9.080 \cdot 10^{-2}$
$F_{rad,m}$ (N/mm)	$1.349 \cdot 10^{-1}$	$2.455 \cdot 10^{-4}$

In regular solenoid windings the main (highest) force components are the radial force and the axial force. The outward radial forces, dominating in the middle zone of the coil (see figure 4.10), stretch the winding outward. The axial forces with opposite direction at the ends (see figure 4.10) compress the winding toward the midplane (x = 0 mm) of the magnet. This characteristic distribution of forces in a regular solenoid results the so called barrel-shape force distribution (see figure 4.12). As a note, the small jiggling of the force values on figure 4.10 is due to the relatively small number of winding turns.

For the force-reduced solenoid, the simulation confirms that the force cannot be everywhere zero on a finite length coil (in agreement with the Virial theorem). While the middle winding zone experience the highest forces in a regular solenoid, in the force-reduced case the high force region is shifted towards the ends of the coil. However, one must note that the higher forces act on a smaller range of the force-reduced coil compared to the regular solenoid.

The highest force magnitude is at the center of the solenoid (x = 0 mm). In this example of a regular solenoid, the force magnitude reduces only by ~0.3 % on 50 mm range along the axis measured from the center (x = 0mm). At a distance of 150 mm away from the center, the force magnitude is still ~93% of the maximum force magnitude. On the other hand, at the ends of the force-reduced solenoid the force magnitude is reduced by ~96 % on 50 mm range of the magnet length (measured from the end of the coil). This is a remarkable reduction of forces on a relatively short magnet (the aspect ratio was chosen so to reduce the end field effects).

Compared to the regular solenoid, the smaller size of the high force region and the large force reduction in the force-reduced solenoid suggest that less support structure can hold the forces at the ends. The main force component is also different than in the case of a regular solenoid. Besides the compressing axial forces, opposing azimuthal forces tend to twist the magnet at the ends of the force-reduced coil (see figures 4.9 and 4.11). It means that in the case of a force-reduced solenoid, the support structure must counteract the azimuthal and axial forces at the ends of the coil. In case of a regular solenoid the support structure must hold mainly the radial forces along a significant length of the coil (and the axial forces in addition).

Obviously, the number of tilted wires around the circumference of a solenoid is limited due to finite wire diameter. The limited number of discrete wires can explain the small deviation of the optimized pitch angle from the ideal 45 degrees pitch angle. Furthermore, if one considers the finite cross section of the wires, Kuznetsov also showed that helical wires with pitch angle of 45 degree and infinite length cannot be completely force-free. However, even with finite wire dimensions, approximately 45 degree coils can achieve a marked reduction of forces compared to other windings (Kuznetsov 1961). This was also confirmed by the simulation. In the central zone of a 45 degree helical winding the magnetic field is approximately force-free, and the force-free configuration is terminated at a point where the magnetic pressure on the winding is within the strength limits of the materials used in the magnet (Hand et al. 1962).

The current (hence the achievable field) in one layer windings is also limited by the heating of the coil due to the ohmic resistance of the conductor. Increasing the coil thickness is also not practical due to the accumulation of stresses. Therefore multilayer designs are better to reach higher magnetic fields (Montgomery 1969). This will be discussed in the next chapter.

Chapter 5

Conceptual Design and Analysis of a 25-T Force-Reduced Solenoid

The previous chapters showed the concept of force reduced solenoids. In this chapter the lessons learned will be applied to the design of a high field magnet. As a design goal a field strength of 25 T has been chosen. I will present the conceptual design of a multilayer pulsed magnet using a novel force-reduced solenoidal winding configuration. After introducing the features of the coil design, the main magnet parameters will be selected considering the field requirements and the maximum allowed current. In the next step, the magnetic field of the magnet will be analyzed inside and outside of the bore and also on the winding. Following the magnetic field analysis, force and heat analysis of the magnet will be discussed with considerations on cooling and conductor materials. The force characteristics of the conceptual force-reduced magnet will be compared to a regular, multilayer solenoid winding that would generate the same peak field in the bore.

5.1 Coil Design

5.1.1 Direct Conductor Design

The complex configuration of wires is a major drawback of force-reduced magnets considering other type of magnets. In force-reduced solenoids, many parallel wires with specified pitch angle must be wound and powered in more layers. Design and manufacturing of force-reduced solenoids are more challenging and, compared to force-reduced toroids, it is less discussed in the existing literature (see works of Shneerson et al.).

I propose a novel method to facilitate the design and manufacturing of force-reduced solenoids. In direct conductor design, the main current path is machined directly from the conductor material. Instead of using wires (placed on surfaces of supporting cylinders), the helical current paths of the force-reduced layers are milled in conductor tubes. Figure 5.1 shows the concept of a variable pitch direct conductor (VPDC) magnet. In each conductor layer the unmilled end-sections of the conductor tube connect together the helical conductor strips in parallel.

There are several advantages of this design method. Direct conductor method was already successfully applied for other type of magnets (Meinke 2009). The method allows to reach high current densities in the conductor, which is important in case of force-reduced solenoids. Besides the easier and more accurate manufacturing of the current paths, the method offers greater flexibility for setting the number of conductor strips in the layers. This method also allows easier application of more layers in order to reach higher fields. If necessary, the conductor strips can be further stabilized by filling the gaps with a strong, light-weight insulation material (like epoxy or G10). Without extra stabilizers between the conductor strips in a layer, the gaps can be used as additional cooling passages to increase cooling efficiency.

Figure 5.1 Concept of the variable pitch direct conductor (VPDC) magnet. The top figure shows individual layers with different pitch angles. The lower figure shows how such layers can be combined to form a force-reduced structure with increased field strength.

5.1.2 Return Current Zone and Solenoid End-Region

To form a more compact solenoid, the currents can be returned at the end of the force-reduced VPDC magnet. The return currents can be established by wires connected to the ends of the VPDC magnet layers. This combined magnet can be separated into three zones (Shneerson et al.): 1. the inner zone of nested, force-reduced layers; 2. the outer return current zone; 3. the solenoid end-region where the inner and outer current zones are connected. The scheme of the current zones is shown on figure 5.2.

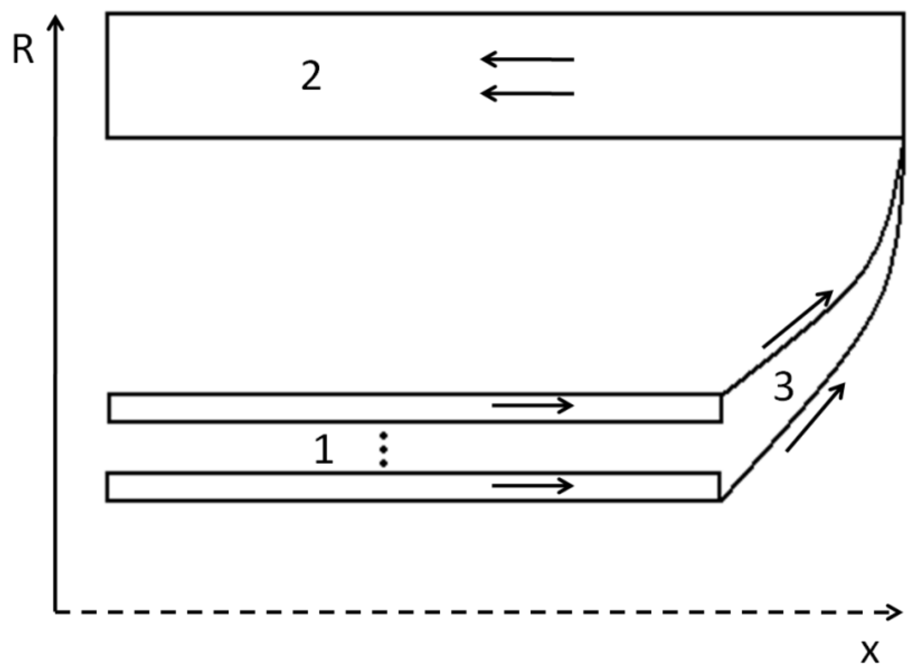

Figure 5.2 Schematic picture of the current zones of a system with high field force-reduced central part and a low field return section, where forces are easily supported (after Shneerson et al. 1998). The dashed line indicates the solenoid axis.

In the solenoid end-region, curved wires can be used to connect the inner force-reduced layers to the return current layers. The ideal (force-reduced) curvature of the wires can be determined and it was obtained by Shneerson et al. by degenerating the force-free layers into a curved surface (see figure 5.2). The return currents can flow in the axial direction (Shneerson et al.), so their field won't disturb the quasi-force-free field configuration of the inner force-reduced layers. However, since these axial backward currents are located in the azimuthal field region of the inner layers, the return current zone layers won't satisfy the force-free condition. Because the azimuthal induction of the force-reduced inner layers decreases as 1/r or faster, the return currents won't experience high forces, and dielectric cylinders can hold the wires. Furthermore, the radii of these outer layers can be adjusted so they will be equally loaded (Shneerson et al. 1998).

5.1.3 Magnet Parameters

The parameters of the force-reduced solenoid are dictated by required maximum field in the bore and the maximum allowed current in the conductor strips. The bore diameter was set to be 50 mm. Copper was chosen as conductor material. Due to the low transfer function (and therefore the required high currents), the magnet should operate in pulsed mode.

In force-reduced solenoids the maximum allowed current density is limited by heating of the conductors rather than stress in the magnet (Shneerson 2004). From the thermal conditions, the maximum allowed current density (or current) can be determined for a desired current pulse characteristic (see thermal analysis). In view of the allowed current density and the desired field, the required number of layers (N) and the number of conductor strips per layer (w) can be determined. The total number of layers was selected to be three.

It was pointed out in section 3.4.2 (see also figure 3.5), that the number of conductor strips (w) should be selected as large as possible, to get a better force-free field distribution. The maximum number of conductor strips in a given layer is determined by the azimuthal width of the strips, the required spacing between the strips, the inner radius of the layer, and the pitch angle of the conductors. In addition to these geometrical constraints on the number of tilted conductors in a layer, one must also consider the maximum allowed current density in each wire. According to this, the number of conductor strips in each layer was determined. The spacing between the conductor strips in a layer is about 1 mm.

The lengths of the layers are equal, and they were adjusted in order to get a good high field region around the center of the bore (reducing the disturbing end-effects). The wall thickness (th) of the conductor tubes were set to be equal (3 mm each). The spacing between the tubes was also set to be equal (1 mm). The parameters of each layer are summarized in table 5.1. The first layer (layer 1) is the innermost layer.

Table 5.1 Main parameters of a 25-T force-reduced VPDC magnet.

Parameter (unit)	Layer 1	Layer 2	Layer 3
Center radius, R_c (mm)	26.5	30.5	34.5
Length (mm)	600	600	600
Pitch angle, γ (degrees)	75.47	47.99	17.66
Number of conductor strips per layer, w	49	44	21
Current per conductor strip, I (A)	34100	34100	34100
Conductor width, d (mm)	2.1	2.3	2.3
Conductor thickness, th (mm)	3	3	3
Current density per conductor strip (10^9 A/m^2)	5.4	4.9	4.9

The pitch angles of the layers were obtained by optimization, as it was described in chapter 3. The distribution of the κ angles is shown on figure 5.3. It shows that the angle between the current element vectors and **B** is minimized for all layers in the central zone along the length.

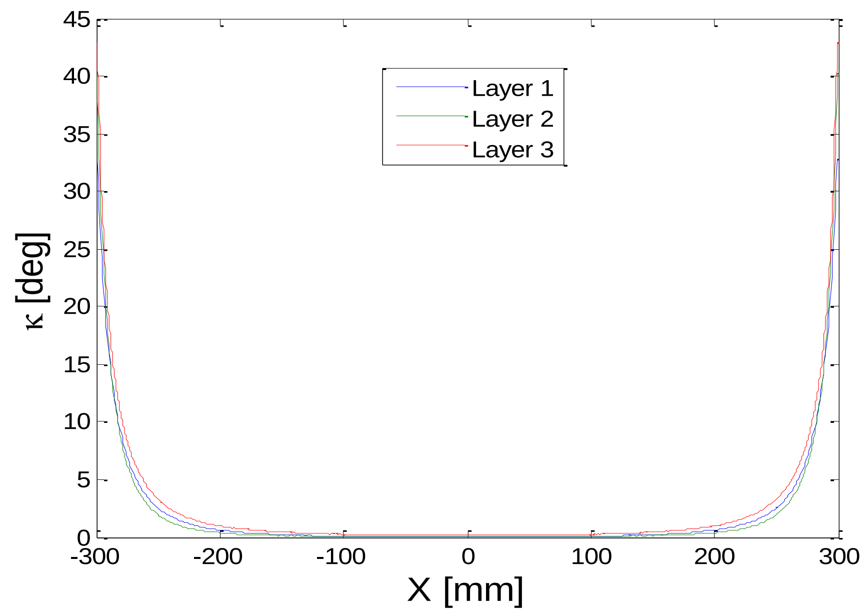

Figure 5.3 The κ angle distribution along the length of the 3-layer VPDC solenoid.

5.2 Magnetic Field Analysis

5.2.1 Magnetic Field in the Bore

The main field components are the axial field (dominating inside the bore) and the azimuthal field (dominating outside the bore). Figure 5.4 shows the variation of these components in the cross sectional midplane (at x = 0 mm) of the VPDC.

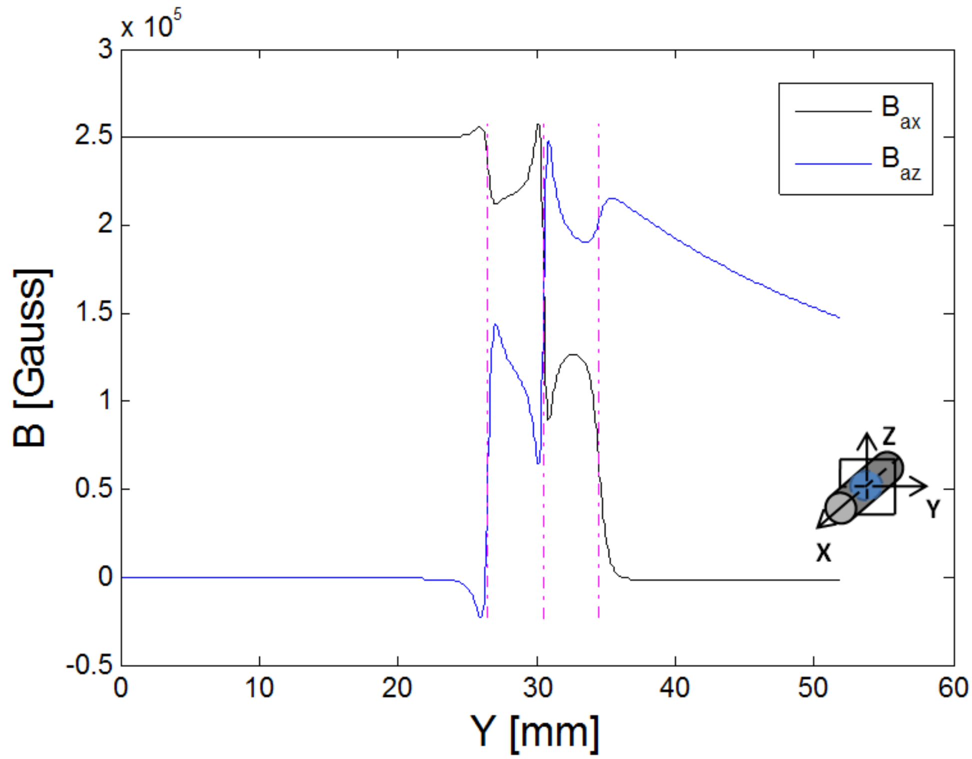

Figure 5.4 Axial and azimuthal field in the cross-sectional midplane (at x = 0 mm and z = 0 mm). The magenta lines (at R_c = 26.5, 30.5, 34.5 mm) mark the position of the layers.

According to figure 5.4, the axial field (in average) decreases through the winding from its maximum value (inside) to zero (outside the magnet). The azimuthal field increases (in average) with the radius until the outermost layer, then (outside) it starts to drop with increasing radial distance from the axis.

Figure 5.5 shows the on-axis field profile of the axial field.

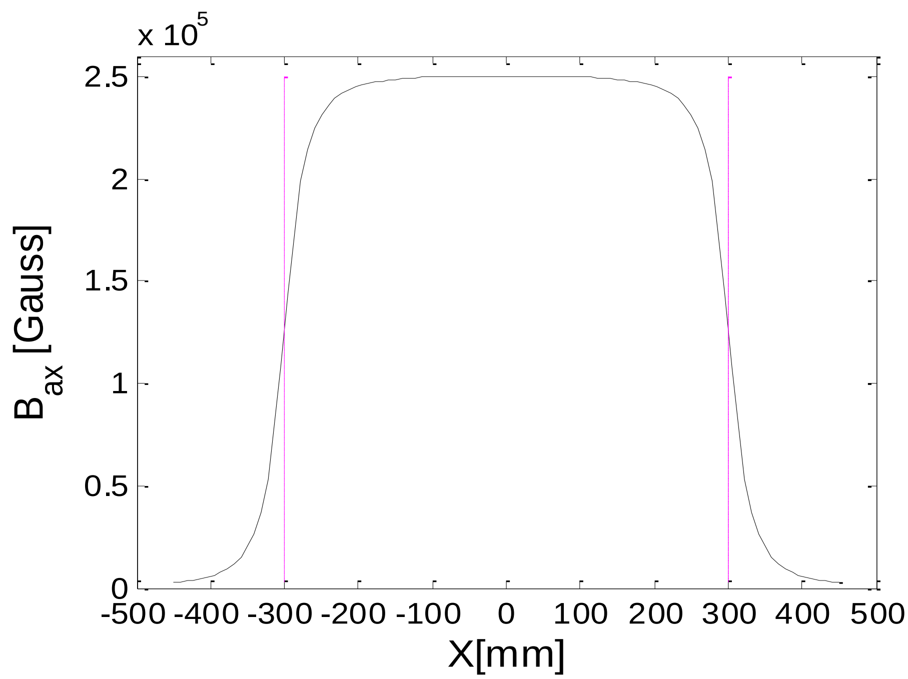

Figure 5.5 On-axis axial field of the 3-layer VPDC magnet. The magenta lines mark the ends of the layers.

From the simulation the maximum axial field generated in the center of the magnet is 25.028 T. In comparison, the axial field in the center obtained from the analytical formula (eq. 4.3) is 25.027 T. The field values are in good agreement.

5.2.2 Magnetic Field at the Winding

The radial, axial and azimuthal field components on the each layer are shown in figure 5.6, 5.7 and 5.8, respectively. Only one filamentary wire was selected from each layer for plotting and x indicates the axial coordinates of the wire elements.

The radial field component (B_{rad}) varies only at the ends of the layers, and its values are basically the same in the three layers (see figure 5.6). The axial field component (B_{ax}) is different in the three layers, and the same is true for the azimuthal field (B_{az}). In accordance with figure 5.4, the axial field on the winding has its highest value in the innermost layer and the outer layers experience lower axial field. The opposite is true for the azimuthal field component: B_{az} has its highest value in the outermost layer and its lowest value in the innermost layer.

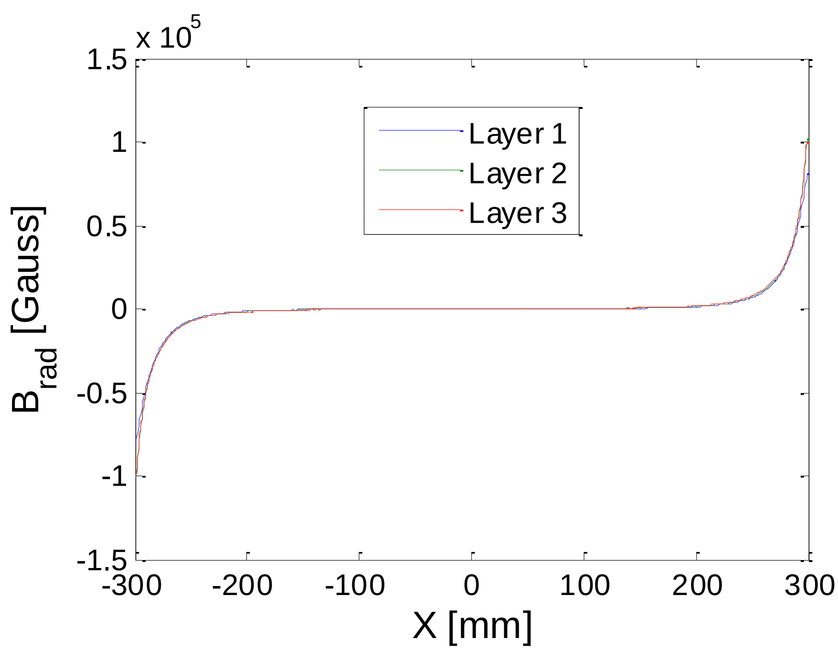

Figure 5.6 Radial field versus axial position on the winding layers of the VPDC solenoid.

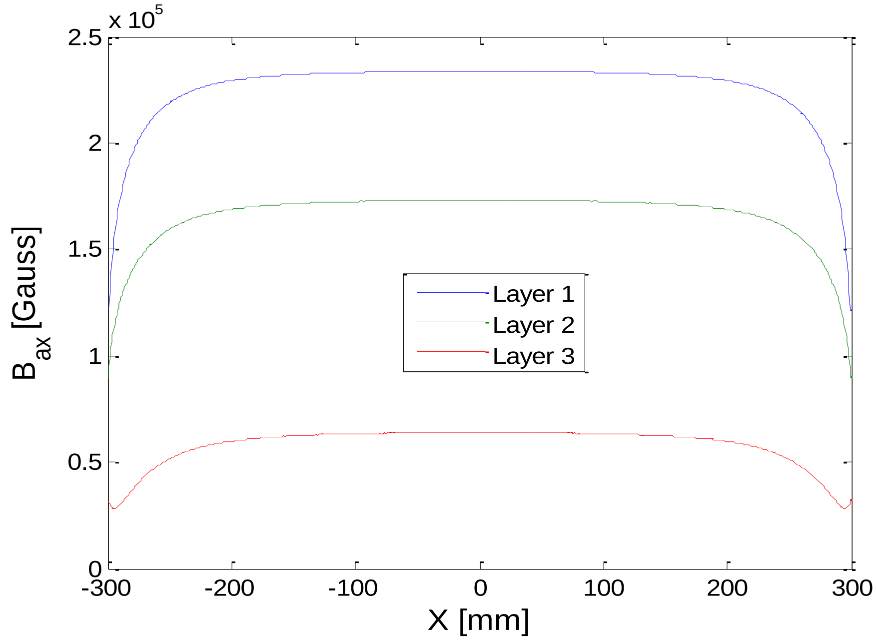

Figure 5.7 Axial field versus axial position on the three layers of the VPDC solenoid.

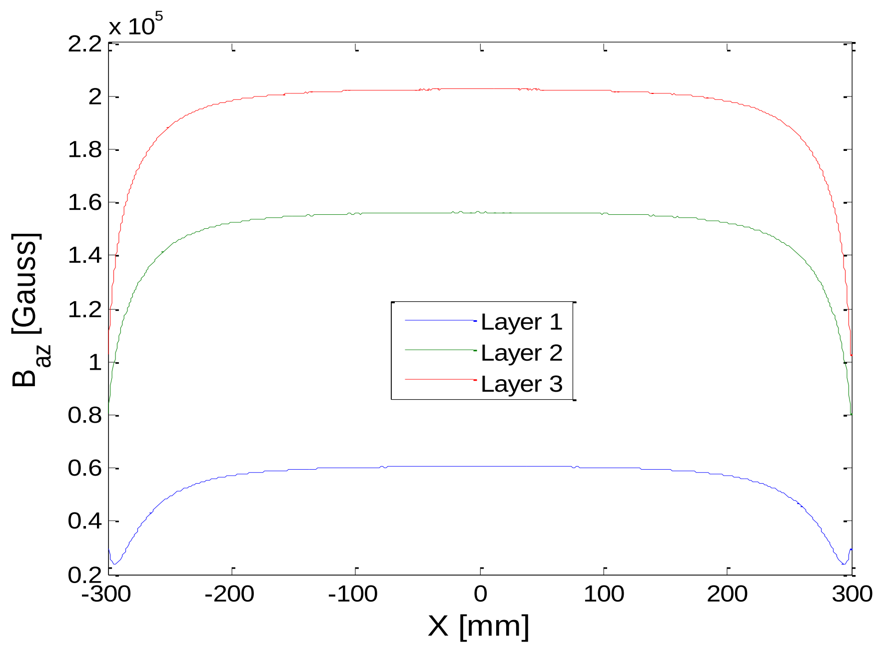

Figure 5.8 Azimuthal field versus axial position on the three layers of the VPDC solenoid.

5.3 Mechanical Design

5.3.1 Force Analysis

The force magnitude along the length of each layer is shown on figure 5.9. The force components in cylindrical coordinates are shown on figures 5.10 - 12. Force values are given as force per unit length of wire element.

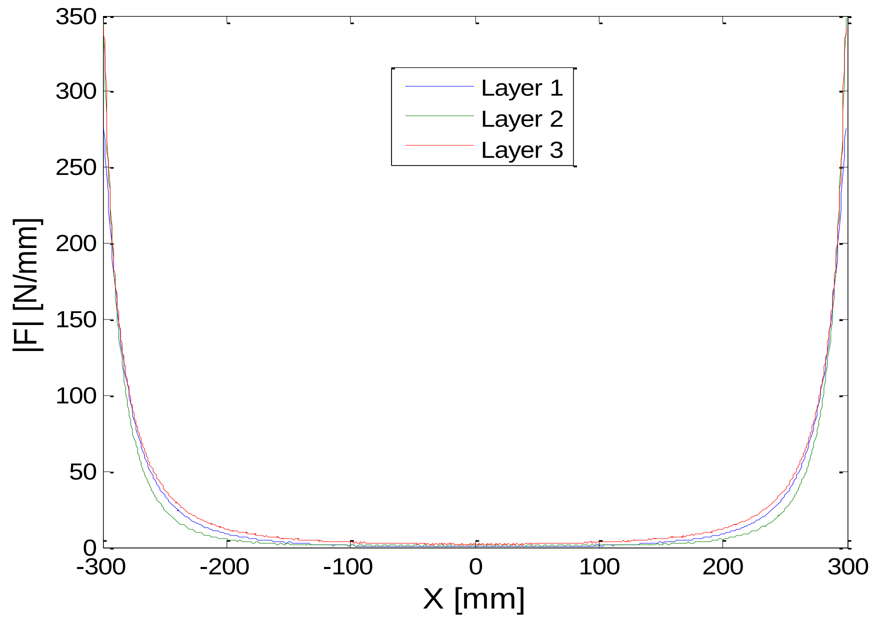

Figure 5.9 Force magnitude per unit length on each layer along the length of the VPDC solenoid.

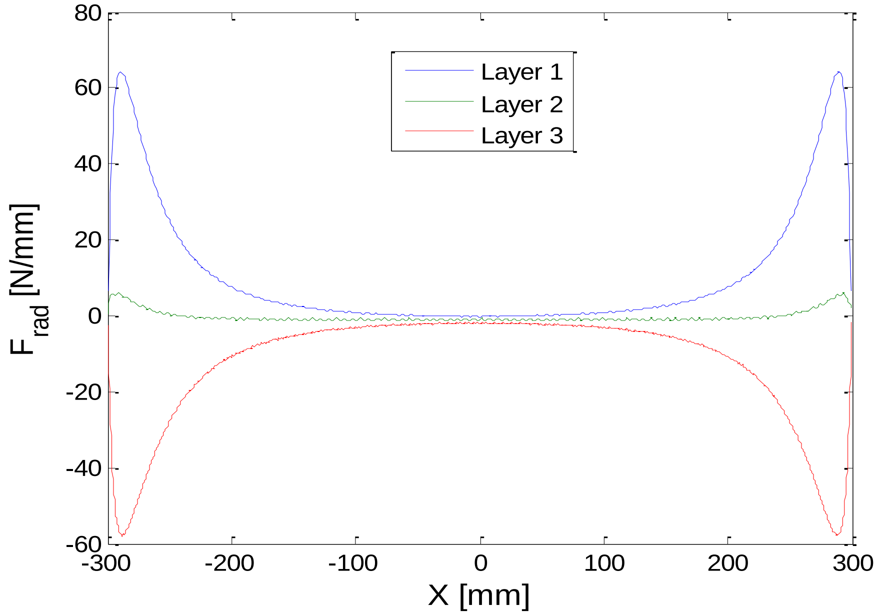

Figure 5.10 Radial force per unit length on each layer along the length of the VPDC solenoid.

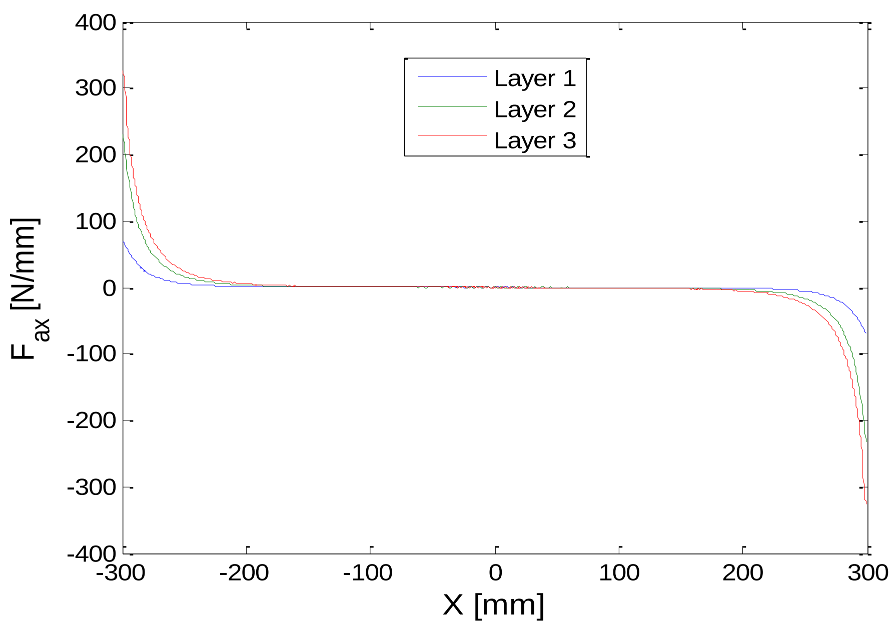

Figure 5.11 Axial force per unit length on each layer along the length of the VPDC solenoid.

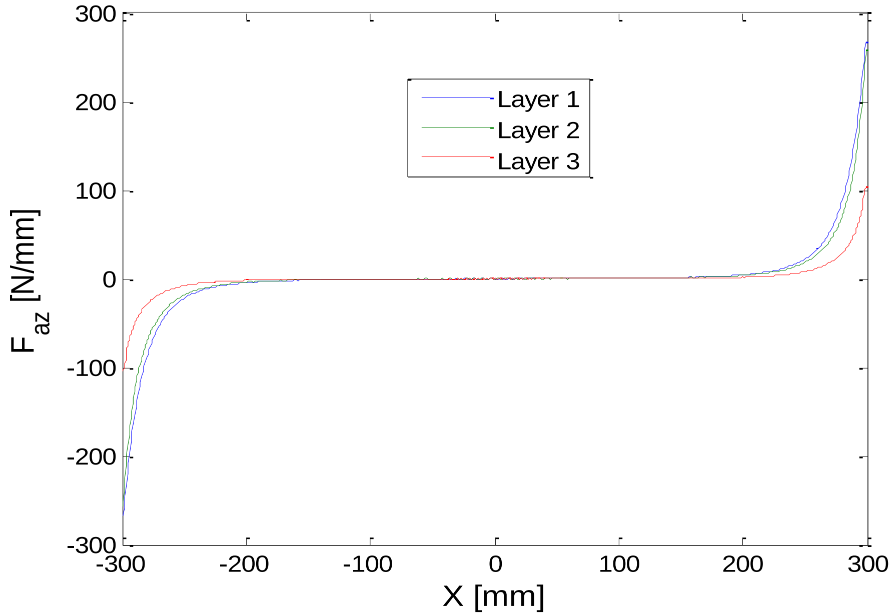

Figure 5.12 Azimuthal force per unit length on each layer along the length of the VPDC solenoid.

In agreement with the obtained κ angle distribution (figure 5.3), the force is reduced in the central zone of the winding. At the ends of this force-reduced magnet, the radial force is tensile (positive) for the innermost layer. In the middle layer, the radial force is still tensile at the ends but it is much smaller in magnitude. The tensile force of the inner two layers is compensated by the third layer where the radial forces are compressive (see figure 5.10). This reason of this radial force balance will be discussed later.

The stray field at the ends gives rise to the axial and azimuthal force components. Due to the opposite radial field component at the ends (see figure 5.6), opposing axial forces act on the azimuthal current component. These opposing axial forces tend to compress the winding just like in regular solenoids. Since the radial field is almost the same in the layers, while the azimuthal current component is higher in the outermost layer(s), thus the axial forces (in absolute value) are also higher in the outermost layer(s) (see figure 5.11). The azimuthal force at the ends acting on the axial current component is also due to the radial field. The axial current component is relatively smaller in the outer layer(s), hence the azimuthal force (in absolute value) is also smaller in the outer layers (see figure 5.12).

The increased axial and azimuthal forces at the ends must be supported. The compressive axial forces can be supported for example by inserting massive rods outside, fixed between the end-tubes of the VPDC solenoid. These support rods can also provide some support against the torsion due to the azimuthal forces at the ends. If necessary, additional crossbars can be applied at the end-tubes to hold the torque.

Force Balance

It is possible to check the force balance in the middle zone of each layer. The force balance of the axial and azimuthal forces in the middle zone of the winding is trivial since the radial field in the middle zone of the layers is practically zero (see figures 5.6, 5.11 and 5.12).

The balance of tensile and compressive radial forces can be expressed in a simplified way with their magnitude:

$$I_{az} \cdot B_{ax} \cdot l = I_{ax} \cdot B_{az} \cdot l,$$

where l is the length of the wire element vector in the middle of the winding. The tensile radial force acting on the azimuthal current (I_{az}) is due to the axial field (B_{ax}), while the compressive radial force acting on the axial current (I_{ax}) is due to the azimuthal field (B_{az}).

The azimuthal and axial current in each layer can be expressed with the pitch angle of the layer as: $I_{az} = I \cdot \cos\gamma$ and $I_{ax} = I \cdot \sin\gamma$. In the simulation, the I transport current in the wires were set to be equal, and the wire elements have also approximately the same l length, so the radial force balance equation reduces to:

$$B_{ax} \cdot \cos\gamma = B_{az} \cdot \sin\gamma \tag{5.1}$$

Table 5.2 shows this calculation for the balance of radial force. The table also includes the maximum values of the azimuthal and axial field components in the middle zone of the layers (see also figures 5.7 and 5.8).

Table 5.2 Axial and azimuthal fields showing the high degree of radial balance between the two when the pitch angles are considered. This balance is responsible for the achieved force compensation.

Parameter (unit)	Layer 1	Layer 2	Layer 3
$B_{ax,m}$ (T)	23.37	17.30	6.39
$B_{az,m}$ (T)	6.06	15.63	20.26
Pitch angle, γ (degrees)	75.47	47.99	17.66
$B_{ax} \cdot \cos\gamma$ (T)	5.86	11.58	6.09
$B_{az} \cdot \sin\gamma$ (T)	5.87	11.61	6.15

Equation 5.1 explains how the axial and azimuthal fields relate to each other in a given layer of a multilayer force-reduced solenoid. This is also in agreement with the one-layer force-reduced solenoid, since in that case $\sin\gamma = \cos\gamma$ and $B_{ax} = B_{az}$ on the winding.

5.3.2 Stress Analysis

A stress simulation was performed to approximate the stress due to the radial forces on the layers. The equivalent von Misses stress was simulated in SolidWorks, using the radial force components obtained from the MATLAB code.

For symmetry reasons, the half of the total length was simulated. Each conductor tube was subdivided along the length into a series of smaller length tubes. From the radial force values, average pressure values were calculated on each of the tube sections. The layers were separated with G10 in the simulation. The magnet was also overwrapped with a thin (1 mm thick) layer of G10 to apply boundary condition on that (it was assumed to be fixed in the simulation). The obtained equivalent von Misses stress distribution is shown on figure 5.13.

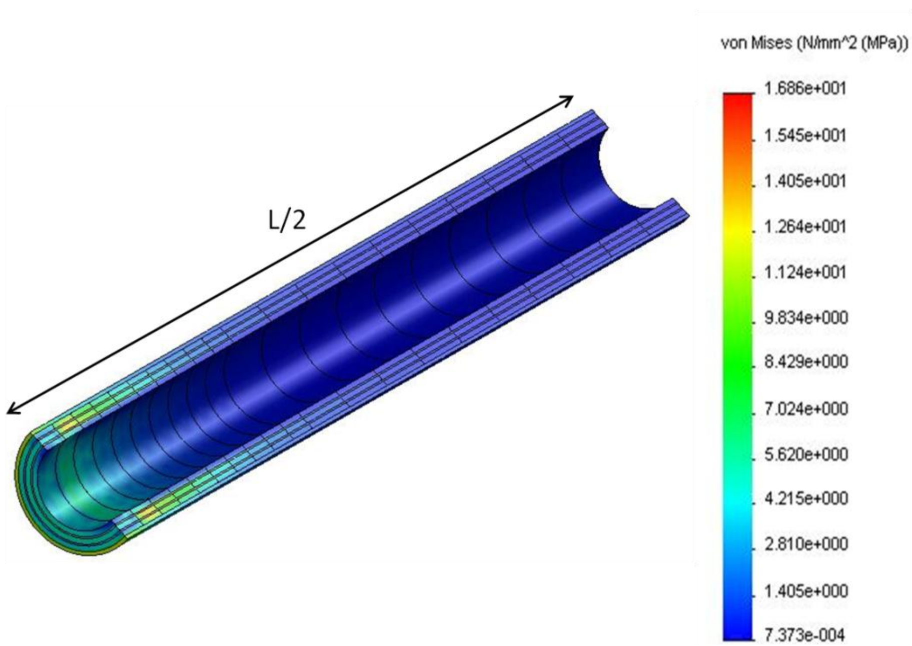

Figure 5.13 Estimated stress distribution in a 25 T VPDC magnet. The stress value is color-coded, with values indicated in the color bar.

Note that in the simulation full (not grooved) tube sections were applied, so higher pressures can be expected, but the values give a rough estimation on pressure.

5.3.2 Comparison of the Layers

It is worthwhile to compare the layers in the case when each layer is energized independently, in absence of the other two layers. The input parameters of the layers were the same as in table 5.1. The results for the generated field in the center (B_0), the transfer function and the forces can be also compared to the force-reduced case, when all the three layers are nested. Table 5.3 contains a summary of the main results (index 'm' indicates the maximum value).

Table 5.3 Comparison of field, forces and transfer functions for individual and nested VPDC magnet layers.

Parameter (Unit)	Layer 1	Layer 2	Layer 3	Nested Layers
B_0 (T)	3.2554	8.8160	12.955	25.027
B / I (10^{-6} T/A)	1.95	5.88	18.09	6.44
$\|F\|_m$ (N/mm)	188.49	149.97	241.95	349.38
$\|F_{rad}\|_m$ (N/mm)	188.49 (compressive)	20.82 (compressive)	188.85 (tensile)	64.42
$F_{ax, m}$ (N/mm)	13.41	100.11	210.69	326.63
$F_{az, m}$ (N/mm)	51.76	111.15	67.07	267.55

As it can be seen, the transfer function of the third layer is the largest. This layer provides more than half of the total field in the center when the three layers are nested together. The transfer functions of the inner two layers are smaller. Their main role is to generate azimuthal field in the outer sections for force reduction.

Layer 2 in itself is close to a force-reduced solenoid, since its pitch angle (~48 degree) is close to 45 degree. This explains the relatively small compressive radial force compared to the other layers. When the three layers are nested together, the significant reduction of radial forces is obvious. Compared to the nested case, the tensile force in layer 1 and 2 are much higher when they are energized alone, although their fields in the center are much lower than 25 T.

5.3.3 Comparison with a Regular Solenoid

A three-layer regular solenoid was also simulated to compare the forces on its layers with the forces on the three-layer force-reduced magnet.

This sample solenoid contains one wire in each layer, and in each wire the same current was used as in the force-reduced example. The lengths and radii of the layers are also the same as for the force-reduced magnet (see table 5.1). The pitch angles (or the number of turns) were adjusted in each layer, so the solenoid generates (intentionally) a little bit less than 25 T. The number of turns for layer 1, 2 and 3 are: 109, 112 and 122, respectively. For comparison, the results are summarized in table 5.4.

Table 5.4 Comparison of fields, forces and transfer functions of a regular solenoid with the force-reduced VPDC solenoid.

Parameter (Unit)	Regular Solenoid	Force-Reduced Solenoid
B_0 (T)	24.346	25.027
B / I (10^{-6} T/A)	237.99	6.44
$\lvert F\rvert_m$ (N/mm)	703.27	349.38
$\lvert F_{rad}\rvert_{m}$ (N/mm)	703.27	64.42
$F_{ax,\ m}$ (N/mm)	280.07	326.63
$F_{az,\ m}$ (N/mm)	9.06	267.55

Figure 5.14 show the force magnitude and its components (per unit wire length). As a note, the small jiggling in the force values is due to the relatively small number of turns in the layers.

In comparison, the significant reduction of radial forces in the force-reduced VPDC magnet is obvious. In the regular solenoid example, all the radial forces are tensile and that must be supported somehow. In the force-reduced case, the radial forces are smaller and compensate themselves between the layers. However, there is a significant difference in azimuthal forces. In the force-reduced configuration, the azimuthal forces rise to higher values compared to a regular solenoid.

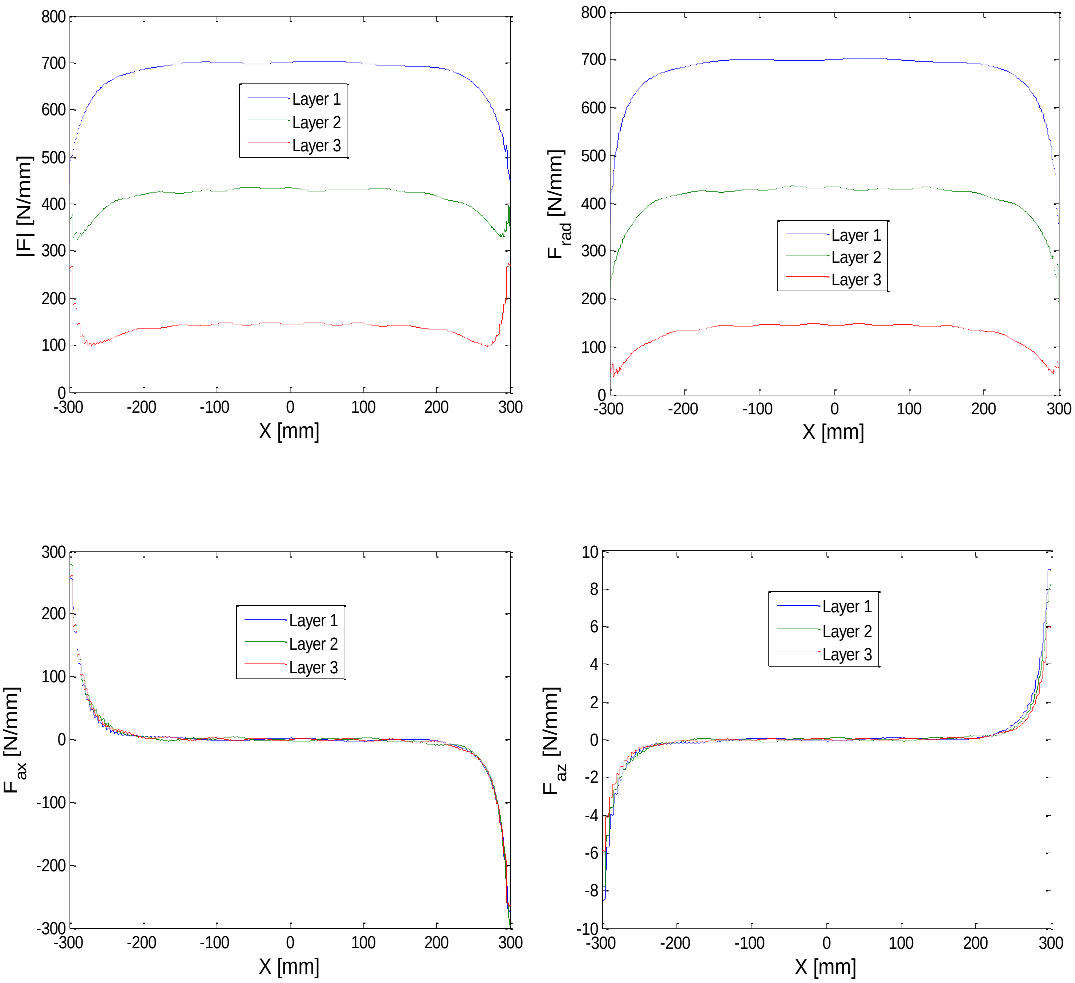

Figure 5.14 Force magnitude and its components per unit wire length in a three-layer regular solenoid as a function of axial position.

5.4 End-Effects

A possible way to reduce the force on the winding at the ends is to change the length of the layers relative to each other. Staggered layers are often applied in the design of nested solenoid magnets.

For the three layer VPDC magnet, four basic cases can be distinguished (see figure 5.15). In the first two cases (A and B), only the length of the middle layer is changed while the 1^{st} and 3^{rd} layer has the same length. In case C the length of the layers increase with the radius, while in case D the length of the layers decrease with radius.

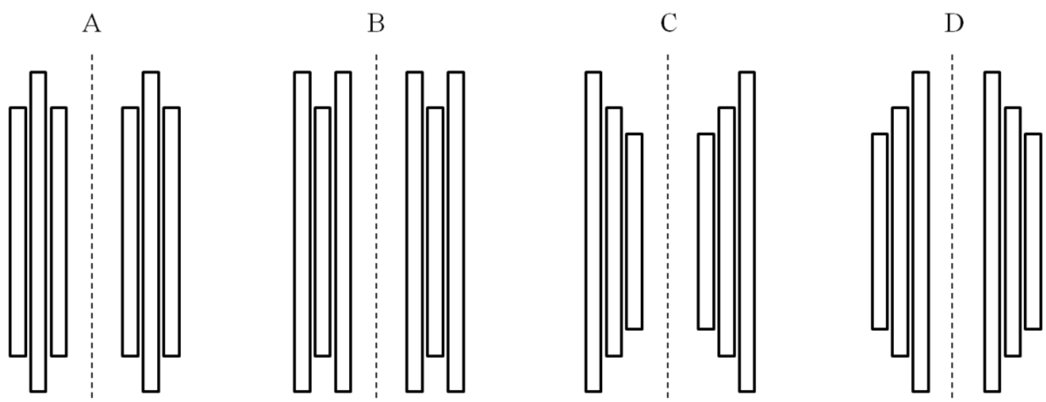

Figure 5.15 Possible cases of staggered layer VPDC solenoids with three layers. The dashed line is the solenoid axis.

These four basic cases where simulated in MATLAB to check the force variation at the ends of the layers. The lengths and the pitch angles for the four cases are summarized in table 5.5. All the other main parameters were kept the same as in table 5.1. The slightly different pitch angles of the four cases were obtained by optimization. This ensures the force reduction in the middle zone of the layers.

Table 5.5 Variation of the layer lengths in a three layer VPDC magnet for the staggered cases shown in figure 5.15. The individually optimized pitch angles are indicated.

Parameter (Unit)	Case A	Case B	Case C	Case D
Length (mm)				
Layer 1	500	600	400	600
Layer 2	600	500	500	500
Layer 3	500	600	600	400
Pitch angle, γ (degrees)				
Layer 1	75.52	75.51	75.61	75.55
Layer 2	48.01	48.03	48.07	48.07
Layer 3	17.64	17.66	17.67	17.53

5.4.1 Force Reduction in Staggered Layers

The main results for the four cases are given in table 5.6. The subscript 'm' in the table indicates the maximum value. For comparison, the original non-staggered case is also included in table 5.6.

Table 5.6 Comparison of the fields and forces of the staggered and non-staggered VPDC magnets with different layer lengths.

Parameter (Unit)	Case A	Case B	Case C	Case D	Not Staggered
B_0 (T)	24.982	24.987	24.926	24.959	25.027
$\|F\|_m$ (N/mm)	258.17	257.84	307.65	310.45	349.38
$\|F_{rad}\|_m$ (N/mm)	50.62	77.58	259.67	263.41	64.42
$F_{ax,m}$ (N/mm)	240.79	240.31	219.18	221.67	326.63
$F_{az,m}$ (N/mm)	172.29	172.33	123.33	130.87	267.55

Figures 5.16 - 20 show the forces of the four different cases for comparison.

Case A

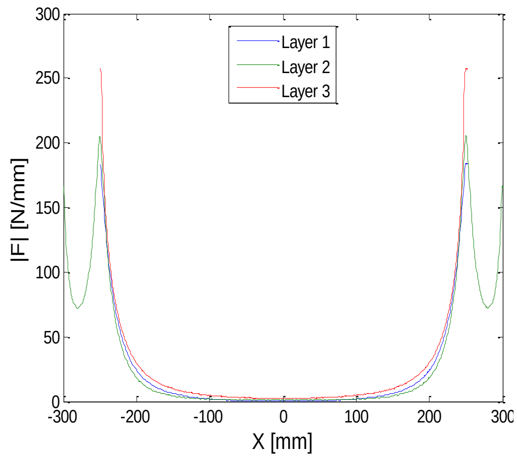

Case B

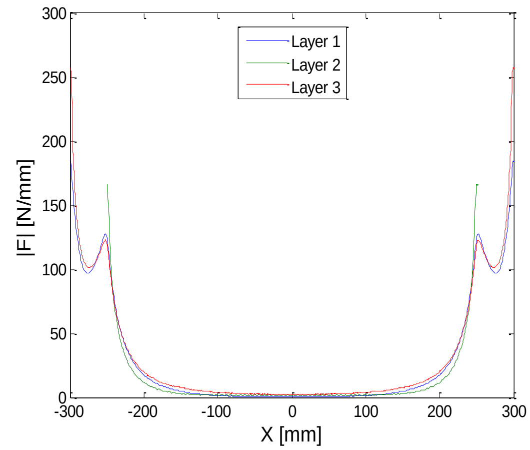

Case C

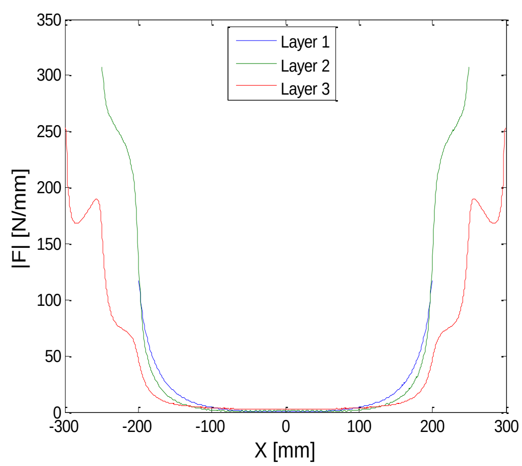

Case D

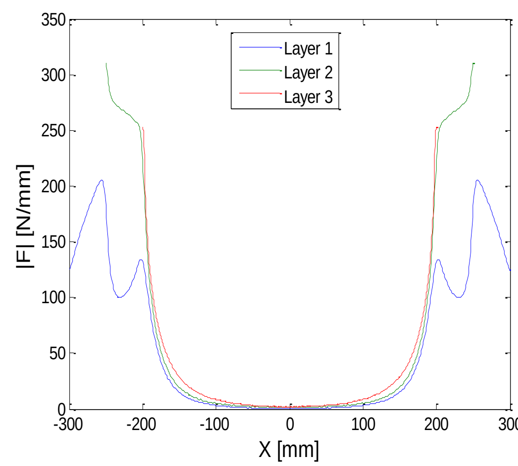

Figure 5.16 Force magnitudes per unit wire length versus axial position of VPDC solenoids with different staggered layers.

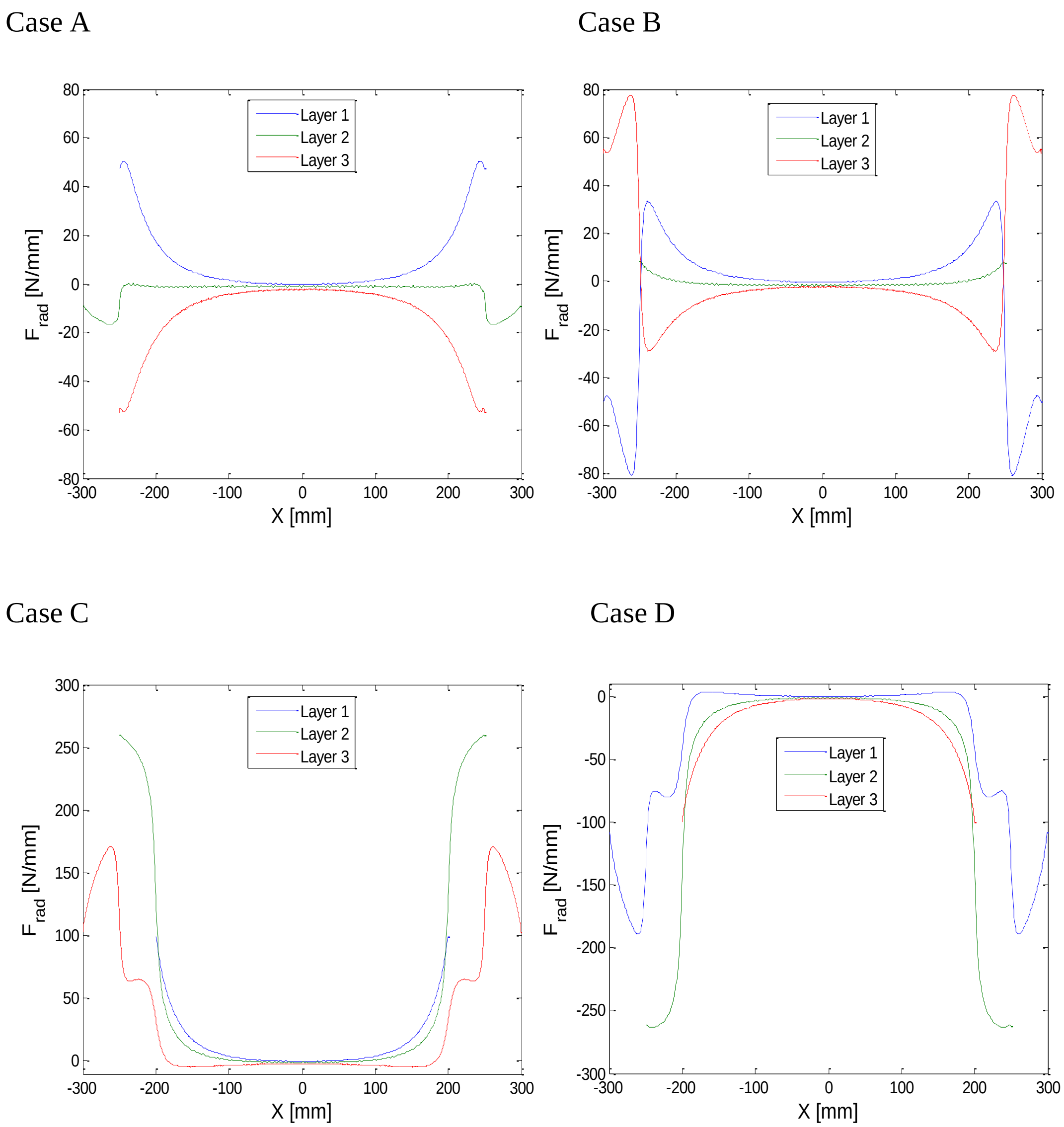

Figure 5.17 Radial force components per unit wire length versus axial position of VPDC solenoids with different staggered layers.

Case A

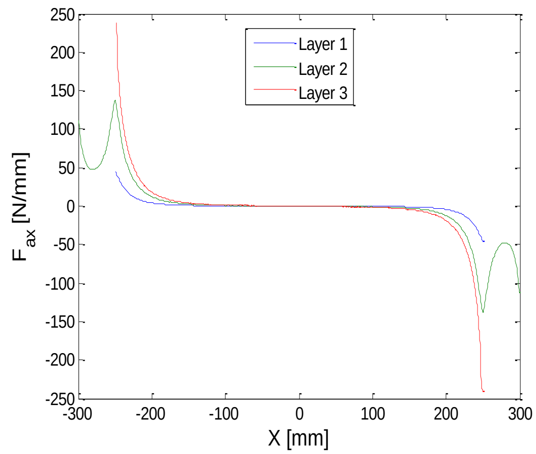

Case B

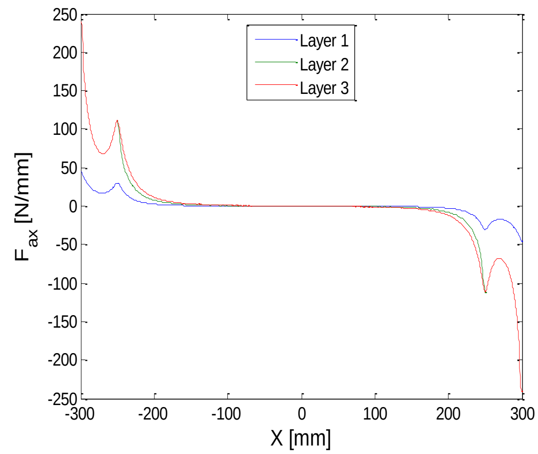

Case C

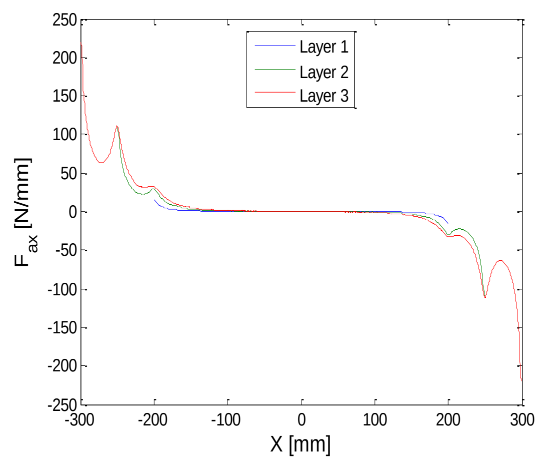

Case D

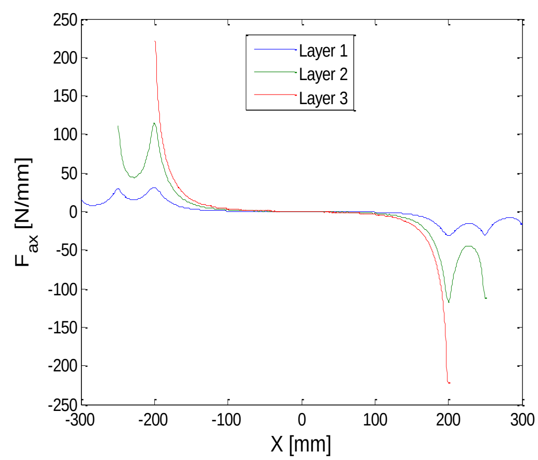

Figure 5.18 Axial force components per unit wire length versus axial position of VPDC solenoids with different staggered layers.

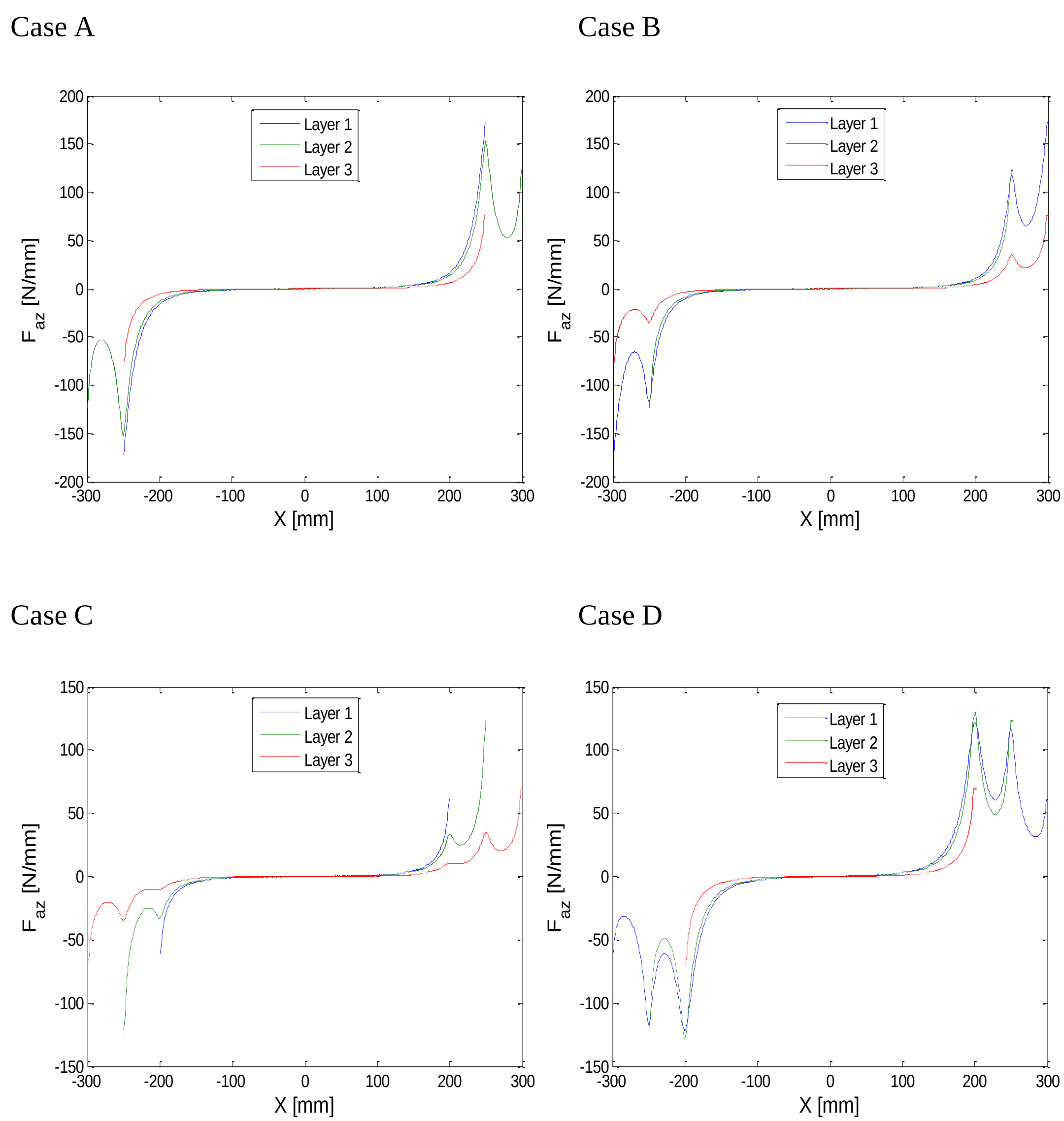

Figure 5.19 Azimuthal force components per unit wire length versus axial position of VPDC solenoids with different staggered layers.

For case A and B the maximum force magnitudes are markedly smaller than in the other cases (see the figures and the table for comparison). There is no significant difference between the peak axial forces for the four cases of the staggered solenoids. But, compared to the non-staggered case, the peak axial force values are much lower in these staggered magnets. The peak azimuthal forces are also smaller when the layers are staggered. However, there is a conspicuous difference in radial forces.

Compensation of radial forces among the layers appears only in case A and B. In the other two cases, there is no radial force compensation (see figure 5.17). In case C, the radial forces are tensile in all layers, while in case D they are compressive. My opinion is that this behavior of radial forces is due to the symmetry of the layers. It can be explained as follows.

In case C, the outermost layer is the longest one where the azimuthal current component dominates (this layer resembles to a regular solenoid). This changes the radial forces to be tensile in the whole magnet. In case D, the longest layer is the innermost layer, where the axial current component dominates. As it was shown in the previous chapter, if the axial current component dominates, the layer experience compressive radial forces. The stronger azimuthal field of the innermost layer changes the radial forces to be compressive in the whole magnet.

On the other hand, in case A and B, only the length of the middle layer was changed. The pitch angle of the second layer is close to 45 degrees, so the magnitude of the axial field (inside) and the azimuthal field (outside) are approximately equal. Hence, modification of the length of the middle layer affects the innermost and the outermost layers approximately in the same way. In these cases (A and B) the field changes approximately symmetrically, so the force-reduction is maintained. This is not true in case C and D, where either the axial field or the azimuthal field starts to dominate, respectively.

This effect excludes case C and D. Since the peak radial force in case A is the smallest, case A would be the better method to reduce the forces not only at the ends but also in the middle zone of the magnet. In the last 50 mm sections at the ends of the middle layer, the radial force does not run up to high values (see figure 5.17: case A, green line), since the pitch angle of this layer is close to the ideal 45 degrees. Because the pitch angle of the second layer is slightly bigger than 45 degrees (48.01 degrees, see table 5.5), there are small, compressive radial forces at the ends of the second layer in case A.

One must note that in these cases, I kept the current magnitude the same in the layers. If the currents are different in the layers, different behavior of the forces can be expected.

5.4.2 The Magnetic Field of Staggered Layers

One must note that, that the center field values are approximately the same (~25T) in all cases (see table 5.6). Furthermore, the on-axis field profiles are better in case A and B than in case C and D (see figure 5.20). It means that the force reduction in middle zone of case A is not due to a lower axial field value in the center, but it is due to the staggered layers and the optimized pitch angles.

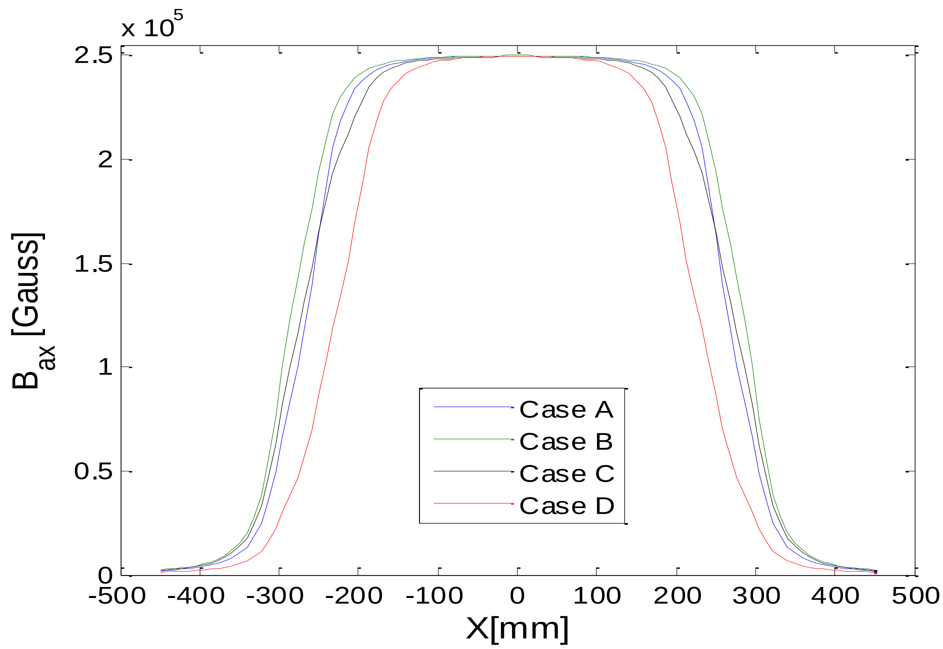

Figure 5.20 On-axis field profile comparison of the different staggered VPDC solenoids.

Since case A seems to be the best choice among the studied staggered cases, in the following I will compare the field at the windings of case A and the non-staggered VPDC solenoid.

The comparisons of the axial and azimuthal field values at the winding are shown on figure 5.21 and 5.22, respectively. These figures show that both the axial and the azimuthal field components are lower at the ends in the staggered VPDC (marked by the dashed lines). These lower field values explain why the peak radial force (per unit length) is also smaller in case A when compared to the non-staggered case (see table 5.6).

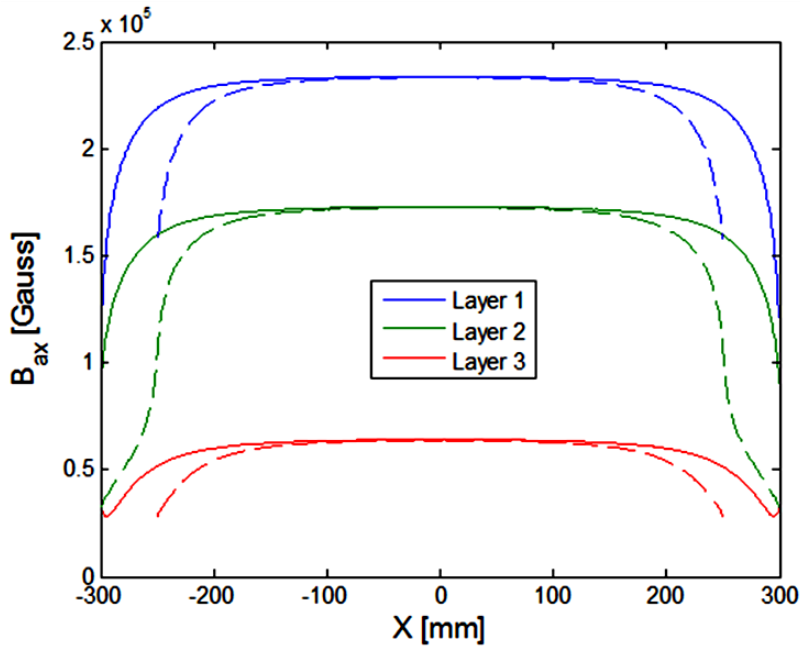

Figure 5.21 Axial field versus axial position on the three layers for non-staggered VPDC (solid lines) and for the staggered VPDC (dashed lines).

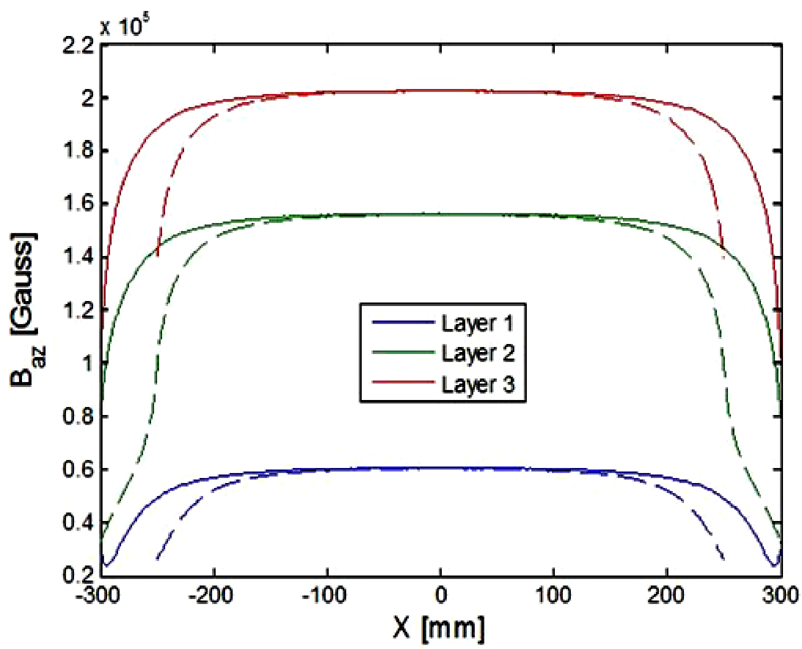

Figure 5.22 Azimuthal field versus axial position on the three layers for non-staggered VPDC (solid lines) and for the staggered VPDC (dashed lines).

The comparison of the radial field values at the winding is shown on figure 5.22. It shows the characteristic change of the radial field at the ends in the staggered case (see the numbered zones).

In zone 1, B_{rad} increases in layer 1 and 2, and their radial fields also increase B_{rad} in layer 2. Since layer 1 and 3 are shorter, their radial field contribution on layer 2 decreases with increasing axial distance (from their ends). As a result of this, the radial field on layer 2 decreases in zone 2.

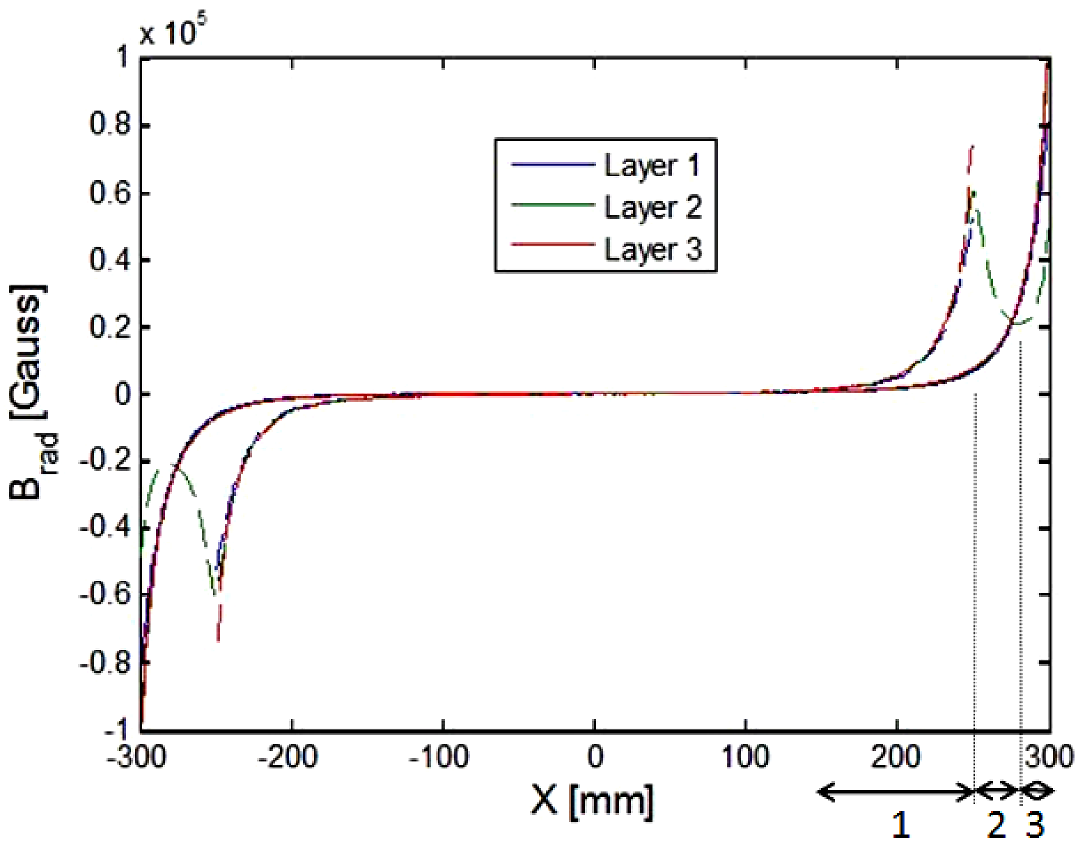

Figure 5.23 Radial field versus axial position on the three layers for non-staggered VPDC (solid lines) and for the staggered VPDC (dashed lines). The numbers at the ends mark different field zones of the staggered solenoid: in zone (1) B_{rad} increases; in zone (2) B_{rad} decreases in the 2^{nd} layer; in zone (3) B_{rad} increases again in the 2^{nd} layer.

The radial field contribution of the second layer to the total radial field at the end is still small in zone 2. However, closer to the end of the magnet, the radial field contribution of layer 2 starts to dominate in zone 3, so here the radial field in layer 2 increases again.

Since layer 2 is the longest, layer 1 is in the longer axial field region of layer 2, so the peak radial field is reduced (in comparison to non-staggered case, see figure 5.23). Layer 3 is in the longer azimuthal field region of layer 2, so the peak radial field is also reduced in layer 3. Due to the lower peak radial field values at the ends, the axial and azimuthal forces are further reduced in case A. The characteristic fluctuation of the radial field at the ends also explains the similar behavior of the axial and azimuthal forces at the ends (see figures 5.18 and 5.19, respectively).

5.5 Heat Analysis and Cooling Design

5.5.1 Heat Analysis and Coil Cooling

The current flowing through a resistive coil will generate ohmic heat due to the resistance of the conductor. In steady state magnets, this heat has to be removed by coolant in order to prevent melting of the conductor material or the insulation. Furthermore, the magnet should operate at temperatures as low as possible, since the mechanical strength of many materials increases with decreasing temperature.

In pulsed magnets, the current is allowed to flow for a short time, and the heat capacity of the magnet is used as a reservoir. To avoid conductor melting, it is important to know the allowed current density during the excitation. The cool-down time of a compact pulsed magnet is typically in the order of half an hour (Herlach and Miura 2003), so the coil heating during the short current pulse can be regarded as being adiabatic.

The initial temperature, the allowed final temperature of the conductor, and the conductor material properties will determine the allowed current pulse characteristic (peak current, pulse width and shape).

The ohmic heating produced during dt time interval causes a temperature rise of dT in the conductor, it can be calculated from the energy balance:

$$\rho(\mathrm{T})\mathrm{j}^2(\mathrm{t})\mathrm{dt} = \mathrm{D}\ \mathrm{c}(\mathrm{T})\mathrm{dT}.$$

Here, $\rho(\mathrm{T})$ and $\mathrm{c}(\mathrm{T})$ describes the temperature dependence of the conductor resistivity and specific heat (at constant pressure), respectively. The D density of the conductor material is assumed to be constant.

5.5.2 Action Integral

If the allowed final temperature (T_f) and the initial temperature (T_i) are known for a given conductor, the maximum allowed current density can be calculated by integration of the energy balance equation. For a current pulse lasting from t_i to t_f :

$$\int_{t_i}^{\mathrm{t_f}} \mathrm{j}^2(\mathrm{t})dt = \int_{T_i}^{T_f} \frac{\mathrm{D}\ \mathrm{c}(\mathrm{T})}{\rho(\mathrm{T})} dT.$$

The time integral of the current density is usually called the action integral (or current integral). The action integral is a unique function of the initial and final temperature for each material, hence the right hand side can be also called as material integral (Kratz and Wyder 2002):

$$F_{mat}\,(\mathrm{T_i}, \mathrm{T_f}) = \int_{T_i}^{T_f} \frac{\mathrm{D\ c(T)}}{\mathrm{\rho(T)}}\, dT.$$

If $\rho(\mathrm{T})$ and $\mathrm{c(T)}$ are known for the conductor material with density D then the material integral can be calculated. The temperature dependence of the resistivity for copper above 60K can be approximated by (Herlach and Miura 2003):

$$\rho_0(\mathrm{T}) = -3.41 \cdot 10^{-9} + 7.2 \cdot 10^{-11}\,\mathrm{T}.$$

The temperature dependence of the specific heat can be approximated by (Herlach and Miura 2003):

$$\mathrm{c(T)} = 834 - 4007(log\mathrm{T}) + 4066(log\mathrm{T})^2 - 1463(log\mathrm{T})^3 + 179.7(log\mathrm{T})^4.$$

Assuming constant density, the material integral can be calculated for different finite temperatures. Calculation of the material integral for copper was performed in MATLAB and it is shown on figure 5.21 for three different initial temperatures.

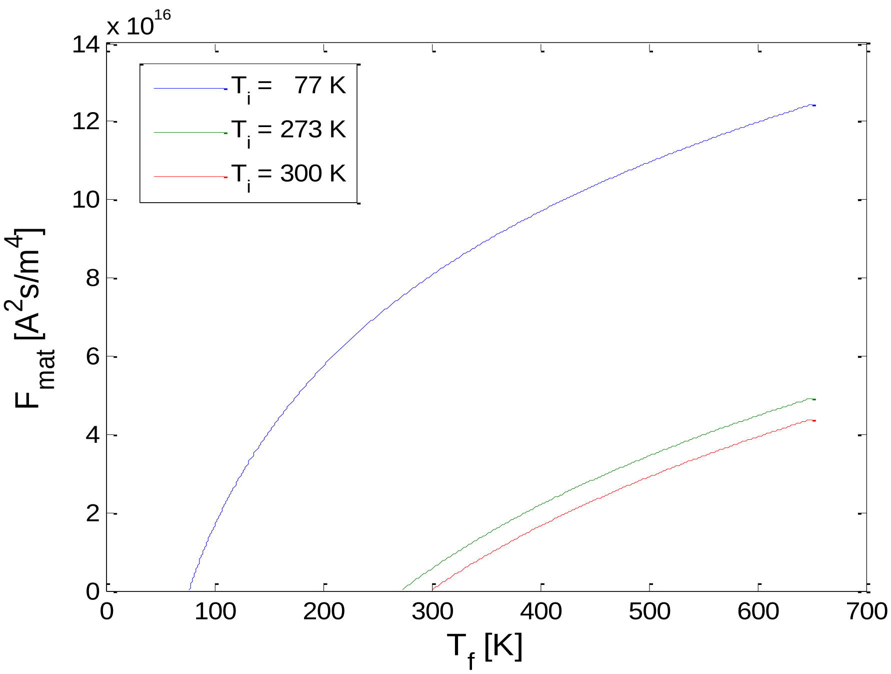

Figure 5.24 Material integral of copper as a function of final temperature for three different initial temperatures.

The action integral can be expressed with the maximum current density j_0 and the τ length of the current pulse as:

$$\int_{t_i}^{t_f} j^2(t)dt = j_0^2\,\tau\,\xi\,,$$

where the ξ parameter reflects the shape of the current pulse. For a rectangular current pulse $\xi = 1$, for a half period of sine wave pulse $\xi = 1/2$, and for a triangular pulse $\xi = 1/3$. Thus, the maximum current density in a conductor can be expressed as:

$$j_0 = \sqrt{\frac{F_{mat}\,(T_i, T_f)}{\tau\,\xi}}.$$

As it can be seen, j_0 in a given conductor depends on the initial and final temperature of the conductor, and it depends also on the shape and length of the current pulse. The maximum current density as a function of finite temperature is shown on figure 5.22 for three different pulse lengths of sine wave pulse. The initial temperature of the conductor was set to 77 K. Figure 5.23 shows the dependence of j_0 on final temperature for three different initial temperatures of the same copper conductor with given pulse width of sine wave pulse.

The maximum allowed temperature of a magnet is determined by the thermal behavior of the insulating material and the annealing temperature of the conductor. For any given pulse shape, pulse width and initial conductor temperature the maximum allowed current density can be calculated.

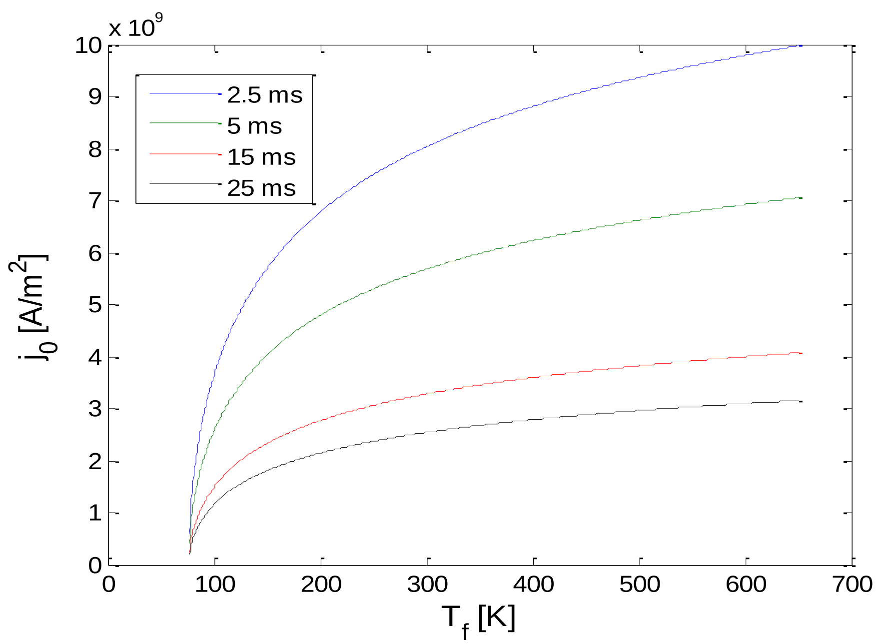

Figure 5.25 Maximum current density of copper as a function of final temperature for three different pulse lengths (sine pulse). The initial temperature is 77 K.

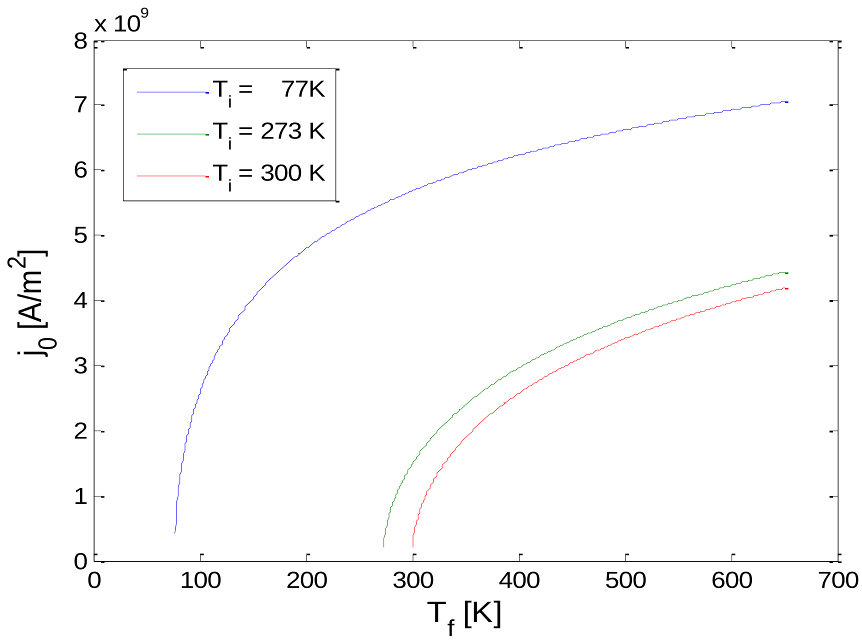

Figure 5.26 Maximum current density of copper as a function of final temperature for three different initial temperatures. The length of the sine pulse is 5 ms.

5.5.3 Effect of Magnetoresistance

The resistance of a conductor increases when exposed to magnetic field, this is called magnetoresistance. Due to the magnetic field the path of the conducting electrons changes, so the length of the electron path increases. This leads to an increased scattering of the electrons which shows up as an increased resistance.

Above 60 K, the transverse field dependence of copper resistivity can be approximated as (Herlach and Miura 2003):

$$\rho(B,T) = \rho_0(\mathrm{T})\left\{1 + 10^{-3}\left(\mathrm{B}\frac{\rho_0(273)}{\rho_0(\mathrm{T})}\right)^{1.1}\right\}.$$

This approximate magnetoresistance function is based on experimental data, and was confirmed up into the megagauss range (Fowler, et al. 1994) . The resistivity of copper as a function of temperature for four different field values is shown on figure 5.24. The magnetoresistance increase strongly with magnetic field and its influence becomes important around 50T (Herlach and Miura 2003). Since the resistivity depends on the magnetic field, it modifies the material integral of the conductor, and hence the maximum allowable current density in the conductor. Figure 5.25 shows the maximum current density as a function of final temperature for three different field values.

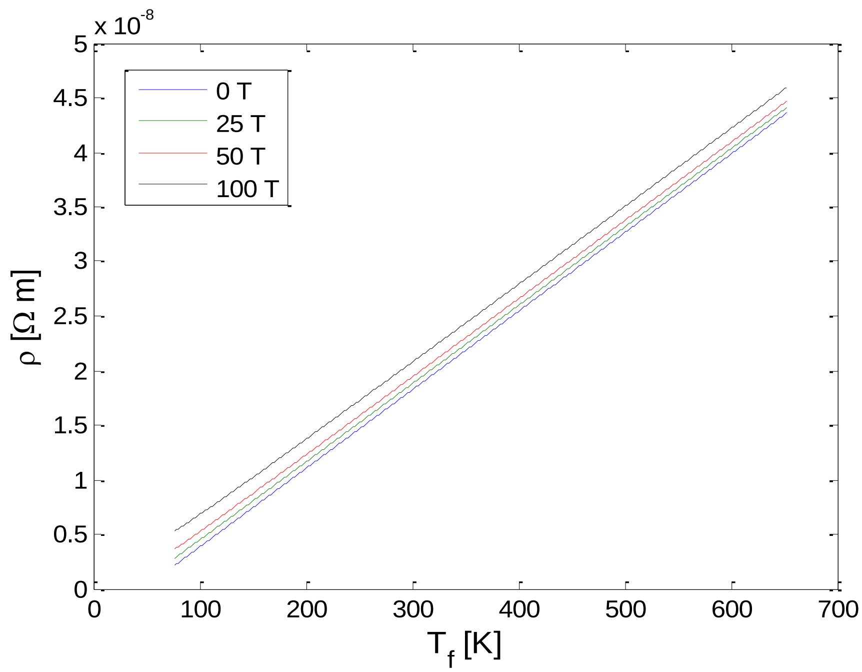

Figure 5.27 Resistivity of copper as a function of final temperature at four different field values.

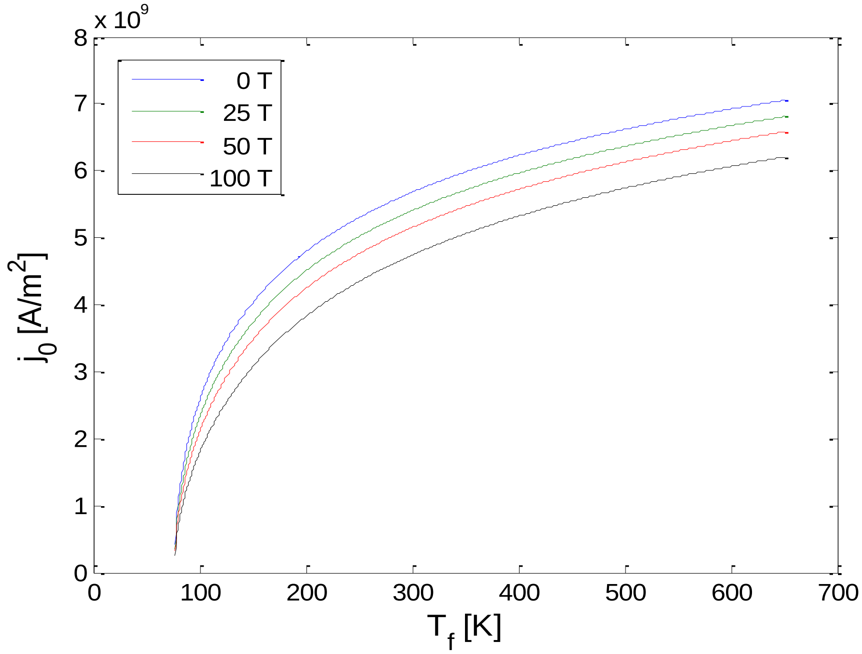

Figure 5.28 Maximum current density of copper as a function of final temperature at four different field values. The initial temperature is 77 K and length of the sine pulse is 5 ms.

Magnetoresistance depends not only on the conductor material, but also on the orientation of wire (current) relative to the magnetic field. One can discern transverse and longitudinal magnetoresistance. The longitudinal magnetoresistance is generally smaller (Kratz 2002). Thus, one can expect smaller magnetoresistance in force-reduced windings where the current and the field tend to be parallel in the winding.

For the 25-T force-reduced magnet, the highest current density ($5.9 \cdot 10^9$ A/m^2) is in the first layer (see table 5.1). From figure 5.25 the final temperature of the copper conductor can be estimated. For a 5 ms sine pulse the final temperature of the conductor would be around 350 K if the conductor is pre-cooled to liquid nitrogen temperature. This final temperature is well below the melting point of copper (see appendix on conductor properties).

5.5.4 Considerations on Conductor Materials and Cooling

The material integral (hence the allowable current) of the conductor increases if the magnet is cooled down before the current pulse. To reach high fields with longer pulse durations one should choose a conductor with material integral as big as possible. Usually, copper or aluminum is selected as a conductor material for winding. Compared to aluminum, the material integral of copper is generally larger. If the initial temperature is 77 K (liquid nitrogen temperature) and the allowed final temperature is 400K, then the material integral for copper is approximately two times larger than for aluminum.

It was also shown that the material integral and the current density increase with lower initial temperature of the conductor. It is possible to pump on the nitrogen, to achieve 63 K (this method is applied in Toulouse). Another possibility is liquid neon (LNe), to reach 27 K. However, Ne is very expensive and pool boiling use of LNe is not economical, so application of a closed cycle system is better (this was used in Amsterdam). At liquid He temperatures (~ 4K), the specific heat capacities are so low that the consumption of He would be expensive. Designs are possible that use He more economically and reduction in temperature significantly below 77 K would just about allow to reach even 100 T with existing materials (Jones, et al. 2004).

The material integral is also bigger for high purity conductors, due to their lower resistivity. According to Matthiessen's rule, the total resistivity of a solid conductor is the sum of two resistivity components: *a.* the temperature dependent resistivity due to the thermal vibrations of the ions in the lattice (phonons), and *b.* the temperature independent resistivity due to the interactions of the conduction electrons with the irregularities of the lattice (impurities, defects, crystal boundaries). This latter resistivity part is called the residual resistivity (or intrinsic resistivity). Generally, compared to alloys, the total resistivity of higher purity conductors is smaller (due to the lower residual resistivity). The improved resistivity of high purity metals is more conspicuous at low temperatures (~ 4 K of liquid helium) where the contribution of the thermal lattice vibration to the total resistivity is smaller.

At liquid helium temperatures, high purity aluminum has some advantages over copper. The residual resistance of aluminum is about the same as copper. The high field magnetoresistance is much lower than that of copper. Furthermore, aluminum is more readily obtained in high purity (99.999% pure) than copper. Since Al has lower density, the mass of the winding would be also lower compared to similar Cu windings. However, high purity aluminum is extremely soft material, and force reduction on the winding is important.

As it was mentioned before, the other advantage of cooling is that the strength of most common materials increases with decreasing temperature. The yield strength of Al and Cu at different temperatures is given in the appendix. The increase in strength is a result of the reduced thermal excitations within the lattice, which inhibits the spread of dislocations (Van Sciver 1986).

As a summary, at liquid helium temperature one has to consider the application of high purity aluminum as a possible winding material. If the magnet is pre-cooled to liquid nitrogen temperature where the effects of purity are smaller, copper seems to be the better choice for conductor material. A summary of relevant parameters of the conductors are also given in the appendix.

Chapter 6

Discussion of the Results

6.1 Force-Reduced Solenoid Coil

In force-reduced solenoids, axial current component must be introduced evenly in a given layer. This makes these solenoids different from regular solenoids, where the current is mainly azimuthal. To introduce the axial currents evenly, tilted wires (with certain pitch angle) can be distributed along the surface of the solenoid. The pitch angle of the wires depends on the number of layers, on the geometry of the layers and on the current in the layers.

The ideal pitch angle of the layer(s) can be determined, using filamentary approximation. Minimization of the angle between the current elements and the field vectors gives the optimal pitch angle of the wires in the layer(s). If there is only one layer, the ideal pitch angle of the wires is 45 degrees. The pitch angle obtained from the simulation is in good agreement with this result considering the discrete characteristics of the conductors. If the solenoid consists more layers, then the innermost layer has the highest pitch angle (axial current is higher) and the outer layers have smaller and smaller pitch angles (azimuthal current is higher).

Since each layer contains many parallel wires, this results in a very complex winding configuration, which is a major drawback of the previous force-reduced solenoid concepts. A high field magnet would require even 10 - 20 layers or more, therefore manufacturing a high field force-reduced magnet would be tedious. This problem can be eliminated with the VPDC solenoid, where the tilted current paths are machined directly in a conducting tube. With this method more conductor layers can be nested easily, and higher fields can be achieved with force-reduction in the magnet. The direct conductor method also allows easier staggering of the layers in order to further reduce the forces at the ends.

In force-reduced superconducting solenoids, one has to ensure equal current sharing between the parallel superconducting wires in a given layer. In parallel connection of superconductors (with zero resistance), there is the problem that the current in the superconductors is not equal. The currents will not necessarily be introduced uniformly into the helical conductor paths of a layer, since the distribution of the currents is influenced by the mutual inductance of each current path. If the inductances of the current paths (including the lead-in wires) are all identical, then it is possible to distribute the currents uniformly into the helical conductors (Sass and Stoll 1963).

Since superconductors are capable to carry higher current densities, application of superconducting helices would also facilitate DC operation of force-reduced solenoids. This offers a possible promising application of force-reduced superconducting magnets. A superconducting magnetic energy storage system (SMES) stores energy in the magnetic field produced by a (persistent) direct current flowing in the superconducting coil. Force-reduced superconducting magnets are capable to carry larger currents and to hold large energy content. The magnetic energy in the coil increases with the square of the current, so the advantage of light weight, force-reduced superconducting magnet as magnetic energy storage device is obvious. A low weight SMES system would be important not only for space and military applications, but also for power grid stabilization.

6.2 Force-Free Magnetic Field

As it was shown in the introduction of the force-free fields, in cylindrical systems two main field components must exist: the axial field (also called as poloidal field) and the azimuthal field (also called as toroidal field). These field components can be generated with tilted wires of variable pitch angles. The axial field dominates inside the force-reduced solenoid, while the azimuthal field dominates in the outer parts of the solenoid.

Since significant azimuthal field is also generated by the currents in a force-reduced solenoid, the transfer function of these coils are lower than in a regular solenoids. Thus, to generate the desired axial field in the bore of a force-reduced coil, more currents are needed than in a regular solenoid.

Besides the obtained field in the bore, the field in the winding structure is also important when the acting forces are considered. In case of a monolayer winding, the simulation showed that the azimuthal field (B_{az}) on the winding does not change significantly with the pitch angle. The azimuthal field remains basically the same on the winding. The formula obtained from Ampere's law could not predict this behavior of the azimuthal field (see eqn. 4.1). In the analysis of monolayer coils, I explained the reason of this contradiction. To reduce forces in monolayer coils, the simulation showed that the axial field and the azimuthal field must be equal on the winding. This result is also in good agreement with theory.

In multilayer force-reduced solenoids, however, the axial and azimuthal fields are not equal on the layers in general. This behavior was also explained by considering the forces on the winding and the simulation results confirm the argument.

The magnetic field content of the coil region is higher in multilayer force-reduced magnets compared to conventional coils (Furth, Levine and Waniek 1957). This was also proven by the simulation (see figure 5.4). In conventional solenoid winding the magnetic field falls off relative to the peak field in the bore. It means that in a conventional solenoid the coil represents a region of low magnetic energy density compared to the bore region. It results a pressure gradient in the magnet that the coil and additional support structure must counteract. In a force-reduced solenoid coil, though the axial field also falls down, the azimuthal field increases in the coil with radius (figure 5.4). It puts additional magnetic energy into the coil region. This additional magnetic energy is used to hold the coil against stress (or, in other words, against the bore field pressure). This also explains the weaker efficiency of central field generation (i.e. the low transfer function) in force-reduced solenoids. It means that force-reduced solenoids are not really power efficient, and increased capacitor bank is expected.

The results of the simulation on solenoid end-effects showed if the lengths of the layers are changed symmetrically, then the force-free character of the field is maintained in the magnet (assuming equal currents in the conductors). In addition to the symmetry studies on solenoid cross-section shape by Van Bladel, this end-effect study also confirms the importance of winding structure symmetry in force-reduced solenoids. The simulations also showed that proper staggering of the layers does not change significantly the on-axis field profile and the maximum field in the center. The peak field values at the ends can be further reduced with application of staggered layers (see figures 5.21-23). In case A, the peak radial fields at the ends were reduced by ~3T, ~5T, ~3T in layer 1, 2 and 3 respectively (see figure 5.23).

If the return currents are also considered, further shaping of the field lines at the ends are possible by inserting diamagnetic walls near the ends of the solenoid (Shneerson et al. 2004). In this way, the force on the additional curved wires at the ends can be reduced.

6.3 Force Reduction

In accordance with the theory of force-free magnetic fields, reduction of forces was obtained by reducing the angle between the current element vectors and the field vectors on the wire element.

In the middle zone of the layer(s), the forces are reduced and balanced. In conventional solenoids the main issue is to support the increased radial forces in a long section of the magnet along its length. Either in monolayer or multilayer force-reduced solenoids, the radial forces are greatly reduced in a large portion of the magnet length.

According to the theory, a finite size winding configuration cannot be completely force-free. This was also confirmed by the simulations. Due to the finite length and the stray field, the forces rise up at the ends of a force-reduced solenoid.

In comparison with the regular solenoid, the peak radial forces at the ends were still lower and compensated in the VPDC magnet. Note that the κ angles at the ends increase, so these lower radial force values at the ends are also due to the decreasing axial and azimuthal field values on the winding end-sections (it is clear that the force on a wire with fixed current can be also reduced by reducing the field on the wire).

The azimuthal forces increased more at the ends of a force-reduced solenoid due to the interaction of the radial field and the axial currents. However, both the azimuthal and the axial forces at the ends can be further reduced in the VPDC magnet by changing the length of the helices (with optimal pitch angle) relative to each other. Properly staggered layers can significantly lower the magnitude of all force components at the ends while the magnet maintains approximately the same field value in the center. The reduction of axial and azimuthal forces at the ends is mainly due to the reduced radial field component at the ends (see figure 5.23). The reduction of radial forces at the ends is mainly due to the reduced axial and azimuthal field components at the ends (see figures 5.21 and 5.22). Compared to the conventional solenoid example, in case A of the staggered VPDC magnet the peak radial force was reduced by approximately 92 % and the peak axial force was reduced by approximately 14 % (see tables 5.4 and 5.6). Compared to the non-staggered case, the peak azimuthal force was reduced by approximately 35% in case A.

It must be pointed out, that the increased forces at the ends of the VPDC act on smaller range of the total length (approximately in the last 50 mm sections). It means that the forces need to be supported on a smaller range (compared to a regular solenoid). Consequently, the mass of the support structure would be smaller in a force-reduced solenoid than in a conventional solenoid, so the cost and the overall size of the magnet would be reduced.

Chapter 7

Summary and Conclusions

7.1 Conclusions

The main obstacle of high magnetic field generation is the handling of the large Lorentz forces in the magnets. A possible way of force reduction in electromagnets is based on the theory of force-free magnetic fields. A detailed investigation of the relevant properties of force-free magnetic fields was presented. Previous studies on force-reduced magnets were also summarized in order to identify the possible methods of force reduction and the major design issues.

Force-reduced solenoid winding configuration can be obtained by properly setting the pitch angle of the conductors. A new code was developed to find the optimal pitch angle in solenoids with different number of layers.

The simulation of the winding structure was based on filamentary approximation. This approach differs from the commonly applied finite element methods. It allows faster computation of magnetic fields and Lorentz forces for more complex winding configurations. A novel approach was used to determine the optimal pitch angle of the filamentary wires on solenoids with different number of layers. Based on force-free condition, an optimization routine minimizes the angle between the wire element vector and the induction vector on the winding by varying the pitch angle of the conductors.

For monolayer solenoids, the simulation results showed the limited applicability of Ampere’s law. The analysis of a monolayer force-reduced coil also revealed that the transfer function of force-reduced coils is smaller compared to regular solenoids. Consequently, multilayer force-reduced solenoids are necessary with high current densities to generate higher magnetic field fields.

Due to the many parallel wires in more layers, a high field force-reduced magnet would have an extremely complex winding configuration. As a solution to this problem, a novel design method was proposed, the variable pitch direct conductor (VPDC) magnet. In direct conductor method, the winding pattern is machined directly from conducting cylinder(s).This method facilitates the application of more layers and it allows higher current densities in the conductor material. The method also allows wider choice of conductor parameters (for example to set the conductor cross-section area).

Due to the required high current, pulsed operation of the magnet is preferred. A heat analysis was also performed to determine the maximum allowed current in the conductor during the pulse assuming pre-cooled winding.

A conceptual design of a 25-T solenoid with three layers was provided. The optimal pitch angles were determined. Detailed magnetic field and force analysis were performed on the force-reduced winding. The simulated magnetic field distribution of the force-reduced solenoid is in good agreement with the force-free magnetic field theory. In a force-reduced solenoid, the main field components are the axial field (dominating in the bore) and the azimuthal field (dominating at the outer layers). The magnetic field on the winding was also determined. It was shown, that the peak field values in the middle zone of the layers behave according to the force-free condition.

The simulation confirmed that the forces in a finite size coil configuration cannot be everywhere zero. It was shown, that significant force-reduction can be achieved in the middle zone of a VPDC magnet. Due to the stray magnetic field, the forces increase at the ends in force-reduced solenoids. It was shown, that the high force region at the ends is smaller compared to the extent of the high force region in a conventional solenoid. It was also shown, that the expected maximum radial forces at the ends of the VPDC are smaller in magnitude than the peak radial forces in a conventional solenoid. The azimuthal forces at the ends of a force-reduced solenoid were not studied before in the literature. It was pointed out that higher azimuthal forces are expected at the ends of force-reduced solenoids.

The behavior of staggered layers in multilayer force-reduced solenoids was not investigated before. In this work, an end-effect study on forces was performed for three-layer staggered configurations. This study showed that further, significant force reduction is possible at the ends with properly staggered layers while the on-axis field does not change significantly in the magnet. The end-force reduction is mainly due to the reduced field magnitude at the winding. The pitch angles of the staggered layers were also adjusted, so the force-reduction in the middle zone of the staggered layers was maintained.

7.2 Results and Contributions of This Work

In this section, I provide a list of main results and new contributions of my work :

- A novel magnet concept was developed, which for the first time enables realistic manufacturing of force reduced coils. The coil windings are not made from conventional wire conductors, but the current carrying components are machined out of conductive cylinders. Manufacturing difficulties of existing designs are therefore completely eliminated.
- The performed analysis was based on newly developed codes that were checked against analytical calculations of simple coil configurations. The numerical method is based on filamentary approximation of the conductor that allows fast calculations and enables complete optimization of 3D coil configurations.
- The simulation confirmed predictions of the theory (for example: the main field components in cylindrical force-free systems are the axial and azimuthal fields; finite size coils cannot be completely force-free; the ideal pitch angle in monolayer force-reduced solenoid is 45 degree; force-free fields usually do not obey superposition principle).
- The ideal pitch angle in force-reduced layer(s) was obtained by optimization that is based on the force-free field theory.
- Force-reduction in the middle zone of the layer(s) was obtained by reducing the κ angle (the angle between the current element vector and its field vector).
- The simulation showed a significant increase of azimuthal forces at the ends of the layer(s) in a force-reduced solenoid, when compared to regular solenoid, where azimuthal forces are extremely small.

- A significant force-reduction has been be obtained in the force-reduced windings at the ends of the layers by properly staggered layers of helical windings with variable pitch angles, thereby reducing the magnitude of the field at the winding.

7.3 Future Work

The simulation revealed not only the advantages but also the disadvantages of force-reduced solenoids. Further improvements are possible. To increase somewhat the power efficiency, different currents can be applied in the layers. An optimal current distribution can be determined for example with a more sophisticated optimization routine. However one must keep in mind that energy is needed anyhow to maintain the force-reduction in the coil, so my opinion is that significant improvement in power consumption cannot be expected.

For time reasons, toroids were not analysed in this work. However, the code is already able to simulate bent solenoids and toroids with different cross section shape using filamentary approximation. Figure 7.1 shows a sample of a bent 2-layer solenoid, where the cross-section of the second layer is an ellipse of 1.5 eccentricity.

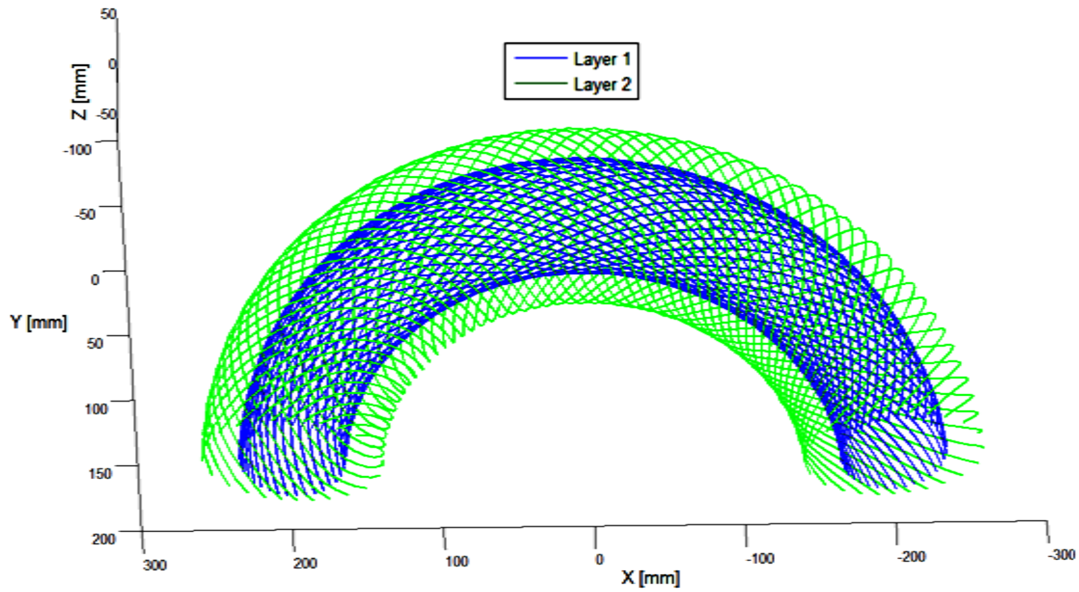

Figure 7.1 Sample plot of a 2-layer bent solenoid. In this sample, the pitch angle of the wires is 70 degrees in the 1st layer and 45 degrees in the 2nd layer. The second layer has elliptical cross-section shape of 1.5 eccentricity.

Effects of additional iron would be also worthwhile to study as a possible method for field shaping at the ends of the solenoid (this can be done by finite element analysis for example). Furthermore, a small scale VPDC magnet can be manufactured to gain more information on the operational behavior of force-reduced solenoids. A preliminary test plan is given in the appendix. On the long term, it would be advantageous to test also the application of superconductors in force-reduced solenoid winding schemes.

Appendix A

Maxwell's Equations

The development of the force-free magnetic field equations is based on the Maxwell's equations (Knoepfel 2000, Jackson 1999). In differential form they are:

$$\nabla \cdot \mathbf{E} = \frac{\rho}{\varepsilon} \tag{A.1}$$

$$\nabla \cdot \mathbf{B} = 0 \tag{A.2}$$

$$\nabla \times \mathbf{E} = -\frac{\partial \mathbf{B}}{\partial t} \tag{A.3}$$

$$\nabla \times \mathbf{B} = \mu \cdot \mathbf{j} + \mu \cdot \varepsilon \frac{\partial \mathbf{E}}{\partial t} \tag{A.4}$$

where **E** is the electric field strength [V/m]; **B** is the magnetic induction [T]; **j** is current density [A/m^2]; ε and μ are the electric permittivity and the magnetic permeability, respectively. The electric permittivity and the magnetic permeability of the media can be expressed as $\varepsilon = \varepsilon_0\, \varepsilon_r$ and $\mu = \mu_0\, \mu_r$ (respectively), where ε_0 and μ_0 are the permittivity and permeability of vacuum while ε_r and μ_r are the relative permittivity and relative permeability of the material, respectively.

To obtain a general solution, three more equations are required, that is, Ohm's law and the constitutive equations:

$$\mathbf{j} = \sigma\, \mathbf{E}, \tag{A.5}$$

$$\mathbf{B} = \mu\, \mathbf{H}, \tag{A.6}$$

$$\mathbf{D} = \varepsilon\, \mathbf{E}, \tag{A.7}$$

Where $\mathbf{D}$ is the electric induction (or –displacement, also called displacement current) [C/m^2]; $\mathbf{H}$ is the magnetic field strength [A/m]; σ is the electric conductivity [1/(Ωm)].

The electric and magnetic fields $\mathbf{E}$ and $\mathbf{B}$ in the Maxwell's equations were originally introduced by means of the force equation:

$$\mathbf{F} = q(\mathbf{E} + \mathbf{v} \times \mathbf{B}) \tag{A.8}$$

This force is the Lorentz force, the force acting on a particle with an electric charge q moving with velocity $\mathbf{v}$ in an electric field $\mathbf{E}$ and in a magnetic field (described by its magnetic induction vector $\mathbf{B}$). This expression of the Lorentz force is also valid for time-dependent quantities and for any velocity (Knoepfel 2000).

Appendix B

Comparison of Conductor Material Properties

Some relevant parameters of aluminum and copper are summarized here.

Table B.1 Selected parameters of aluminum and copper.

Parameters	Dimension	Aluminum	Copper
Density[a] (at 25 ^{o}C)	g/cm^3	2.7	8.96
Resistivity[a] at 300 K	10^{-8} Ωm	2.733	1.725
80 K		0.245	0.215
1 K		0.0001	0.002
Melting Point[a]	^{o}C	660.32	1084.62
Specific Heat[b], c_p at 300 K	J/(g K)	0.902	0.386
77 K		0.336	0.192
4 K		0.00026	0.00009
Yield Strength[c], σ_y at 300 K	MPa	282	552
80 K		332	690
0 K		345	752
Material Integral[d] (T_i = 77K, T_f = 400 K)	10^{16} A^{2}s/m^4	4.58	9.42

[a] Data is given for pure metals (Lide 1994).
[b] Ekin (2006).
[c] Data is given for Al 6061 and Cu+2Be, respectively (Van Sciver 1986) .
[d] Kratz et al. (2002).

Appendix C

Validation of Field Calculations

The method of finding force-reduced configurations is based on the field calculations. To check and confirm the field calculations, a simulation was performed independently using the commercially available AMPERES software for a 3-layer force-reduced configuration (Goodzeit 2008) .The parameters of the 3-layer test solenoid is given in table C.1below:

Table C.1 Parameters of a 3-layer force-reduced solenoid for validation of field calculations.

Parameter (unit)	Layer 1	Layer 2	Layer 3
Center radius, R_c (mm)	23.81	30.16	36.51
Length (mm)	400	400	400
Pitch angle, γ (degrees)	77.47	56.23	23.58
Number of conductor strips per layer, w	24	24	24
Current per conductor strip, I (A)	1000	1000	1000

The simulated wire filaments obtained from AMPERES is shown on figure C.1:

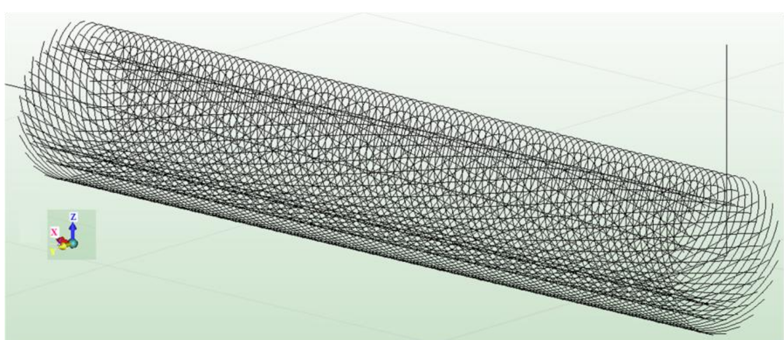

Figure C.1 Simulated conductor filaments obtained from AMPERES for field calculations (Goodzeit 2008).

The values of the field components (B_x, B_y, B_z) obtained from AMPERES for the midplane of this test solenoid is shown in figure C.2. The field values from AMPERES are marked with '+' signs. The solid lines show the field values obtained from the MATLAB simulation. As it can be seen, the field values obtained from the simulations are in good agreement. This also validates the field calculations.

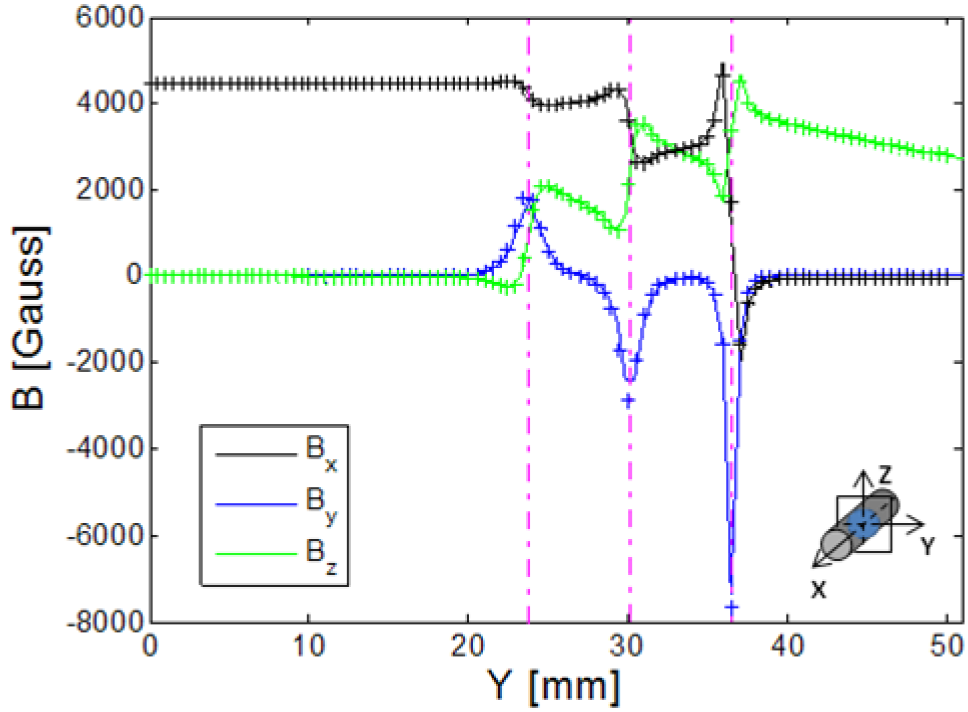

Figure C.2 Comparison of the field component values obtained from AMPERES and from the MATLAB simulation for the midplane of the test solenoid. The field values from AMPERES are marked with '+' signs, the solid lines represent the field values obtained from MATLAB. The field values of the simulations are in good agreement. The radii of the layers are marked with the magenta lines.

The on-axis axial field profile for this magnet was also calculated using the analytical formula of eq.4.3. The theoretical axial field values along the axis (obtained from eq.4.3) were compared to the simulation values obtained from the MATLAB code. The percent difference between the theoretical values and the simulation values was also calculated at each position along the axis. Figure C.3 shows the axial field values together with the calculated percent difference values along the axis. As it can be seen, the values obtained from the two methods are in good agreement, the percent difference values are really low (especially towards the center).

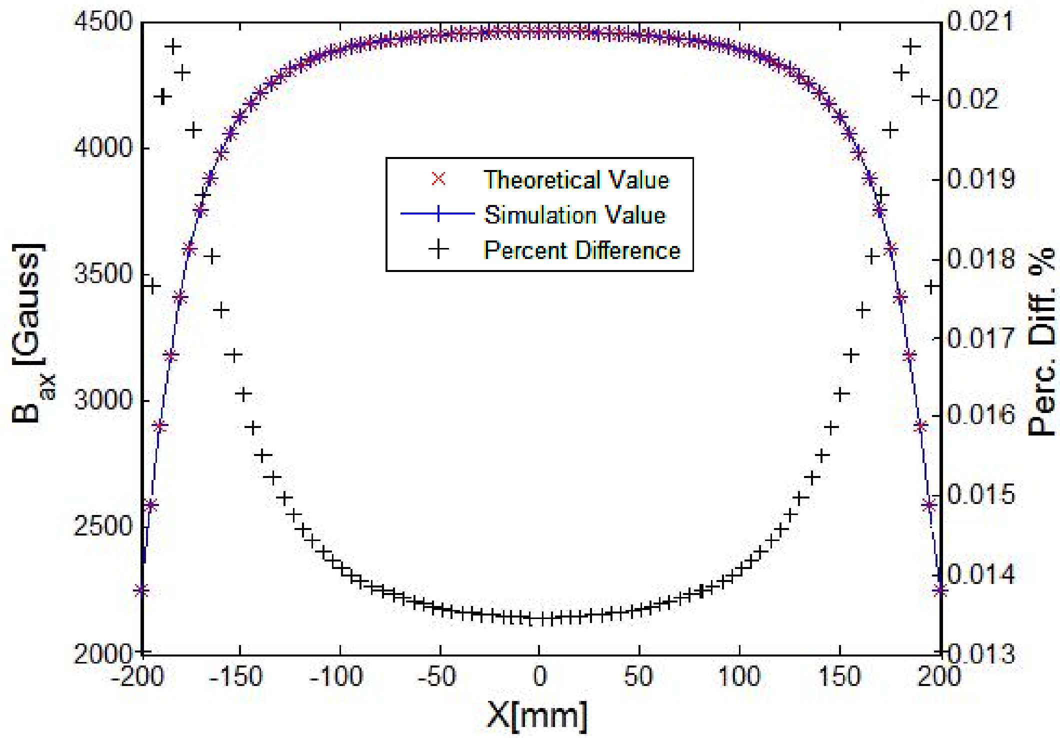

Figure C.3Comparison of the axial field values (along the solenoid axis) obtained from the analytical calculations (red 'x') and from the MATLAB simulation (blue '+'). The percent difference vales (black '+') are also shown at each position. The low percent difference values indicate that the values obtained from the simulation are in good agreement with the theory.

Appendix D

Preliminary Test Plan

In this section, I provide a brief plan to test the properties of a small scale 3-layer VPDC force-reduced model solenoid. If required (depending on the parameters of the future test magnet and the maximum currents in the magnet) proper cooling must be used. Here, I assume distilled water flow cooling. To reduce cost and facilitate the measurements, it is further assumed that the measurements are performed at low DC currents of about 100 A. Precise results taken at low currents can be extrapolated to estimate the magnet performance at high currents in pulsed mode.

<u>Planned Measurements:</u>

- Field measurements (to test field distribution of the magnet);
- Strain measurements (to check force reduction);
- Resistance and temperature measurements (to test heating of the magnet).

<u>Required Equipment:</u>

- Assembled 3-layer VPDC magnet;
- DC power supplies for the 3 layers;
- Water chiller for distilled water and flow meter;
- Ampere- and voltmeters;
- Thermocouples (for temperature measurements);
- Hall-probe (for field measurements);

- Strain gauges and readout device for strain measurements (at least 3 gauges per layer: 2 at the ends and 1 at the middle of the layers).

Measurements:

Field measurements:

- Measure on-axis field profile and peak field in the bore: use Hall-probe to measure field values at different positions along the axis at a given current when only the inner layer is powered. Repeat measurements with different current values.
- Repeat measurements for the other two layers, and calculate the transfer function of each layer.
- Measure on-axis field profile and peak field in the bore: use Hall-probe to measure field values at different positions along the axis when all layers are powered together. Repeat the measurements when the three layers are powered with different current. Verify also the field direction in the bore using Hall-probe.
- Measure field outside the magnet at different positions increasing the distance from the magnet (along the radial direction). Test also field direction with Hall-probe.

Strain measurements:

These strain measurements should be repeated for strains due to hoop stress, axial stress and azimuthal stress (torsion).

- Measure strain values at the ends and in the middle of the innermost layer when only that layer is powered. Repeat the measurement also for the other two layers separately.
- Measure strain values when all layers are powered together and test force-reduction (the strain from hoop stress should be significantly smaller in the middle zone of each layer when compared to the previous case). Compare results of the corresponding layer to the previous case, when only one layer was powered.
- Repeat the previous measurement at different set of currents.
- Test how the degree of force-reduction changes when the current in one layer is changed to a different value (while maintaining the currents in the other two layers). In absolute value higher strain values are expected in this latter case.
- If possible repeat these measurements with staggered layer configuration.

Resistance and temperature measurements:

- Monitor temperature values at different positions on each layer to test heating of the layers. Repeat these measurements when different current is applied.
- Measure the resistance of the conductor layers to test the temperature dependence of the resistance in each layer.

The proposed tests would give a good understanding of the magnet performance and allow verifying my performed simulations. The obtained results would help to optimize the design of a larger, full size magnet.

Appendix E

Stress and Strain in Nb_3Sn Superconductor

Stress and strain can degrade the superconductive properties and the mechanical strength of the composite wire in a superconducting magnet. Consequently, it is important to know in magnet design how the critical current density of superconductor depends on the values of magnetic field, temperature and strain ($j_c(B, T, \varepsilon)$).

A superconductor wire is usually subject to three different kinds of stress in a magnet:

Fabrication stress:

During magnet construction, the superconducting wire is subjected both to bending stress as it is wound into the magnet coil and to uniaxial stress from the pretension of the wire during the winding procedure.

Thermal-contraction stress:

Superconducting wires are usually composite wires: they consist of twisted multifilamentary superconductors embedded in a matrix of normal conducting material (usually copper). As the wire is cooled down to cryogenic temperature, the different materials within the composite wire contract at different rates. Because of the mismatch of the thermal contraction rates, significant stress on the superconducting material can be generated during cooldown.

Magnetic stress:

In high field superconducting magnets the Lorentz forces put the conductor under considerable stress. As the magnet is energized, the stress due to the Lorentz-force can approach the ultimate strength of conventional multifilamentary superconductors, 1GPa or more.

Effects of Strain on Critical Parameters

As it was mentioned before, in the wire the superconductor is embedded by reaction in a matrix material (normal conducting material). As the wire is cooled down below 20 K, the larger thermal contraction of the matrix material (compared to the thermal contraction of the Nb_3Sn) results in an axial pre-compression of superconductor. This pre-compression is characterized by the axial pre-strain ($\varepsilon_i < 0$). The combined strain from the other sources of winding stress (fabrication stress, magnetic stress) is the applied strain (ε_a). In the total strain (ε_0) the axial pre-strain is added to the applied strain:

$$\varepsilon_0 = \varepsilon_i + \varepsilon_a .$$

Present high field superconducting magnet designs favor the use of Nb_3Sn as winding material. It can be assumed that the main effect of strain is the modification of the electron-phonon interaction in the Nb_3Sn crystal lattice (Oh and Kim 2006 and Markiewicz 2004). The dependence of the critical current density is determined by the de-pinning of the flux-line lattice in the superconductor. The bulk pinning force depends on the applied field, temperature and strain on the superconductor, since these parameters can change the electron-phonon interaction in the lattice.

Most models for strain dependence are defined through the strain dependence of the upper critical field or the critical temperature. The first model, proposed by Ekin, was a completely empirical model. It is the so-called power law model (Ekin 1980). This model is only valid over a limited strain regime and does not account for the three-dimensional nature of the strain in the wire (Godeke, et al. 2006). Different types of other models were proposed to better describe the strain behavior of Nb_3Sn. One of these models is a modified version of the so-called deviatoric strain model (Godeke, et al. 2006). This model is in good agreement with the observed strain behavior of Nb_3Sn, it accounts for the three-dimensionality and it can be also applied at larger strain values where the strain dependence is approximately linear.

A MATLAB code was written based on these model calculations of Godeke et al. (Godeke 2005, see also Lee 2006) to simulate the strain dependence of the critical parameters of Nb_3Sn superconductor. The code and the input parameters of the simulation can be found in appendix F. The critical current density as a function of temperature and field at different strain values is shown in figures E.1 and E.2, respectively. Figure E.3 shows the critical current density as a function of strain at a given field (10 T) and temperature (4.2 K). One can also define the normalized critical current density j_c / j_{cm}, where j_{cm} is the maximum critical current density at zero strain. The normalized critical current density as a function of strain at different field values is shown in figure E.4.

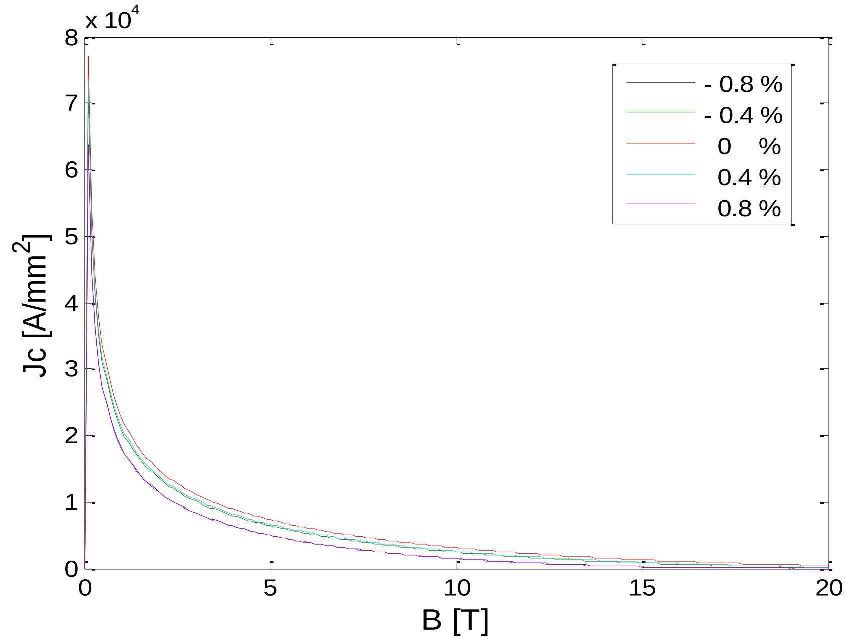

Figure E.1 Critical current density of Nb_3Sn as a function of magnetic field at 4.2 K for different strain values.

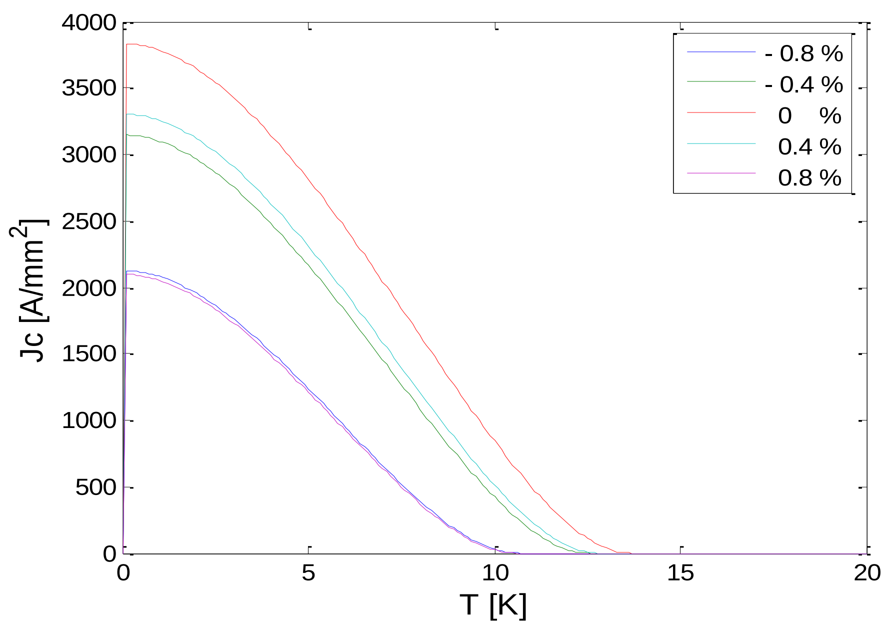

Figure E.2 Critical current density of Nb_3Sn as a function of temperature at 10 T for different strain values.

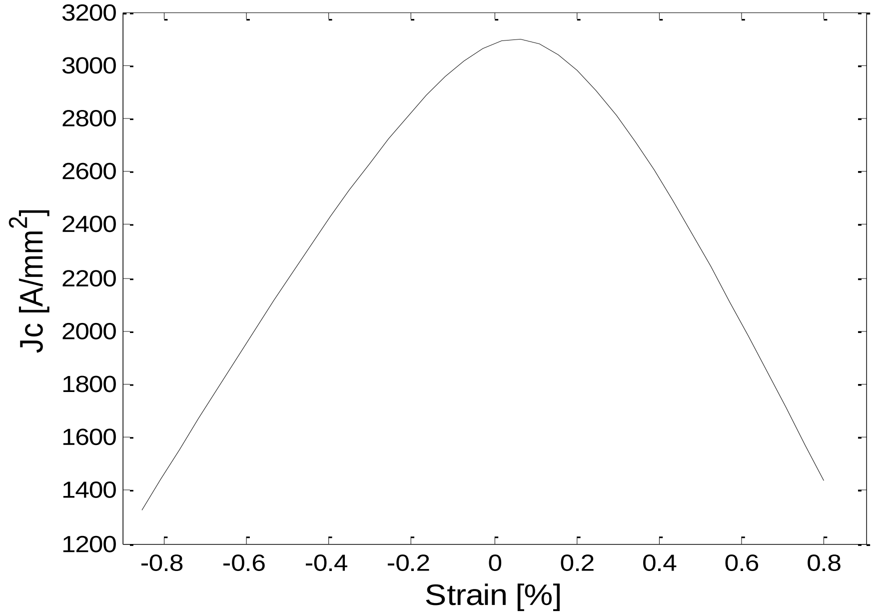

Figure E.3 Critical current density of Nb_3Sn as a function of strain at 4.2 K and 10 T.

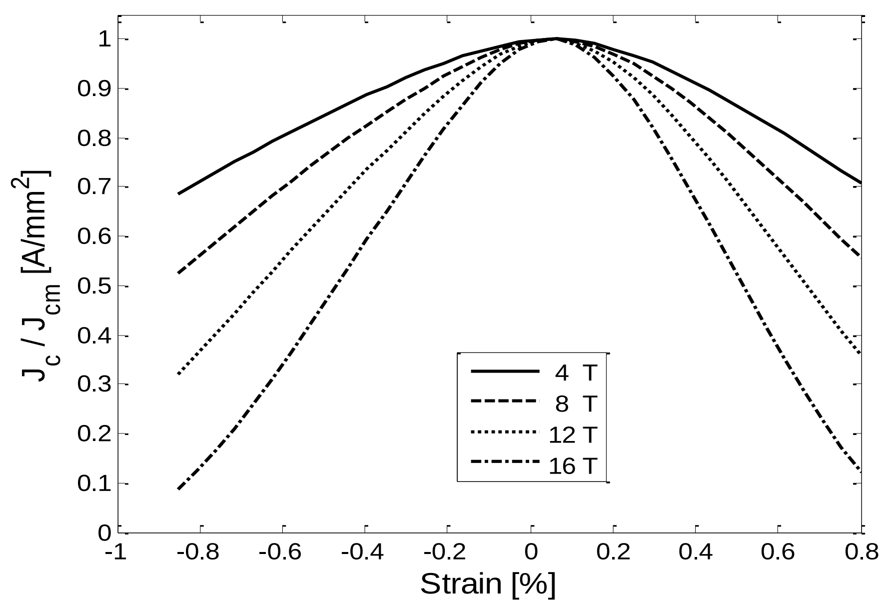

Figure E.4 The normalized critical current density of Nb_3Sn as a function of strain at different field values and at 4.2 K.

When the Nb_3Sn composite wire is subjected to compressive strain (ε_a, $\varepsilon_0 < 0$), the critical parameters (J_c, B_{c2}, T_c) reduce approximately linearly with strain. When the wire is subject to tension ($\varepsilon_a > 0$), the tensile strain counteracts the initial compressive strain, and the total strain (ε_0) becomes less negative. Thus, J_c increases approximately proportionally with strain until a parabolic-like peak is reached (see figure E.3). The maximum appears where the strain on the wire is minimal. After the maximum, the critical properties reduce approximately linearly again with increasing tensile strain on the wire (Godeke, et al. 2006).

A strain design criterion can be employed to utilize the strain dependence of critical current density in magnet design. The strain design criterion states that the combined strain from all sources of wire stress in the superconducting winding should be approximately equal and opposite to the initial compressive prestrain of the wire, so the total strain is approximately zero: $\varepsilon_0 = \varepsilon_i + \varepsilon_a \approx 0$.

This strain balance need only be obtained in the critical parts of a magnet, where the field is highest in the winding (Ekin, Superconductors 1983). For strains below approximately half percent, the critical current density changes quite reversibly, i.e. after removal of the stress the original J_c is recovered. At higher strains however, the superconducting filaments suffer permanent damage by microcracking. As it is shown on figure E.4, at 16 T the maximum critical current density reduces by about 30% at 0.4% strain. At higher fields the maximum current density reduces more. Therefore, it is desirable to design magnets so the strains are kept below about 0.3 percent (Wilson 1983).

As a result of the strain the critical surface of the Nb_3Sn superconductor shrinks, so it narrows the operational range of the superconducting magnet. Figure E.5 shows how the critical surface is modified when strain is applied on the conductor.

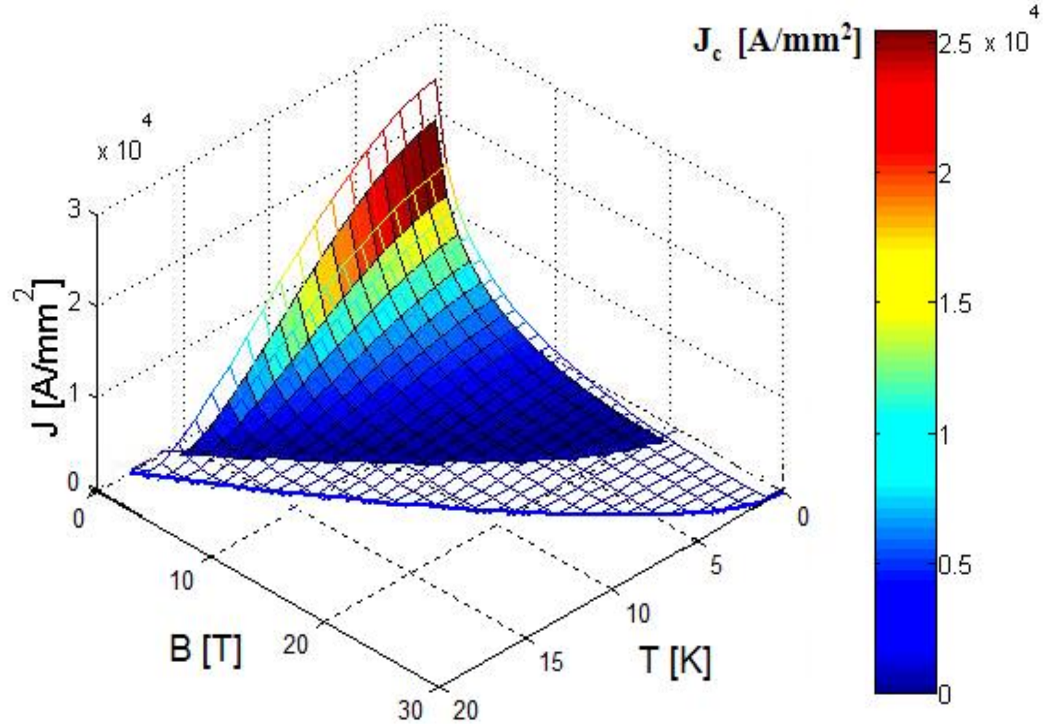

Figure E.5 Simulated critical surface of Nb_3Sn superconductor at 0 % strain (outer, transparent surface) and at 0.8 % strain (inner surface).

Appendix F

Computer Programs

In this section the main calculation routines and their input/output parameters are presented. Programming of the simulation was performed in MATLAB (version 7.0.4 with service pack 2).

Codes of VPDC magnet calculations:

```
clc; clear; disp('Wait!')

% Give input parameters of the VPDC:
VPD.SolNum  = 3; %number of layers in the magnet
VPD.Rmag    = [26.5,30.5,34.5]; %magnet layer center radius [mm]
VPD.Lmag    = [600,600,600]; % layer length in mm (positive)
VPD.Wirenum = [49,44,21]; %number of wires/layer
VPD.Pitchang = [75.4713,47.9914,17.6581]; %pitch angle is measured from the
vertical
VPD.Thet    = [0,0,0];%initial phase angle [deg] of the 1st wire on the layer
VPD.Rot     = [0,0,0];%rotates the solenoid layer [deg]
VPD.Coeff   = [-0.5,-0.5,-0.5]; % set -0.5 to center magnet to 0 on X axis
VPD.XShift  = [0,0,0]; %shift layer along the X axis [mm]
VPD.YShift  = [0,0,0]; %shift layer along the Y axis [mm]
VPD.ZShift  = [0,0,0]; %shift layer along the Z axis [mm]
VPD.Exc     = [1,1,1]; %cross section eccentricity
VPD.NPoints = [100,100,100]; %number of wire elements on the twisted filament
VPD.ITrans  = [34100,34100,34100]; %transport current in one wire (positive, [A])
VPD.IDir    = [1,1,1]; % current direction (+/- 1, same sign=same direction)
VPD.WireDiameter=[2.1,2.3,2.3]; %wire diameter [mm]
VPD.TH      = [3,3,3]; % layer thickness [mm], for circular set it equal to wire
diameter
%% Set WL wire element length if number of points (VPD.NPoints)
%% has to be adjusted automatically (else set it 0):
VPD.WL = 1; % wire element length [mm]

%%=========================================================
% Feasibility calculations:
FEAS = GenerateFeasibilityPar(VPD); % returns a structure of feasibility par.
```

```
VPD = GenerateInputCheck(VPD,FEAS); % check input and returns warnings if
exist
%%===============================================================
% Generate helical points coordinates X,Y,Z [mm]:
[X,Y,Z,NTot] = GenerateVPDCEllipse(VPD); %NTot is the total number of points
%%===============================================================
%Generate wire element vectors:
[PT2,PT1,LVEC,SC,RSC,PhiSC,ArcSC,starting,ending,stp,etp,TNwe,Mwelength,N
WE]...
    = GenerateVPDCEllipsewireel(VPD,X,Y,Z);
%%===============================================================
% Heat analysis calculations
% Input parameters for temperature and field dependence:
CDens =8960; %conductor mass density in kg/m^3
PulseWidth=5 *1e-3; % pulse length [s]
Xi=1/2; %pulse shape factor; xi=1 for rectangular; 1/2 for sine; 1/3 for triang.
Tempini=77; %initital temperature [K]
Tempfin=650; %final temperature [K]
delTemp=0.5; %temperature increments [K]
Fielddep=1; %field dependence 1-yes,0-no (w/o magnetoresistance)
Bini=25; %field value [T]
TempRange=Tempini:delTemp:Tempfin; %temperature range [K]

% Calculate resistivity, specific heat, material integral:
[rhonull,rho,spech,FMatint]=GenMaterialIntegral(Tempini,Tempfin,delTemp,Bini,C
Dens,Fielddep);
% Calculate current density limits:
jlim=GenCurrDensLimit(FMatint,PulseWidth,Xi); % [A/m^2]
Jlimmax=max(jlim); % maximum current density [A/m^2]
TempRange=Tempini:delTemp:Tempfin; % Assign temperature values for plots
%%===============================================================
%Analytical field calculations
%Field calculation from Ampere's law [Gauss]:
[AmpereBin,AmpereBout]=GenAmpereFieldCalc(VPD,VPD.Rmag(1)/1000);
%Field calculation from Biot-Savart law [Gauss]:
[BiotCalcBax,BiotCalcBaxL]=GenBiotAxFieldCalc(VPD,FEAS);
% Transfer function calculation (T/A):
[TrFunction,TrFunctionTot]=GenerateTransFunc(BiotCalcBaxL,VPD);
% Center field pressure [Pa]:
PrBzero=GenerateBcentPress(BiotCalcBax);
%%===============================================================
% Field calculation from the filaments
% Set calculation range:
xax = 1; % along x axis only
yax = 0; % along y axis only
zax = 0; % along z axis only
% set extension range for plotting (multiplier of the magnet size):
```

```
exten = [1.5,1.5,1.5];
% Set number of testpoints:
txmax = 100; %number of testpoints along x axis
tymax =17; %number of testpoints along y axis
tzmax = 17; %number of testpoints along z axis

% Calculate field from the filaments [Gauss]
% BFbore contains: Bx,By,Bz,Brad,Baz components and the field magnitude:
[BFbore,BFMagbore,BinCenter,BinCenterMagni,PT]=...

GenerateBinBore(VPD,X,Y,Z,starting,ending,Mwelength,exten,txmax,tymax,tzmax
,xax,yax,zax);
%%===========================================================
% Magnetic field calculations on winding
% BFwinding gives Bx,By,Bz,Brad,Baz field components [Gauss]
% CurrBangle is the angle between wire element vector and the field vector [deg]:
[BFwinding,BFMagwind,CurrBangle] =
GenerateBonWinding(TNwe,SC,LVEC,Mwelength,starting,ending,X,Y,Z,VPD);
% Find peak field values and their position on each layer:
PB = PeakField(BFwinding,BFMagwind,VPD,NWE);
% Check radial force balance:
[BazSinPitchang,BaxCosPitchang] = CalcRadForceBalance(VPD,PB);
%%===========================================================
% Lorentz force calculations
% Calculate Fx,Fy,Fz,Frad,Faz,F magnitude [N/mm]
[FL,FLRad,FLAz,FLMag,FLRadyproj,FLRadzproj,mFLRad,mFLAz,mFLAx,mFLMa
g]=...
GenerateForce(VPD,PT1,PT2,X,Y,Z,PhiSC,TNwe,stp,etp,Mwelength,starting,endi
ng);
% Find peak force values [N/mm] and their position on each layer:
PF = PeakForce(FL,FLRad,FLAz,FLMag,VPD,NWE);
%%===========================================================
% Generate plots:
IFig = 1; % start to assign figure numbers
IFig = GeneratePlots_Winding(VPD,X,Y,Z,SC,PT1,PT2,LVEC,IFig);
IFig = GeneratePlots_FieldInBore(PT,BFbore,BFMagbore,IFig);
IFig =
GeneratePlots_FieldOnWinding(VPD,NWE,SC,ArcSC,BFwinding,CurrBangle,IFig)
;
IFig = GeneratePlots_Heat(TempRange,rho,rhonull,spech,jlim,FMatint,IFig);
IFig =
GeneratePlots_Force(VPD,NWE,SC,ArcSC,FL,FLRad,FLAz,FLMag,FLRadyproj,F
LRadzproj,IFig);
%%===========================================================
% Optimization
% Set parameters to optimize:
Par =VPD.Pitchang(1:VPD.SolNum);
```

```
% Set optimization parameters:
options = optimset('Diagnostics','on','Display','iter','TolFun',1e-
6,'MaxIter',1000000,'MaxFunEvals',1000000,'TolX',1e-6);

% Find optimal parameters and the minimum value:
[OptPara,Minfval] = fminsearch(@(Par) OptVPDCEllipseM(Par,VPD),Par,options)

disp 'Done!';beep
```

Codes of Nb_3Sn critical parameters generation and strain dependence

(see also Godeke 2006 and Lee 2006)

```
% Calculations and plots for Nb3Sn critical surface and the strain
% dependence of its critical parameters.
% Calculations are based on work of Arno Godeke (2006), see reference.

clc;clear;disp('Wait!');

% Give properties:
% Note: All strains are divided by 100 (percent values)!!!
MP.Ca1   = 43;  % deviatoric 2nd strain invariant
MP.Ca2   = 4.3; % deviatoric 3rd strain invariant
MP.eRem  = 0.247/100; %hydrostratic strain, 1st strain invarinant
MP.eMax  =-0.054/100; %thermal axial pre-strain
MP.Bc2m0 = 30; % maximum upper critical field in T (at 0K and at min.strain)
MP.Tcm0  = 18; % critical temperature in K (at minimum strain and 0 T)
MP.C     = 150000; % constant for Jc calc. [AT/mm^2]
MP.n = 1;   % from Ekin formula (power values)
MP.p = 0.5; % constant for pinning force dependence on field
MP.q = 2;   % constant for pinning force dependence on field
MP.v = 2;   % const. for pinning force dependence on Bc2 [T]
MP.g = 1;   % const. for pinning force dependence on kappa [T]
MP.w = 3;   % const. for field dependence on temp.
MP.u = 2;   % const. for field dependence
IFig = 1; % start to number figures

% Sample calc. of crit parameters:
Bapplied = 10; % field value [T]
Tapplied = 4.2; % temperature [K]
e_applied = 0; % strain [%]
[CritB,CritJ,CritT] = BcJcTcCalculator(Bapplied,Tapplied,e_applied,MP);
%%=========================================================
```

```
% Generate temperature dependence plots:
Tlim=20; % upper limit of temperature [K]
ic=0; %start index counting
for Temp=0:0.1:Tlim % temperature range [K]
   ic=ic+1; %increase index
   Temper(1,ic)=Temp; % temperature values
   [Bc2,Bc20,Tc0,S] = calc_Bc2(Temp,e_applied,MP); % Calculate 2nd crit.field
   BcTemp(1,ic)=Bc2;   % Bc2 vs. temperature
   TcvsB(1,ic)=Tc(Bc2,e_applied,MP); % critical temp. vs. crit. field
   JcTemp(1,ic)=Jc(Bapplied,Temp,e_applied,MP);   % Jc vs. temperature
end
IFig=PlotBcVsTemper(Temper,BcTemp,IFig); % plot Bc vs. temperature
IFig=PlotJcVsTemper(Temper,JcTemp,Bapplied,IFig); % plot Jc vs. temperature
%%============================================================
%Generate the field dependence plot of Jc:
fc=0;
Blim=20; % upper limit of field [T]
for fie=0:0.1:Blim % values for field and temperature
   fc=fc+1;
   Bfieldv(1,fc)=fie; % field values
   JcField(1,fc)=Jc(fie,Tapplied, e_applied, MP);% Jc vs. field
end
IFig=PlotJcVsField(Bfieldv,JcField,Tapplied,IFig); % plot
%%============================================================
%Generate strain dependence plots:
LowerStrain= -0.8/100; % lower strain limit [%]
UpperStrain= 0.8/100 - MP.eMax; % upper strain limit [%]
eapp=linspace(LowerStrain,UpperStrain,37); % applied strains
etot=eapp + MP.eMax; %total strain (all terms are divided by 100)
is=0; % start counting for strain values
for strain=1:length(etot) % strain testpoints
   is=is+1;
   JcStrain(1,is)= Jc(Bapplied,Tapplied,etot(is), MP); % Jc vs. strain
   TcStrain(1,is)=Tc(Bapplied,etot(is), MP); %Tc vs.strain
   BcStrain(1,is)=Bc(Tapplied,etot(is), MP);  %Bc2 vs. strain
end
StrainValues=etot*100; %place strain values in a vector,for plots
IFig=PlotJcVsStrain(StrainValues,JcStrain,IFig); % generate plots
IFig=PlotBcVsStrain(StrainValues,BcStrain,IFig);
IFig=PlotTcVsStrain(StrainValues,TcStrain,IFig);
%%============================================================
% Generate critical surface:
e_applied=[0.8/100,0];
for eee=1:2
   IFig=GenerateCritSurf(30,18,IFig,MP,e_applied(eee)); % plot critical surface
end
disp('Done!');beep
```

References

Amm, B C. *An Optimized Superconducting Toroidal Magnet Using Force-Reduced Winding Scheme.* Tallahassee, 1996.

Anderson, P. W., and Y. B. Kim. *Rev. Mod.Phys.*, no. 36 (1964): 39.

Aubert, G. "High Magnetic Fields: Physical Limits in Magnet Design." *Physica Scripta* T35. (1991): 168-171.

Bergeron, C. J. "Simple Model for Longitudinal Force-Free Current Flow in Superconductors of the Second Kind." *Applied Physics Letters*, 1963: 63-65.

Berlincourt, T. G. "High Magnetic Fields by Means of Superconductors." *Brit. J. Appl. Phys.* 14 (1963): 749-758.

Bitter, F. *Rev.Sci.Instrum.* 7 (1936): 482.

Boom, R. W., and J. C. Laurence. "Force-Reduced Superconducting Toroidal Magnet Coils." *NASA Technical Memorandum*, 1970.

Bouillard, J.X. "Preliminary Investigation of Force-Reduced Superconducting Magnet Configurations for Advanced Technology Applications." Argonne National Laboratory, 1992.

Brandt, E. H. "The Flux Line Lattice In Superconductors." *Rep. Prog. Phys.*, no. 58 (1995): 1465-1594.

Brownstein, K. R. "On Solutions of the Equation $\nabla \times a = ka$." *J. Phys. A: Math. Gen.*, 1987:L19.

Buck, G.J. "Force-Free Magnetic Field Solution in Toroidal Coordinates." *J.Appl.Phys.* 36, no. 7 (1965): 2231-2235.

Callaghan, E. E. "Anisotropic effects in Helically Wound Superconducting Solenoids." *NASA Technical Note*, 1963.

Chandrasekhar, S. *Hydrodynamic and Hydromagnetic Stability.* London: Oxford University Press, 1961.

Clem, J. R. *Phys. Rev. Lett.*, no. 38 (1977): 1425.

Cullen, G. W., G. D. Cody, and J. P. McEvoy. "Field and Angular Dependence of Critical Currents in Nb3Sn." *Physical Review* 132, no. 2 (1963): 577-580.

Ekin, J. W. *Experimental Techniques for Low-Temperature Measurements.* Oxford: Oxford University Press, 2006.

Ekin, J. W. "Superconductors." In *Materials at Low Temperatures*, by R. P. Reed and A. F. Clark, 465-513. Metals Park: American Society For Metals, 1983.

Ekin, J. W. "Strain scaling law for flux pinning in practical superconductors: Part I – Basic Relationship and Application to Nb3Sn conductors." *Cryogenics*, 1980: 611-624.

Fowler, C. M., B. L. Freeman, J. C. King, and D. T. Torres. *Megagauss Magnetic Field Generation and Pulsed Power Applications.* Edited by M. Cowan and R. B. Spielman. Commack, N.Y.: Nova Science Publishers Inc., 1994.

Friedlander, F. J. In *Encyclopedia of Physics*, by R. G. Lerner and G. L. Trigg, 288. VCH Publishers, 1991.

Furth, H.P, M.A. Levine, and R.W. Waniek. "Production and Use of High Transient Magnetic Fields.II." *Rev.Scientific Instruments*, 1957: 949-959.

Furth, H.P., and M.A. Levine. "Force-Free Coils and Superconductors." *J. Appl. Phys.* 33 (1962): 747-748.

Furth, H.P., S.C. Jardin, and D.B. Montgomery. "Force-Free Coil Principles Applied to High-Temperature Superconducting Materials." *IEEE Trans.on Magnetics* 24, no. 2 (1988): 1467-1468.

Gao, B. J., H. J. Schneider-Muntau, Y. M. Eyssa, and M. D. Bird. "A New Concept in Bitter Disk Design." *IEEE Transactions on Magnetics*, 1996: 2503-2506.

Georgievsky, A.V., V.E. Ziser, and Yu.A. Litvinenko. "Employment of Partly Force-Free Toroidal Magnetic Systems for Producing Stellarator-Type Traps." *Proceedings of the 5th Symposium on Engineering Problems of Fusion Research*, 1974: 511-514.

Godeke, A., B. ten Haken, H. H.J. ten Kate, and D. C. Larbalestier. "A General Scaling Relation for the Critical Current Density in Nb3Sn." *Supercond.Sci.Technol.*, 2006: 100-116.

Godeke, A. *Performance Boundaries in* Nb_3Sn *Superconductors.* Ph.D. Dissertation, University of Twente, Enschede, 2005.

Goodzeit, C. L. Private communications, 2008.

Hand, G. L., and M. A. Levine. "New Approach to Force-Free Magnetic Fields." *Physical Review* 127, no. 6 (1962): 1856-1857.

Hansen, W.W. "A New Type of Expansion In Radiation Problems." *Phys.Rev.* 47 (1935): 139-143.

Herlach, F., and N. Miura. *High Magnetic Fields - Science and Technology.* Vol. I. Singapore: World Scientific Publishing Co. Pte. Ltd., 2003.

Hill, J. L., B. C. Amm, and J. Schwartz. "A Comparison of Force-Reduced Toroidal Geometries and Conventional Superconducting Magnets." *Advances in Cryogenic Engineering* 39 (1994): 285.

Hill, J.L., B.C. Amm, and J. Schwartz. "An Analysis of Force-Reduced Toroidal Magnets." *IEEE Transactions on Magnetics* 30, no. 4 (1994): 2094-2097.

Iwasa, Y., and J. Minervini. *MIT OpenCourseWare, Superconducting Magnets.* 2003. http://www.core.org.cn/OcwWeb/Nuclear-Engineering/22-68JSpring2003/CourseHome/index.htm.

Jackson, J. D. *Classical Electrodynamics.* New York: John Wiley & Sons, Inc., 1999.

Jefimenko, O. D. *Electricity and Magnetism: An Introduction to the Theory of Electric and Magnetic Fields.* Star City: Electret Scientific Co., 1989.

Jones, H, et al. "The Stony Path to 100 T, Non-Destructive, Results!" *Megagauss - 10.* 2004. 54-58.

Kamerlingh Onnes, H. *Leiden Commun.*, no. 124C (1911).

Knoepfel, H. E. *Magnetic Fields - A Comprehensive Theoretical Treatise for Practical Use.* New York: John Wiley & Sons, Inc., 2000.

Kratz, R., and P. Wyder. *Principles of Pulsed Magnet Design.* Berlin: Springer-Verlag, 2002.

Kuznetsov, A. A. "Force-Free Coils for Magnetic Fields of Infinite Length." *Technical Physics* 6, no. 6 (1961): 472-475.

Lee, P. J. *National High Magnetic Field Laboratory, Applied Superconductivity Center.* 2006. http://www.magnet.fsu.edu/magnettechnology/research/asc/plots.html.

Lide, D. R. *CRC Handbook of Chemistry and Physics.* Boca Raton: CRC Press, 1994.

Low, B. C. "Force-Free Magnetic Fields." In *Encyclopedia of Astronomy and Astrophyics*. Nature Publishing Group, 2001.

Lundquist, S. "Magneto-Hhydrostatic Fields." *Ark.Fys.* 2, no. 361 (1951).

Luongo, C. A. "Superconducting Storage Systems: An Overview." *IEEE Trans. on Magn.*, 1996: 2214-2223.

Lust, K., and A. Schlute. "Kraftfreie Magnetfelder." *Z. Astrophys.*, 1954: 263-282.

MacLeod, M. A. "Force-Free Magnetic Fields, Curl Eigenfunctions, and the Sphere in Transform Space, With Applications to Fluid Dynamics and Electromagnetic Theory." *Environmental Research Papers*, 1993.

Markiewicz, W. D. *Cryogenics* 44 (2004): 767.

Marsh, G. E. "Flux Flow And Flux Cutting in Type II Superconductors Carrying A Longitudinal Current." *Physical Review B* 50, no. 1 (1994): 571-574.

Marsh, G. E. *Force-Free Magnetic Fields - Solutions, Topology and Applications.* New Jersey: World Scientific Publishing Co. Pte. Ltd., 1996.

Matsushita, T. "Macroscopic electromagnetic behavior of an ideal superconductor in a longitudinal magnetic field." *Phys. Lett.*, no. 33 (1981): 123-125.

Meinke, R. B. "Helical Coil Design and Process for Direct Fabrication from a Conductive Layer. " Patent pending. 2009.

Meissner, W., and R. Ochsenfeld. *Naturwissenshaften* 21 (1933): 787.

Miura et al. "Force-Free Coil Principle Applied to Helical Winding." *IEEE Trans.on Magnetics* 30, no. 4 (1994): 2573-2576.

Montgomery, D. B. *Solenoid Magnet Design.* New York: Wiley-Interscience, 1969.

Moon, F.C. "The Virial Theorem and Scaling Laws for Superconducting Magnet Systems." *J.Appl.Phys.* 53, no. 12 (1982): 9112-9121.

Moon, F.C. *Magneto-Solid Mechanics*. New York: John Wiley & Sons, Inc., 1984.

Motokawa, M. "Physics in High Magnetic Fields." *Reports on Progress in Physics*, 2004: 1995-2052.

National Research Council, of National Academies. *Opportunities in High Magnetic Field Science.* Washington: The National Academic Press, 2005.

Nelder, J. A., and R. Mead. "A Simplex Method for Function Minimization." *Computer Journal*, 1965: 308-313.

Nomura, S. "Force-Balanced Coil for Large Scale SMES." *IEEE Trans. on Magnetics* 9, no. 2 (1999): 354-357.

Nomura, S. "Experimental Results of a 7-T Force-Balanced Helical Coilf for Large Scale SMES." *20th International Conference on Magnet Technology.* Philadelphia, 2007. 4.

Nomura, S., et al. "Experimental Study on High-Temperature Superconducting Helical Coil." *IEEE Trans. on Appl. Superconductivity*, 2002: 788-791.

Nomura, S., Y. Ohata, T. Hagita, H. Tsutsui, S. Tsuji-Iio, and R. Shimada. "Design and Fabrication of a 7-T Force-Balanced Helical Coil." *IEEE Trans. on Appl. Superconductivity*, 2004: 739-742.

Oh, S., and K. Kim. *J.Appl.Phys.* 99 (2006).

Parker, E.N. "Reaction of Laboratory Magnetic Fields Against Their Current Coils." *Phys. Rev.* 109 (1958): 1440.

Press, W. H., B. P. Flannery, S. A. Teukolsky, and W. T. Vettering. *Numerical Recipes in C.* Cambridge: Cambridge University Press, UK, 1988.

Sass, A. R., and J. C. Stoll. "Magnetic Field of a Finite Helical Solenoid." *NASA Technical Note*, 1963.

Schneider-Muntau, H J. "Generation of Very High Continuous Fields by Polyhelix and Polyhelix Hybrid Magnets." *IEEE Transactions on Magnetics*, 1982: 1565-1570.

Schneider-Muntau, H. J. "Magnet Technology Beyond 50T." *IEEE Transactions On Applied Superconductivity*, 2006: 926-933.

Schneider-Muntau, H. J. "Physique Sous Champs Magnetiques Intenses." *Ed.du C.N.R.S.*, 1974: 161.

Schneider-Muntau, H. J., J. Toth, and H. W. Weijers. "Generation of the Highest Continuous Magnetic Fields." *IEEE Transactions on Applied Superconductivity*, 2004: 1245-1252.

Schneider-Muntau, H. J., Private Communications, 2009

Shneerson, G.A. et al."Generation of Megagauss Fields In Indestructible Solenoids With Quasi-Force-Free Windings." In *Megagauss Magnetic Field Generation, its Application to Science and Ultra-High Pulsed-Power Technology*, by H.J. Schneider-Muntau, 99-107. 1998.

Shneerson, G.A., O. S. Koltunov, and H. J. Schneider-Muntau. "The Concept of Quasi-Force-Free Magnets: Theoretical Substantiation, Estimation of Parameters, and Feasibility." *Phisica B.*, 2004: 566-570.

Shneerson, G.A., and O.S. Koltunov. "Computer Model of a Quasi-Force-Free Magnet With 100-T Field." *IEEE Trans.on Magn.*, 2008: 377-383.

Shneerson, G.A., O.S. Koltunov, and H.J. Schneider-Muntau et al. "The Concept of Quasi-Force-Free Magnets: Theoretical Substantiation, Estimation of Parameters, and Feasibility." *Phisica B.*, 2004: 566-570.

Shneerson, G.A., O.S. Koltunov, and H.J. Schneider-Muntau et al. "The First Quasi Force-Free Pulse Magnet - Computer and Natural Modeling." *Jn. Megagauss-10*, 2005: 68-71.

Smythe, W. R. *Static and Dynamic Electricity.* New York: McGraw-Hill, 1968.

Thome, R. *Magnetohydrodynamic and Fusion Magnets.* New York: John Wiley & Sons Inc, 1982.

Timms, W. E., and M. A.R. LeBlanc. "Achievement of Very High Critical Currents In Type II Superconductors." *J. Phys. F : Metal Phys.* 4 (1974): 136-153.

Van Bladel, J. *Some Remarks on Force-Free Coils.* U.S. Atomic Energy Commission Research and Development Report, Madison: Midwestern Universities Research Association, 1961.

Van Sciver, S. W. *Helium Cryogenics.* New York: Plenum Press, 1986.

Walmsley, D. G. "Force Free Magnetic Fields in a Type II Superconducting Cylinder." *J.Phys. F: Metal Phys.* 2 (1972): 510-527.

Wilson, M. N. *Superconducting Magnets.* New York: Oxford University Press Inc., 1983.

Wood, M. F., and D. B. Montgomery. "Colloques Intern.du CNRS." *Les Champs Magn. Intenses.* Grenoble, 1966.

Yangfang, Bi. "A Superconducting Toroidal Magnet With Quasi-Force-Free Configuration." *IEEE Transactions on Magnetics* MAG-19, no. 3 (May 1983): 324-327.

Zaghloul, H. "Force-Free Magnetic Fields." *Am.J.Phys.*, 1990: 783-788.

Zijlstra, H. "Experimental Methods in Magnetism - Generation And Computation of Magnetic Fields." In *Selected Topics in Solid State Physics*, by E. P. Wohlfarth. Amsterdam: North-Holland Publishing Company, 1967.